AN ABSTRACT OF THE DISSERTATION OF

George Law for the degree of Doctor of Philosophy in Chemistry presented on December 9, 2003.

Title: Surface Composition and Orientation of Room Temperature Ionic Liquids

Abstract approved:

Redacted for Privacy

Philip R Watson

In this thesis, we investigated the surface composition and orientation of both pure room-temperature ionic liquids (Ils) and binary mixtures of the ILs of the type consisting of the 1-alkyl-3-methylimidazolium ($[C_nmim]^+$, n = 4, 8, and 12) cation coupled with either $[PF_6]^-$, $[BF_4]^-$, $[Cl]^-$, or $[Br]^-$. The surfaces of the ILs were examined using both direct recoil spectrometry (DRS) and surface tension measurements. With DRS, a spectral signal produced by a recoiled surface atom indicates the existence of a particular molecular or ionic species at the interface. Derived from the signal are the atomic ratios, which are strongly dependent on the surface orientation of the surface species. The DRS findings are complimented with surface tension measurements, and the thermodynamics properties (surface enthalpy and entropy) derived from such measurements are related to the surface composition and orientation.

From the experiments on the neat ILs, the surface compositions of the imidazolium-based ILs were determined. Furthermore, the effects of systematic variations of the

cation size (the length of the 1-alkyl chain) and anion identity on the surface orientation of the organic cation were also examined.

The surfaces of binary mixtures containing ~25 mol % of $[C_{12}mim][PF_6]$ or $[C_{12}mim][BF_4]$ in $[C_4mim][BF_4]$ were also investigated. The DRS and surface tension data of the mixtures were compared to those of the pure components to determine the composition and any changes in the orientations of the cations upon mixing.

©Copyright by George Law
December 9, 2003
All Rights Reserved

Surface Composition and Orientation of Room Temperature Ionic Liquids

by

George Law

A DISSERTATION

submitted to

Oregon State University

in partial fulfillment of
the requirements for the
degree of

Doctor of Philosophy

Presented December 9, 2003
Commencement June 2004

Doctor of Philosophy dissertation of George Law presented on December, 9 2003

APPROVED:

Redacted for Privacy

Major Professor, representing Chemistry

Redacted for Privacy

Head of the Department of Chemistry

Redacted for Privacy

Dean of the Graduate School

I understand that my dissertation will become part of the permanent collection of Oregon State University libraries. My signature below authorizes release of my dissertation to any reader upon request.

Redacted for Privacy

George Law, Author

ACKNOWLEDGEMENTS

The author would like to express sincere appreciation to those who made the journey to and through the five years of graduate studies at Oregon State University possible.

Without the support and mentoring of Dr. Philip Watson, I might not have gone as far as I have. His suggestion of examining ionic liquids with direct recoil spectrometry resulted in a project that was challenging, interesting, and at times frustrating. I appreciate that he stuck with me despite the fact that at times I appear to be like a "deer caught in the headlights."

Much appreciation also goes to various OSU Department of Chemistry faculty and staff members. I believe that graduate students like myself would have found the graduate years more painful without the administrative, and emotional support of great people like Joey, Karen, Carolyn, Bob, Kristie, Dean, Gary, etc. I also want to thank various members of the faculty for the enjoyment of interacting with them, whether in graduate courses or working as a TA. I believe that faculty members such as Dr. Nibler, Dr. Nafshun, Dr. Hauser, Dr. Simonsen, etc. plays a big part in making this such a great department.

A BIG "Thank You" goes out to Mom, Dad, Grandma, Judy, and Linda for much love and support throughout my life. Thanks for listening and not telling me to "shut up" on those nights when I'm whining about graduate school. Also thanks to members of my extended family, Ken and Marie, for much support. Despite the fact that I met them after graduate school, I would not have gone as far as writing this acknowledgement without them.

I would also like to say that I am grateful to Tom and Michael for being great lab partners and great friends (not much more a grad student can ask for). And Tom, you will always be the man.

Thanks to all the great friends I have met here at OSU. I am glad that to have enjoyed the company of Rebecca, Lissa, Nipaka, Tony, Brian, Jeff, Ben, Rob, Sheri, etc. May Friday night "Beers Law" meetings be an OSU Chem Department tradition to be enjoyed by future grad students.

TABLE OF CONTENTS

		Page
1	General Introduction	1
1.1	Surface Chemistry and the Liquid State	1
1.2	Methods of Analysis of liquid Surfaces	5
1.3	Ion Spectroscopy and Direct Recoil Spectrometry (DRS)	7
1.3.1	Categories of Ion Spectroscopy	7
1.3.2	Historical Perspective on Ion Spectroscopy	7
1.4	Surface Analysis Using DRS	9
1.5	DRS and Analysis of Liquid Surfaces	10
1.6	Introduction to Ionic Liquids	11
1.6.1	What are Ionic Liquids?	11
1.6.2	The Advantages of Using ionic Liquids	13
1.6.3	Ionic Liquids at the Interface	14
1.7	Objectives of this Thesis Project	15
2	General Considerations: Theory	17
2.1	Overview of this Chapter	17
2.2	Kinematics of Elastic Collision Events	17
2.2.1	Impact Parameter	19
2.2.2	Direct Recoiling (DR)	20
2.2.3	Single Scattering (SS)	21
2.2.4	Multiple Collisions: Multiple Scattering (MS) and Surface.Recoil (SR)	23
2.3	Inelastic Effects: Ionization and Excitation	25

TABLE OF CONTENTS (CONTINUED)

Page

2.4 Collision Cross Sections..... 26

2.4.1 Mathematical Description of the Center of Mass Cross Section 27
2.4.2 Effects of Experimental Parameters on the Cross Section..... 29

2.5 Shadowing and Blocking..... 32

3 Experimental 34

3.1 Description of Direct Recoil Spectrometer..... 34

3.1.1 Ion Source..... 34
3.1.2 Ion Optics..... 34
3.1.3 Sample Cell..... 36
3.1.4 Detection Assembly..... 38
3.1.5 Miscellaneous..... 38

3.2 Experimental: Operation of the Spectrometer..... 39

3.2.1 Beam Optimization: Continuous Current..... 40
3.2.2 Beam Optimization: Pulsed Current..... 43

3.3 Data Analysis..... 44

3.3.1 Spectral Deconvolution..... 44
3.3.2 Atomic Ratios..... 47
3.3.3 Surface Orientation Simulations..... 48

4 Investigation of the Surface Orientation and Composition of Room Temperature Ionic Liquids..... 50

4.1 Introduction..... 50

4.2 Properties of Ionic Liquids..... 50

TABLE OF CONTENTS (CONTINUED)

Page

4.3 Experimental Methods..... 51

4.4 Results..... 52

4.4.1 DR Spectra Using 2.0-keV Ne^+..... 52
4.4.2 DR Spectra Using 2.5-keV Ar^+..... 54
4.4.3 Surface Atomic Ratios..... 57

4.5 Discussion..... 62

4.5.1 Influence of a on Atomic Ratios..... 62
4.5.2 Structural Considerations and Line-of-Sight Simulations..... 62
4.5.3 Cation/Anion Surface Composition..... 65
4.5.4 Cation Surface Orientation..... 67

4.5.4.1 Fluorine Containing Ionic Liquids..... 67
4.5.4.2 [C_8mim][Cl] and [C_8mim][Br]..... 76

4.6 Conclusion..... 78

5 Surface Tension Measurements of 1-Alkyl-3-Methylimidazolium Ionic Liquids..... 80

5.1 Introduction..... 80

5.2 Brief Overview of the Ring Method..... 81

5.3 Experimental Methods..... 82

5.4 Results..... 85

5.5 Discussion..... 88

5.5.1 Surface Tension and Surface Orientation..... 88
5.5.2 Surface Excess Quantities of ionic Liquids..... 92

TABLE OF CONTENTS (CONTINUED)

Page

5.6 Conclusion..... 95

6 Surface Composition of Mixtures of Room Temperature Ionic Liquids..... 96

6.1 Introduction..... 96

6.2 Experimental Methods..... 97

6.3 Results..... 97

6.3.1 DR Spectra of Ionic Liquid Mixtures..... 97

6.3.1.1 $[C_{12}mim][BF_4]$ (25.5 mole%) in $[C_4mim][BF_4]$..... 97
6.3.1.2 $[C_{12}mim][PF_6]$ (25.3 mole%) in $[C_4mim][BF_4]$..... 98

6.3.2 Surface Tension of the Ionic Liquid Mixtures..... 101

6.4 Discussion..... 103

6.4.1 Mixture A – (25.5 mol % $[C_{12}mim][BF_4]$ in $[C_4mim][BF_4]$..... 104
6.4.2 Mixture B – (25.3 mol % $[C_{12}mim][PF_6]$ in $[C_4mim][BF_4]$..... 109

6.5 Conclusion..... 111

7 General Conclusion..... 113

7.1 Summary..... 113

7.2 Future Studies..... 115

Bibliography 117

Appendices 122

Appendix A. Recoil Cross Sections 122
Appendix B. Supplemental DRS Spectra..... 125

LIST OF FIGURES

Figure		Page
1.1	Radical distribution function for a liquid.....	2
1.2	Interfacial region of a liquid.....	2
1.3	Surface correlation (density) profile of a liquid.....	3
1.4	The density-orientation profile $\rho(z,\theta)$ for a rod like molecule.....	4
1.5	Examples of heterocyclic cations used in ILs.....	12
1.6	The effect of chain length on melting points for $[C_nmim][PF_6]$ ILs.....	13
2.1	Schematic diagram of a DRS spectra.....	18
2.2	Illustration of the impact parameter (p).....	19
2.3	Schematic of direct recoiling (DR).....	20
2.4	Schematic of single scattering (SS).....	22
2.5	Schematic of multiple scattering (MS).....	23
2.6	Schematic of surface recoiling (SR).....	24

LIST OF FIGURES (CONTINUED)

Figure		Page
2.7	The relationship between the impact parameter (p), the CM scattering angle (θ), and the solid angle $d\Omega$.....	28
2.8	DR cross section as a function of recoil angle for oxygen atoms recoiled by various 3-keV noble gas ions	30
2.9	DR cross section as a function of recoil angle for various target atoms recoiled by 3-keV Ar^+ projectiles.....	31
2.10	DR cross section as a function of recoil angle for various target atoms recoiled by 3-keV Ar^+ projectiles at a recoil angle of 20°....	31
2.11	Schematic of shadowing with respect to the incident ion beam at the surface.....	33
2.12	Schematic of blocking with respect to the divergent beam of scattered or recoiled particles.....	33
3.1	Schematic diagram of direct recoil spectrometer.....	35
3.2	Schematic of DRS liquid sample cell.....	37
3.3	Overview of spectrometer operational procedures before data acqusition.....	41
3.4	Ion beam pulsing scheme.....	44

LIST OF FIGURES (CONTINUED)

Figure		Page
4.1	Composite DR spectra obtained from $[C_{12}mim][PF_6]$ using 2.0-keV Ne^+	55
4.2	DR spectra of ionic liquids taken with 2.00-keV Ne^+ at $\alpha = 16^o$	56
4.3	Deconvolution of peaks for [C12mim][PF6]	58
4.4	DR spectra of ionic liquids taken with 2.50-keV Ar^+ at $\alpha=16^o$	59
4.5	Experimental H/C ratios for $[C_8mim][Cl]$ and $[C_8mim][Br]$ from 2.0-keV Ne^+	60
4.6	Experimental H/C ratios from 2.0-keV Ne^+	61
4.7	Experimental F/C ratios from 2.0-keV Ne^+	63
4.8	Structure of IL cation (n = 4)	64
4.9	Arrangement of the cation and anion relative to the surface plane	66
4.10	Axis of rotation of the cation defining δ	68
4.11	Surface orientations of the cation based on the rotational angle (δ)	68

LIST OF FIGURES (CONTINUED)

Figure		Page
4.12	Estimated F/C ratios for $[C_nmim][PF_6]$ ILs from LOS simulations at $\alpha = 16^o$	70
4.13	Estimated F/C ratios for $[C_nmim][BF_4]$ ILs from LOS simulations at $\alpha = 16^o$	71
4.14	Estimated H/C ratios for $[C_nmim][PF_6]$ ILs from LOS simulations at $\alpha = 16^o$	74
4.15	Estimated H/C ratios for $[C_nmim][BF_4]$ ILs from LOS simulations at $\alpha = 16^o$	75
4.16	Estimated H/C ratios ($\alpha = 16^o$) for $[C_8mim][Br]$ and $[C_8mim][Cl]$	77
5.1	Schematic of ring tensiometer	81
5.2	Schematic diagram of sample heating cell	83
5.3	γ (mJ/m^2) as a function of temperature for the ionic liquids	86
5.4	Surface excess entropy (S_s) as a function of the number of carbon in chain	88
5.5	Surface excess enthalpy (E_s) as a function of the number of carbon in chain	88
5.6	Extreme orientations of the imidazolium cation (C4) based on rotation about the ring axis (rotational angle = δ)	91

LIST OF FIGURES (CONTINUED)

Figure		Page
5.7	Plot of surface excess entropy (S_s) versus surface excess energy (E_s) for the ionic liquids, and a series of *n*-alkanes and heterocycles.....	94
6.1	Spectra obtained from $[C_{12}mim][BF_4]$ (25.5 mole%) in $[C_4mim][BF_4]$ using 2.0-keV Ne^+.....	99
6.2	Spectra obtained from $[C_{12}mim][BF_4]$ (25.5 mole%) in $[C_4mim][BF_4]$ using 2.5-keV Ar+.....	100
6.3	Normalized DR spectra of $[C_{12}mim][BF_4]$ (25.5 mole %) in $[C_4mim][BF_4]$, neat $[C_4mim][BF_4]$, and $[C_{12}mim][BF_4]$ taken with 2.0 ke-V Ne^+ at $\alpha=16^o$.....	101
6.4	Normalized DR spectra of $[C_{12}mim][PF_6]$ (25.3 mole %) in $[C_4mim][BF_4]$, neat $[C_4mim][BF_4]$, and $[C_{12}mim][PF_6]$ taken with 2.0 keV Ne^+ at $\alpha = 16^o$.....	102
6.5	Surface tension (γ) as a function of temperature for several neat ILs and the two mixtures.....	103
6.6	Example of solver fit for solution A.....	108
6.7	Example of solver fit for solution B.....	110

LIST OF TABLES

Table		Page
1.1	Comparison of some popular ion spectroscopic techniques.....	8
3.1	Approximate values of I_e, gas pressures, and Wien filter settings for beam optimization.....	42
3.2	Approximate ranges of settings for the ion optics system.....	43
3.3	Relationship between parameters in Equation 3.3.2.....	46
3.4	Examples of recoil cross sections (σ_i) for recoiling from 2.50-keV Ar^+ and 2.0-keV Ne^+.....	48
4.1	Properties of $[C_nmim]\{X]$ ionic liquids.....	51
4.2	Predicted TOFs for 2.00-keV Ne^+ events.....	53
4.3	Predicted TOFs for 2.50-keV Ar^+ events.....	54
5.1	Surface tension (γ) of the ionic liquids at 336 K.....	85
5.2	Surface excess entropy (S_s) and surface excess enthalpy (E_s) of the ILs.....	87
6.1	Surface excess entropy (S_s), surface excess enthalpy (E_s), and the surface tension (γ) (at 328 K) of the IL mixtures and some neat ILs.....	104

LIST OF TABLES (CONTINUED)

Table		Page
6.2	Surface mole fraction (x_1^{σ}) of ionic mixture A, calculated with Equation 6.4.1, at 328 K.....	107

LIST OF APPENDIX FIGURES

Figure		Page
B1	DR Spectra of $[C_{12}mim][BF_4]$ obtained from 2.0-keV Ne^+.....	126
B2	DR Spectra of $[C_{12}mim][BF_4]$ obtained from 2.5-keV Ar^+.....	127
B3	DR Spectra of $[C_{12}mim][PF_6]$ obtained from 2.5-keV Ar^+.....	128
B4	DR Spectra of $[C_8mim][PF_6]$ obtained from 2.5-keV Ar^+.....	129
B5	DR Spectra of $[C_8mim][PF_6]$ obtained from 2.0-keV Ne^+.....	130
B6	DR Spectra of $[C_8mim][BF_4]$ obtained from 2.0-keV Ne^+.....	131
B7	DR Spectra of $[C_8mim][BF_4]$ obtained from 2.5-keV Ar^+.....	132
B8	DR Spectra of $[C_8mim][Cl]$ obtained from 2.0-keV Ne^+.....	133
B9	DR Spectra of $[C_8mim][Cl]$ obtained from 2.5-keV Ar^+.....	134
B10	DR Spectra of $[C_8mim][Br]$ obtained from 2.0-keV Ne^+.....	135
B11	DR Spectra of $[C_8mim][Br]$ obtained from 2.5-keV Ar^+.....	136
B12	DR Spectra of $[C_4mim][PF_6]$ obtained from 2.0-keV Ne^+.....	137
B13	DR Spectra of $[C_4mim][PF_6]$ obtained from 2.5-keV Ar^+.....	138

LIST OF APPENDIX FIGURES

Figure		Page
B14	DR Spectra of $[C_4mim][BF_4]$ obtained from 2.0-keV Ne^+.....	139
B15	DR Spectra of $[C_4mim][BF_4]$ obtained from 2.5-keV Ar^+.....	140
B16	DR Spectra of $[C_{12}mim][PF_6]$ (25.3 mole %) $[C_4mim][BF_4]$ obtained from 2.0-keV Ne^+.....	141
B17	DR Spectra of $[C_{12}mim][PF_6]$ (25.3 mole %) $[C_4mim][BF_4]$ obtained from 2.5-keV Ar^+.....	142

LIST OF APPENDIX TABLES

Table		Page
A.1	Constants A and B for various atomic species (projectile = Ne^+)...	124
A.2	Constants A and B for various atomic species (projectile = Ar^+)...	124

SURFACE COMPOSITION AND ORIENTATION OF ROOM TEMPERATURE IONIC LIQUIDS

1. General Introduction

1.1 SURFACE CHEMISTRY AND THE LIQUID STATE

Surface chemistry is concerned with the study of the physical and chemical properties, and interactions at the boundary separating two phases. Such a boundary is known as an interface, and more specifically referred to as a surface when one of the phases is a gas. Processes at surfaces play vital roles in daily life. For example, the adsorption and diffusion of molecules at the surface of lung tissue are two important factors in respiration. Work by surface chemists has lead to deeper understanding in the areas of catalysis, lubrication, evaporation, and crystallization, and has even been incorporated in the semi-conductor industry.

At phase boundaries, atoms and molecules are known to behave differently than those in the bulk [1]. In the bulk, a molecule is subjected to symmetrical forces. For those at or near the surface the forces, both attractive and repulsive, are no longer symmetrical [2]. This asymmetry produces variations in properties, such as density, between the bulk and the surface. Chemical reactions at surfaces may also differ from reactions in the bulk, and can be attributed to differences in activation energies. To establish an understanding of surfaces, an examination of surface structures at the molecular level is necessary.

Of the surfaces of interest, the liquid surface is the most challenging to study. The molecules in the liquid state have greater degrees of rotational and translational freedom, allowing movement between the bulk and surface, as well as across the surface. Such mobility of the molecules lead many early scientists to speculate that

there is complete disorder in both the bulk and the liquid surface. However, studies of liquids using X-ray diffraction lead to conclusions that bulk liquids are not completely amorphous [3]. X-ray diffraction of liquid mercury and water allowed for the description of the liquid structure using radial distribution functions (g(r)), as shown in Figure 1.1. The distribution function describes the probability that one molecule is found a certain distance from another, and the oscillatory pattern seen for a liquid indicates the existence of short-range order without long-range order.

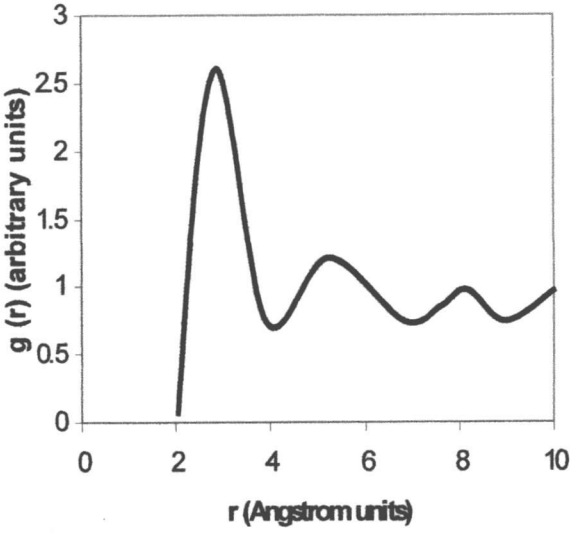

Figure 1.1 Radial distribution function for a liquid

Furthermore, unlike a solid, a liquid does not have a sharply defining boundary, but has a region where the density and local pressure gradually decrease going from the liquid to the vapor phase, as illustrated in Figure 1.2 [4]. The treatment of such an interface is often carried out through statistical mechanics by using a surface- correlation (density) function ($\rho(z)$). The behavior of such a function is shown in Figure 1.3, where z is the height, which is negative at the

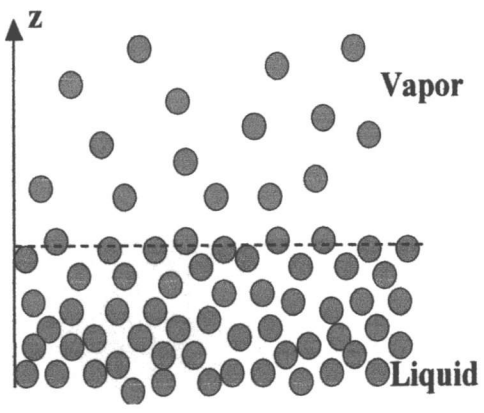

Figure 1.2 Interfacial region of a liquid

liquid side of the interface and positive at the vapor side. For convenience, a mathematical dividing surface is set at z = 0.

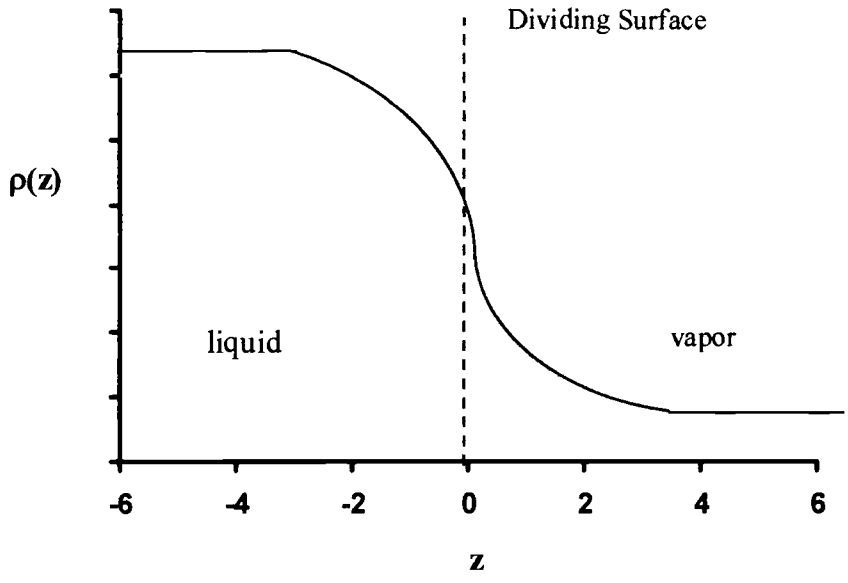

Figure 1.3 Surface correlation (density) profile of a liquid

As with bulk molecules, molecules in the interfacial region experience short-range order. For rigid asymmetrical molecules, anisotropy in the forces in addition to the limited freedom to rotate, allows for molecular alignment such that the mutual interaction energy is at a maximum. Computer simulations of the interfacial density profile, allowing for molecular rotation, have indicated that such preferential orientations are angular averages. The density-orientation profile ($\rho(z,\theta)$) of rod like molecules interacting via Lennard-Jones+anisotropic dispersion forces is illustrated in Figure 1.4. The figure shows that the molecules tend to align perpendicular on the liquid side of the dividing surface, and parallel on the vapor side.

The study of liquid surfaces is a challenge for chemists, especially when structural information is involved. The mobility of the molecules at the diffuse boundary makes it difficult to experimentally determine molecular orientations.

However, experimental techniques coupled with computer simulations generally help in the determination of the surface structure of liquids at the microscopic level.

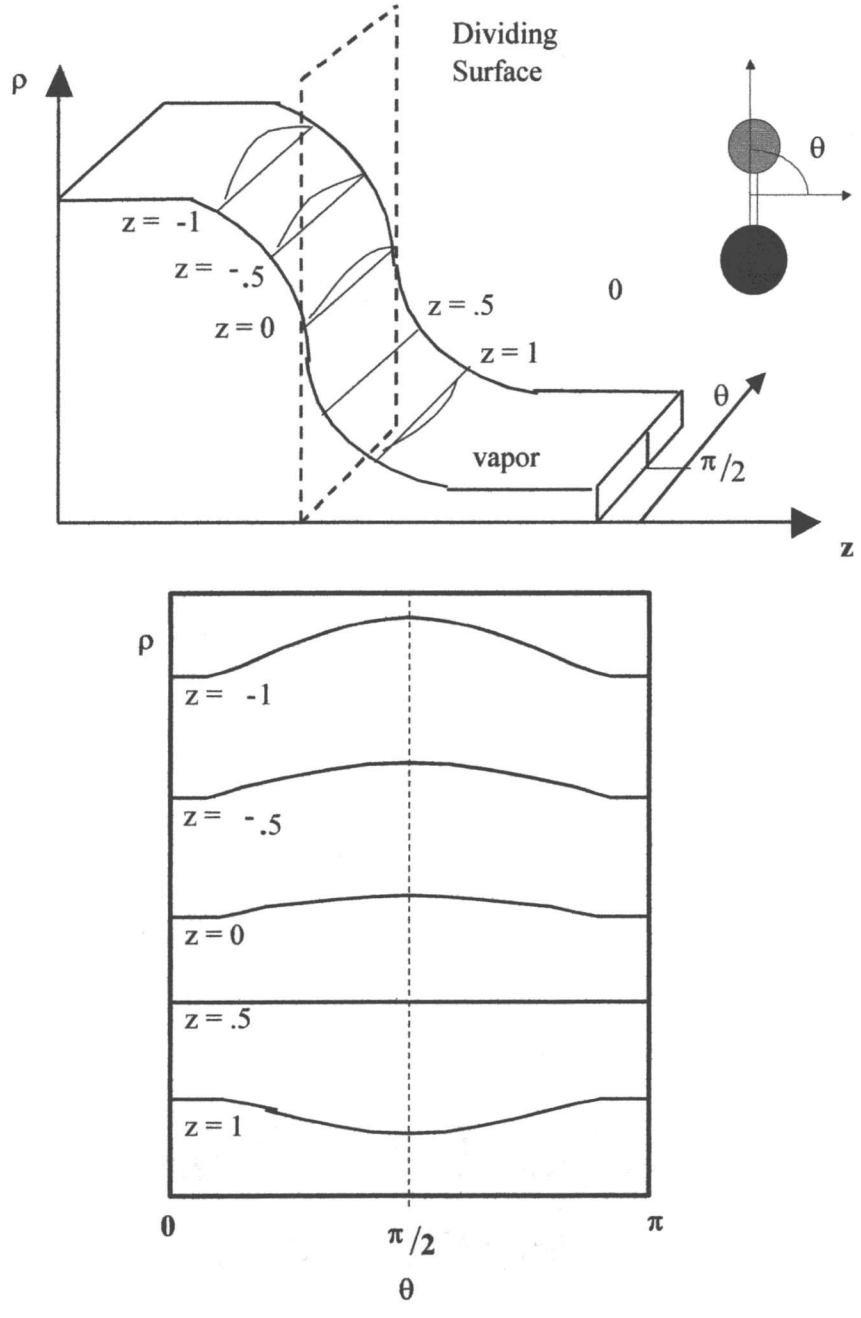

Figure 1.4 The density-orientation profile $\rho(z,\theta)$ for a rod like molecule

1.2 METHODS OF ANALYSIS OF LIQUID SURFACES

Surface analysis techniques for energetic particles fall into three general categories such as ions, electrons, and photons [5]. For studies of crystalline and amorphous solid surfaces, analytical methods utilizing electronic interactions with surface atoms and molecules include Auger electron spectroscopy (AES), low energy electron diffraction (LEED), and high-resolution electron energy loss spectroscopy (HREELS). Methods using atomic or molecular ion beams include ion scattering spectroscopy (ISS), secondary ion mass spectrometry (SIMS), and Rutherford backscattering spectroscopy (RBS). Photon-surface interactions are used in such techniques as X-ray photoelectron spectroscopy (XPS), and low angle X-ray diffraction. Other techniques that do not fall into these categories are atomic force microscopy (AFM) and scanning tunneling microscopy (STM). Both AFM and STM allows for atomic resolution imaging of surfaces.

Despite the numerous instruments available to surface chemists, few of them are employed for liquid surfaces. Until the late 1980s, scientists had to determine liquid surface structures indirectly. The most popular approach was to measure the surface tension of a liquid, and compare the values to systems where the molecular orientation at the surface is known [4].

Another approach was to model liquid surfaces using either Monte Carlo or molecular dynamics methods. In both techniques, a computer generates all possible molecular states belonging to a given thermodynamic state, and by assigning the proper weight to each, ensemble averages of structural and macroscopic properties are obtained [6]. Both methods have been applied to liquid surfaces since the 1970s. However, such theoretical predictions are limited by computing power and time, and much of the structural investigations have been limited to atomic liquids, molten metals, and simple molecules.

In the last decade, the rapid development of laser technology has resulted in the development of non-linear optical techniques to probe liquid surfaces. The two that are the most popular are second-harmonic generation (SHG) spectroscopy and sum-frequency generation (SFG) spectroscopy. SFG is a vibrational spectroscopy, while SHG is an electronic spectroscopy. Both SFG and SFG are able to differentiate signals from the bulk versus that of the surface [7], therefore generating spectra that give detail on surface orientation. Of the two techniques, SFG is more useful because the vibrational transitions are narrower, and therefore allows for both compositional and orientational analysis [8]. As a result SHG is limited to neat liquids, and monolayers formed between two immiscible chemical species. Whereas, SFG has been used to examine surface interactions between complex systems such as that of sodium dodecyl sulfate (SDS) adsorbed at the D_2O-CCl_4 interface [9].

Two other techniques often mentioned in literature in regards to investigations of liquid surface structure are ellipsometry and X-ray reflectivity. Ellipsometry is a polarimetric technique that involves the measurement of changes in polarization of monochromatic light from a liquid surface [10] and has been shown to be sensitive to surface density variation and to surface molecular orientation [11]. Ellipsometric investigations have been performed on the surface freezing of liquid alkanes [12], and on monolayers of phospholipids on alkanes and bicyclohexane [13]. X-ray reflectivity involves the determination of electron density from the intensity of reflected X-ray beams. It has been used to obtain orientational information on n-alkanes [14] and normal 1-alcohols [15], as well as on liquid crystals such as n-cyanobiphenyls [16]. While both ellipsometry and X-ray reflectivity appear useful for orientational studies, they are limited to those liquids where molecules are highly ordered at the interface.

1.3 ION SPECTROSCOPY AND DIRECT RECOIL SPECTROMETRY (DRS)

1.3.1 Categories of ion spectroscopy

The surface analysis method described in this thesis is direct recoil spectrometry (DRS). DRS is an analysis tool that falls under the class of technique known as ion spectroscopy. Ion spectroscopy is based on the physics of ion-surface interaction. Generically speaking, in ion spectroscopy a beam of mono-energetic incident ions (primaries) is projected towards a surface, resulting in collisions with target atoms. The impact can then produce one or more possible events: scattering of primary ions, and recoil of surface ions and neutrals.

Ion spectroscopy is categorized according to the energy of the primary, and are as follows: low-energy ion spectroscopy (LEIS, ~1-10 keV), medium-energy ion spectroscopy (MEIS, ~20-200 keV), and high-energy ion spectroscopy (HEIS, 200-2000 keV) [17]. The specific techniques are differentiated based on the primary energy, species analyzed, and the type of analysis (mass, energy, or time-of-flight [TOF]). A comparison of some of the more popular techniques in surface analysis using energetic ions is shown in Table 1.1.

1.3.2 Historical perspective on ion spectroscopy

Historically, ion spectroscopy gained first recognition as an analytical tool in the early 1960s due to the work of Tukevich and coworkers [18]. Their studies lead to the implementation of high-energy scattering experiments in the Surveyor V mission to analyze the composition of the lunar surface [19]. Other works during this decade that contributed to an understanding of ion-surface interactions, included the detection of recoiled ions by Datz and Snoek [20], and by Mashkova and Molchanov [21, 22]. In 1967, Smith [23] demonstrated that low-energy ions (1 keV- He^+, Ne^+,

or Ar^+) could be used to collect compositional information on solid surfaces. His experiments showed that scattering of the primaries from surface atoms of different masses into energy-dispersive detectors produced spectral peaks corresponding to characteristic energies [18]. Later works by Chu et al. [24], and Brogersma and Mul [25] in 1973, produced mass spectra of the surfaces.

Table 1.1 Comparison of some popular ion spectroscopic techniques

	Primary Energies	Examples of Primary Ions Used	Species Analyzed	Type of Analysis
LEIS	1-10 keV	H^+,He^+,Ne^+,Ar^+	scattered primary ions	Energy
SIMS	1-30 keV	Cs^+,O_2^+,Ar^+,Ga^+	secondary ions	Mass
RBS	1-3 MeV	He^{2+}	backscattered neutrals	Energy
DRS	1-5 keV	He^+,Ne^+,Ar^+	recoiled neutrals and scattered primaries	TOF or Energy

The detection of DR species was introduced in 1977, when Chen et al. [26] described surface analysis, in the low energy regime, of both recoiled ions and atoms from a solid surface using a TOF spectrometer. This was followed by investigations of other physicists, such as Boers et al. [27], and Eckstein et al. [28], to improve upon the LEIS-TOF methodology.

The use of TOF technique in chemical analysis was first accomplished by chemists lead by Rabalais [29]. This group of chemists investigated the chemisorption of H_2O on Mg using TOF analysis of recoiled species (ions and atoms). By using the H direct recoil peak intensity, they were able to obtain a surface stoichiometry of $Mg(OH)_2$ when water reacted with the polycrystalline substrate. This group rapidly demonstrated the capabilities of the technique to determine surface structure and composition on other solids such as silicon nitride [30], and polyimides [30]. It was in these later studies that Rabalais referred to this technique as direct recoil spectrometry (DRS).

1.4 SURFACE ANALYSIS USING DRS

DRS experiments can be carried out using two types of analysis systems. The energies of scattered primary ions and recoiled ions can be measured using electrostatic analyzers. A second type of analysis system is the TOF analyzer. The TOF spectra can be generated from recoil neutrals, recoiled ions, or scattered primaries. By varying either the incident energy and/or mass, or the recoil angle, the types of spectra (scattering or recoiling) can compliment each other in chemical analysis. DRS in the TOF mode has been referred to as both time-of flight scattering and recoiling spectrometry (TOF-SARS), and time-of-flight direct recoil spectrometry (TOF-DRS). The investigation presented in this thesis is of this technique using a TOF analyzer, and for the sake of simplicity shall be referred to as DRS.

DRS has been shown to be a multifaceted surface analysis tool. The two important features are its abilities in qualitative and quantitative elemental analysis, and surface structural determination. Other useful applications include, but not limited to, the monitoring surface diffusion, and determination of ion-surface electronic transitions [32].

The advantage of using DRS in elemental analysis is due to capability to directly detect all elements including hydrogen. Hydrogen detection is not possible with either XPS or AES, because both techniques are based on two electron processes. Also, due to its small mass, the hydrogen direct recoil peak appears at short TOF and is easily set apart from other elements. The hydrogen detection in DRS makes it ideal as a quantitative tool to probe many organic liquids.

DRS is extremely surface sensitive. For a technique such as XPS, the depth penetration of X-ray photon allows for integration over the top 10 Å. Computer simulations from this laboratory have confirmed that 50-75% of the recoils in DRS originate from the top 1.5 Å [33]. This surface sensitivity allows for the effectiveness of DRS in structural determination. Furthermore, due to the low ion doses ($\sim 10^{-11}$ ions/cm^2) and pulsing of the beam, damage to the sample surface and surface charging is avoided [32].

1.5 DRS AND ANALYSIS OF LIQUID SURFACES

While the majority of DRS investigations focused on solid surfaces, the potential of the technique in examining liquid surfaces was not explored until the mid-1990s. During this time, this laboratory began construction on a DRS specifically designed for liquids. As with many surface analysis techniques, DRS experiments are performed under high vacuum ($\sim 10^{-6}$ torr). In ion-based techniques, analysis under vacuum increases the mean free path (λ) traveled between collisions of the incident ions and recoiled surface species. However, the use of a vacuum poses a significant challenge for liquid analysis. Due to the fact that many liquids have high vapor pressures at ambient conditions, introduction of a liquid into a vacuum would result in evaporation of the sample either during the pump-down period or through the course of the analysis. However, by proper selection of liquid, sample depletion can

be avoided. Furthermore, preliminary investigations have shown that DRS signals originate from the liquid surface, not from the vapor [34].

The structural information obtained by DRS on liquid differs from that of solid surfaces. Whereas atoms in a solid remain stationary with respect to their neighbors, the molecules at the liquid surface are mobile and subjected to molecular tumbling during the course of the experiment. However, as the previously mentioned density-orientation profiles have indicated, any preferential orientations are essentially angular averages. Therefore, it is expected that any information obtained by DRS on composition and orientation will be statistical averages.

The spectrometer has been used to investigate the surface orientation of several liquid systems. The liquids previously investigated include:

- Dioctyl phthalate (DOP) and bis(2-ethylhexyl) chlorendate (BEHC), where the results showed DRS as a viable tool to determine the "head-tail" orientation of these molecules [35].
- Glycerol: the orientation inferred from DRS is consistent with an upright molecular axis, as reported in SHG experiments and molecular dynamic simulations [34].

Other liquids examined include squalene and n-heptadecane. Recently, our investigations have focused on the surface characteristics of room-temperature ionic liquids [36], of which the findings will be presented in this work.

1.6 INTRODUCTION TO IONIC LIQUIDS

1.6.1 What are ionic liquids?

Traditionally, the term ionic liquid (IL) was used to refer to high-temperature molten salts. Many of these inorganic ionic liquids have been used in industrial processes, such as for aluminum production [37]. The use of the term ILs, or more

specifically room-temperature ILs, in this work is in reference to salts containing organic cations and inorganic anions. Room-temperature ILs have been documented through out the 20th century. For example ethylammonium nitrate ($[EtNH_3][NO_3]$), which has a melting point of 12°C, was first reported in 1914 [38]. However, the applications and properties of the ILs were not extensively investigated until the 1980s [39].

Since then, the chemical and solvent properties of ILs have been extensively studied. The detail reviews of the ILs have been presented by several authors, including Seddon [40], Welton [41], and Holbrey [42]. The ambient-temperature ILs, most often discussed, consists of bulky heterocyclic cations. Examples of typical cations used in ion ILs, such as 1-butyl-3-methylimidazolium ($[C_4mim]^+$) and N-butylpyridium ($[Nbupy]^+$), are shown in Figure 1.5.

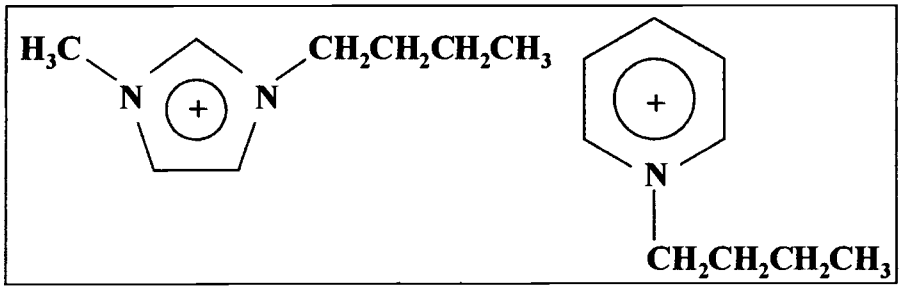

Figure 1.5 Examples of heterocyclic cations used in ILs: (left) $[C_4mim]^+$, (right) $[N\text{-}bupy]^+$

The size of the cation, and its asymmetry are key factors in the reduction of the crystalline lattice energy, and leads to lower melting points [43]. The identity of the anion determines the chemical properties of the IL system. Typical anions include $AlCl_4^-$, NO_3^-, PF_6^-, and BF_4^-. By altering the size (the alkyl chain length) and the anion, chemists have shown that ILs can be "designed" according to the necessary chemical purpose. An example of the effect of alkyl chain length on the melting

point of 1-alkyl-methylimidazolium hexafluorophosphate ($[C_nmim][PF_6]$) is illustrated in Figure 1.6. Furthermore, varying the mole ratios in binary and ternary mixtures of ionic liquids can alter solvent properties. Including such mixtures, it has been estimated that there are 10^{18} accessible room temperature ionic liquids [42].

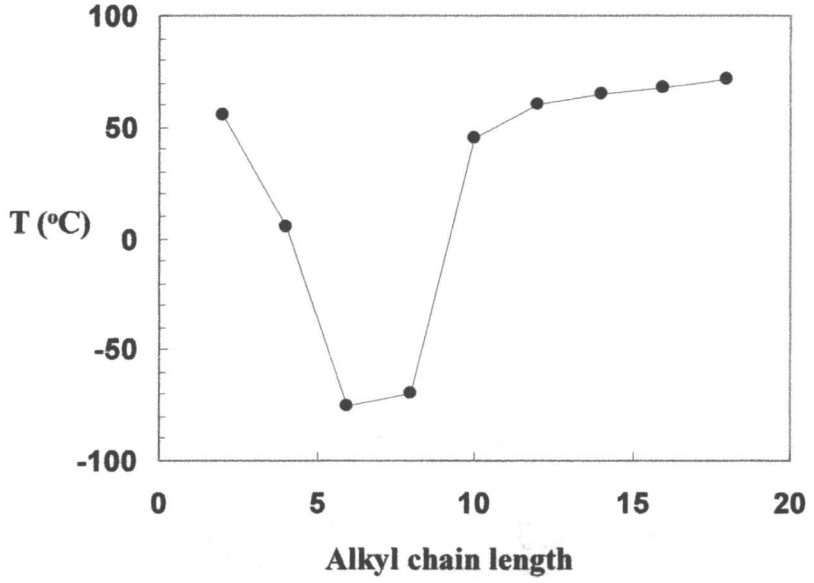

Figure 1.6 The effect of chain length on melting point for $[C_nmim][PF_6]$ ILs

1.6.2 The advantages of using ionic liquids

ILs dissolve an enormous range of inorganic, organic, and polymeric materials at very high concentrations, are non-corrosive, have low viscosities and no significant vapor pressures. ILs also have a liquid range of 300°C, and are thermally stable up to 200°C [44]. Due to these properties, ILs have been proposed as an alternative in replacement of traditional solvents in synthetic chemistry. Also of interest to chemists, are that ILs have variable acidity, are highly polar yet are non-

coordinating, and can be separated from most reaction by-products. There are other advantages of ILs in organic synthetic reactions, and such examples include:

- The replacement of water in Diels-Alder cycloadditions, so that moisture sensitive reagents can be used [41].
- In the alkylation of sodium β-naphthoxide, the use of ILs as solvents leads to the high regioselectivity of the alkylation product [41].

ILs have also shown to be beneficial in inorganic applications. For example, research by the British Nuclear Fuels Laboratory (BNFL) has shown that ILs containing nitrates, such as 1-butylpyridium nitrate, can be used in nuclear fuel reprocessing [45]. In the extraction of uranium (IV) oxide and plutonium (IV) oxide and the conversion to useful products in ILs reduces the number of processing cycles. In this case, ILs offers economical and environmental advantages. ILs have also been used as an electrolyte in photogalvanic cells [42]. By using ILs, the cells have been shown to have increased electrical conductivity and thermal stability.

1.6.3 Ionic liquids at the interface

A rapidly developing application area for ionic liquids is that of multiphasic homogeneous catalytic reactions [41, 46-48]. In this type of reaction, the IL is chosen to dissolve the catalyst and is immiscible with the second phase containing reactants and products. Such catalysis is believed to occur at the IL-organic interface, and must be strongly dependent on access of the catalyst to the surface and the transfer of material across the interface.

An example of such applications of ILs are in Heck reactions [49], which involves the coupling of aryl or benzyl halides with alkenes with a palladium catalyst. With typical organic solvents, the catalyst is usually not extractable. However, by performing the multiphasic reaction with ILs, the catalysts can be

extracted from the IL phase. Furthermore, the product yields were shown to be high and dependent on IL used [47]. It is believed that the reactivity is affected either by a change in the concentration of the catalyst at the interface or by a change in the nature of the catalyst. Such a change is likely dependent on the IL/catalyst interaction at the interface. Therefore, knowledge of the surface behavior of ILs is important in understanding the solvent interactions in such multiphasic catalytic processes.

1.7 OBJECTIVES OF THIS THESIS PROJECT

The worked discussed in this thesis is essentially an ongoing project that started with the construction and initial tests of the liquid DR spectrometer by Thomas Gannon and Michael Tassotto. The engineering details have been previously documented in their thesis [50, 51]. The investigations presented in this thesis are essentially a continuation of their work in investigation on the viability of using DRS as a tool to investigate liquid surfaces.

The work presented in proceeding chapters will focus on the determination of the surface composition and orientation of ILsconsisting of the 1-alkyl-3-methyl-imidazolium cation ($[C_nmim]^+$). A preliminary study on one of the ILs, 1-butyl-3-methylimidazolium hexafluorophosphate ($[C_4mim][PF_6]$), has been discussed in the thesis of Thomas Gannon. The experiments presented here focuses on the effect of the surface characteristics of neat and binary mixtures of ILs when: a) the 1-alkyl chain length of the cation is varied, and b) the type of anion is changed. Surface information will include:

- the composition of the ionic liquids at the surface- whether surface segregation of the ions occur
- the preferential orientation of the cation at the surface, and variations of the orientation with cation size and anion type

- the change in composition and orientation of the ions in a binary mixture as compared to the neat liquids

The surface tensions of neat and binary mixtures ILs were also determined at various temperatures. Such measurements were used to obtain information on the surface thermodynamics on the ILs. In addition it was shown to be a simple and effective way of complimenting the orientational information obtained from DRS.

2. GENERAL CONSIDERATIONS: THEORY

2.1 OVERVIEW OF THIS CHAPTER

The ion-surface interactions in DRS can be viewed as a series of binary collisions. The binary collision discussed in this chapter involves a projectile (incident ion) and a stationary target (surface atom) interacting through a potential energy (Vr). Such a collision can be either elastic or inelastic. In an elastic collision, there is no permanent change in the internal energy of the collision pairs, and the total kinetic energy, linear and angular momenta are conserved. In an inelastic collision, momentum is still conserved, but the total kinetic energy after the collision changes through excitation or ionization of one of the collision pairs. This discussion of the theory behind DRS will focus on the

- kinematics of elastic collisions: the types of collision events and the kinetic energies of scattered and recoiled species
- inelastic effects: energy losses due to electronic processes
- cross sections: the probability that a scattered or recoiled will have a particular trajectory
- shadowing and blocking: problems in the collision model with multi-atom targets

2.2 KINEMATICS OF ELASTIC COLLISION EVENTS

The kinematics of the collision events in the KeV range, such as those in DRS, is well described by the binary elastic collision (BEC) model. This model over-simplifies the process in that it: a) ignores the influence of the atoms surrounding the target, b) treats both projectile and target as hard spheres, and c) ignores bonding and

atomic vibrations [52]. However, it has been found to be useful, and allows for the application of the laws of conservation of kinetic energy and momentum to describe the post-collision particle energies.

In the usual experimental arrangement for DRS, the ion source and the detector are in-plane with respect to the surface normal. When the projectile strikes the surface, the four possible surface collision events that can occur are direct recoiling (DR), single scattering (SS), multiple scattering (MS), and surface recoiling (SR). The DRS spectral features of the four mechanisms are shown in Figure 2.1. The peak labeled P is that of a photon peak attributed to inelastic collisions that result in deactivation by photon emission. These events depicted in the figure and discussed in the proceeding sections are associated with a particle trajectory away from the surface (i.e. away from the condensed phase).

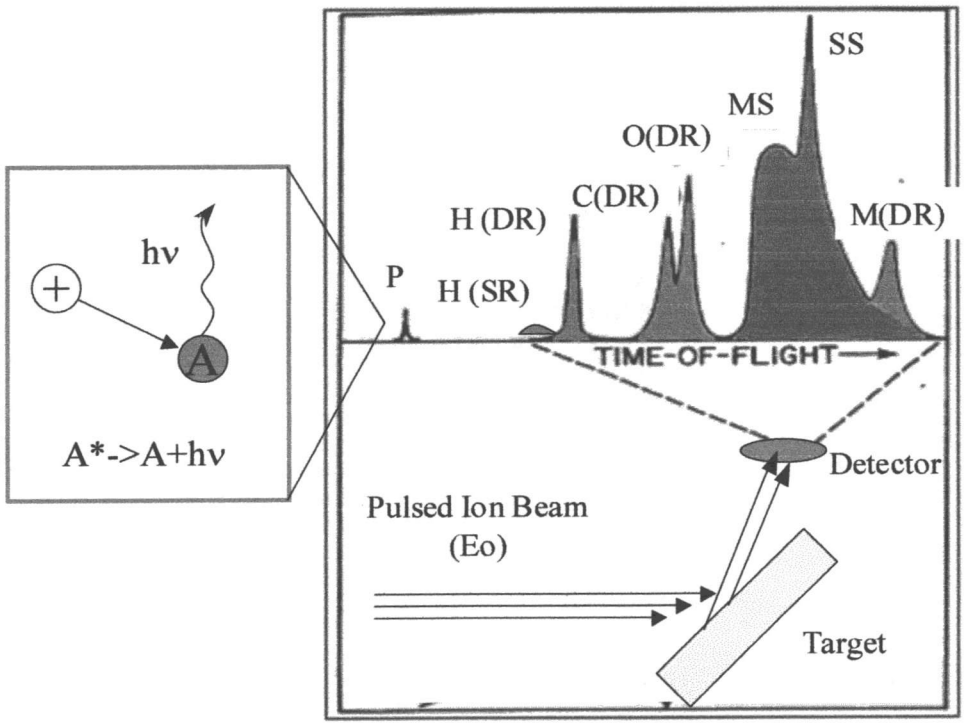

Figure 2.1 Schematic diagram of a DRS spectra: the peaks are associated with surface recoiling (SR), direct recoiling (DR), single scattering (SS), multiple scattering (MS), and photon emission (P).

It must be noted that the diagrams used in the following sections to illustrate the various collision events represent the ideal collisional processes at the surface. The trajectory of the ions can also lead to penetration of the surface plane. In such a situation, the trajectory of the scattered or recoiled particle and incoming ion can be altered by further collisions. Scattered and recoil particles from below the surface and inelastic loses results in a long tail in the respective peaks. Sputtering of molecules or clusters is also possible. But the low energies of such species (1 – 20 eV) do not allow for their detection, because they fall under the detection thresholds of the channel electron multipliers (CEM) typically used in DRS.

2.2.1 Impact parameter

Consider first the collision between a projectile of mass m_1 with a kinetic energy of E_o, and a target of mass m_2 that is initially at rest in the LAB frame (the reference frame of the laboratory observer). The likelihood that a collision will occur is dependent on the impact parameter (p). As shown in Figure 2.2, the impact parameter is the perpendicular distance from the center of the target to the path the projectile would take if it were not deflected [53], and is a measure of the directness

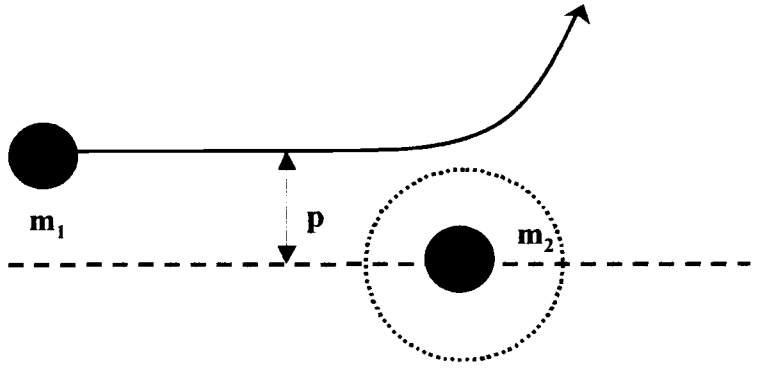

Figure 2.2 Illustration of the impact parameter (p)

of the collision, with p = 0 corresponding to a head-on collision. This parameter is important in the magnitude of energy transferred between projectile and target. The post-collision trajectories are also dependent on p.

2.2.2 Direct recoiling (DR)

The collision event that is of the most interest in DRS is the direct recoiling (DR) of a surface atom. The large angle in–plane DR of a surface atom away from the condensed phase and the scattering of the projectile into the bulk are illustrated in Figure 2.3. In this figure, the recoiling angle (ϕ) is in the LAB frame, while both the angle of incidence (α) and exit angle (β) are defined with respect to the surface plane. Furthermore β is defined by α and ϕ as $\beta = \phi - \alpha$. The figure also shows the scattering of the ion into the bulk.

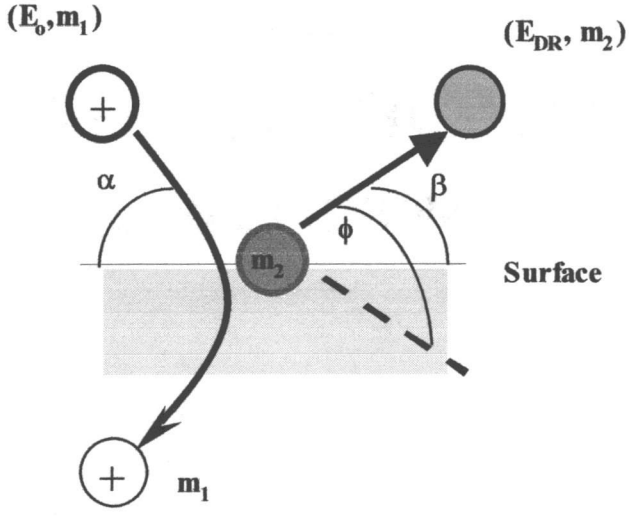

Figure 2.3 Schematic of direct recoiling (DR): α = angle of incidence, β = exit angle, ϕ = recoiling angle, E_o = kinetic energy of projectile (ion), m_1 = mass of projectile, m_2 = mass of target atom, and E_{DR}= energy of recoiled atom.

The energy of the recoiled atom (E_{DR}) is determined by [32]

$$E_{DR} = [(4\ E_o m_1 m_2)/(m_1 + m_2)^2]\ (\cos^2 \phi) \qquad 2.1$$

where ϕ is the recoiling angle, which is experimentally set at 45°. The time of flight of the DR atom (t_{DR}) for the flight path (L) between the surface to the detector is then calculated by [32]

$$t_{DR} = [L(m_1 + m_2)]/[(8\ m_1 E_o)^{1/2}(\cos \phi)] \qquad 2.2$$

In the experimental setup described in this thesis, L is 1.125 m.

As Equation 2.1 indicates, recoil does not occur at $\phi = 90°$ (i.e. $E_{DR} = 0$). Applying values of $\phi > 90°$, a non-zero and positive value of E_{DR} can be obtained. However, the laws of conservation of momentum dictates that the velocity vectors of the incident, scattered, and recoiled particles must form a closed triangle [54]. Such is not the case when the angle is greater than 90°, and therefore the recoiling angle is limited to $\phi < 90°$. Furthermore, close inspection of Equation 2.1 shows that the recoil energy is at a maximum at small values of ϕ.

2.2.3 Single scattering (SS)

Single scattering (SS), as illustrated in Figure 2.4, is the large angle deflection of the ion away from the surface. The single scattering (SS) of the ion produces a sharp peak similar to that in Figure 2.1.

The energy of the scattered ion (Ess) can then be determined by [32]

$$E_{ss} = (E_o\, m_1^2/(m_1 + m_2)^2)\ (\cos \theta \pm [(m_2/m_1)^2 - \sin^2 \theta)^{1/2}]^2 \qquad 2.3$$

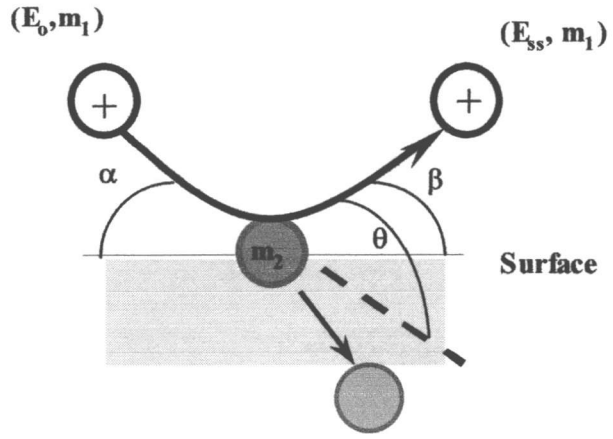

Figure 2.4 Schematic of single scattering (SS): α = angle of incidence, β = exit angle, θ = scattering angle, E_o = kinetic energy of projectile (ion), m_1 = mass of projectile, m_2 = mass of target atom, and E_{ss} = kinetic energy of scattered ion

which shows, E_{ss} can have two possible values. In the case of $m_1 \leq m_2$, the positive sign is used, and θ can vary from 0° to 180° [18]. However, in the case of $m_1 > m_2$ both signs are used, but only $\theta < 90^o$ is possible [18]. The expression of kinetic energy of the scattered ion is said to be doubled-valued, leading to two values of E_{ss} for each θ. The two values of E_{ss} correspond to two different collisions resulting in the same scattering angle of the ion. The use of the positive sign (when $m_1 > m_2$) is a result of a glancing collision with a large impact parameter p. The use of the negative (when $m_1 > m_2$) is a result of a direct impact with a small p. Also when $m_1 > m_2$, the maximum or critical angle (θ_c) in which scattering is observed is given by

$$\theta_c = \arcsin (m_1/m_2)^{-1} \qquad 2.4$$

E_{ss} can then be converted to a single scattering TOF (t_{ss}) by taking into consideration the path length from the surface to the detector (L). The TOF of the scattered ion is then given by [32]

$$t_{ss} = L(m_1 + m_2)/((2\ m_1E_o)^{1/2}[\cos\theta + [(m_1/m_2)^2 - \sin^2\theta]^{1/2}]] \qquad 2.5$$

It must be noted that for the DRS experiments presented in this thesis θ and ϕ are fixed at 45°.

2.2.4 Multiple collisions: multiple scattering (MS) and surface recoil (SR)

One of the major problems in DRS is broad peaks that may overlap with the sharper SS and DR peak, which can be due to multiple collisions of ions or recoiled neutrals. One such event is a multiple-scattering (MS) event, represented by two or more large angle deflections of the ion that may be proceeded by, and followed by, several small angle deflections. An example of MS involving two large angle defections, a double scattering, is shown in Figure 2.5. In the ke-V range, MS events can be treated as a series of *n* independent binary elastic collisions only if the distance of closest approach between the ion and target is smaller than the interatomic spacing (d) [52]. The maximum MS energy can then be approximated by *n* applications of Equation 2.5 for each collision. For a double collision, the

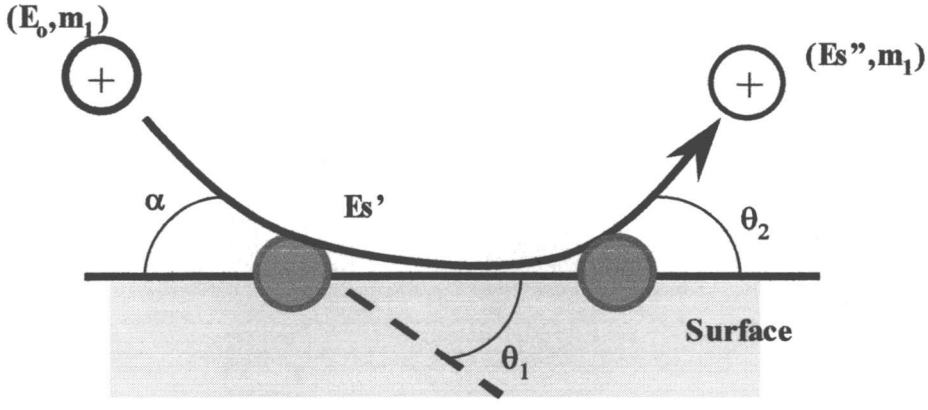

Figure 2.5 Schematic of multiple scattering (MS): involving two large angle deflections, θ_1 = angle of first scattering event, and θ_2 = angle of second scattering event.

energy of the first deflection (E_S') can be calculated by using E_o and θ_1. The energy following the second deflection (E_S") is then approximated by using θ_2 and E_S'.

The ions that participate in large angle MS typically depart the surface at a particular θ with higher energies than the singly scattered species. For example, in the scattering of 1-keV He^+ off a surface of O atoms, the single scattering energy is 0.863 keV ($\theta = 45^o$). For a doubly scattered He^+ ($\theta_1 = \theta_2 = \theta/2$), the scattering energy is 0.963 keV.

Also observed in the DRS spectra are broad and lower energy MS peaks. Such peaks can be attributed to projectiles that penetrate the surface, participate in many multiple scattering events, and re-emerge from the bulk. Such peaks can also involve backscattering in the MS process. In general computer simulations are required to approximate the final scattering energies [55] in such cases.

A second type of event involving multiple collisions is that of surface recoiling (SR). An example of this mechanism involving two collision events is depicted in Figure 2.6. In this case a primary ion direct recoils a surface atom (m_2), which scatters of another surface atom (m_3).

For the double collision, the surface recoiling energy (E_{SR}) can be approximated using equations 2.1 and 2.3. As with MS, the SR energies for a particular surface

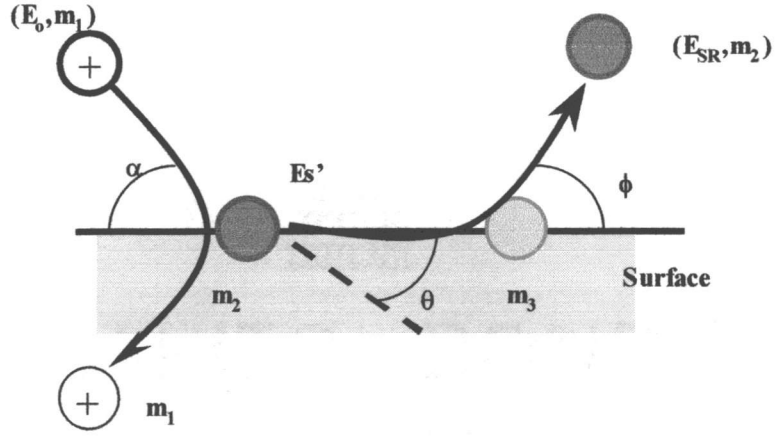

Figure 2.6 Schematic of surface recoiling (SR): two collision events

atom tend to be greater than that of DR. SR typically occurs with lighter atoms, such as hydrogen, scattering off heavier surface atoms and is enhanced at grazing angles (i.e. small α).

2.3 INELASTIC EFFECTS: IONIZATION AND EXCITATION

Up to this point, the collision discussed have been limited to those that are elastic in nature. However, atoms and ions are not hard spheres. For distances of close approach, the atomic collisions may result in the overlap of atomic orbitals. Such overlaps can lead to inelastic energy losses in the form of excitation and ionization of either species.

Excitation processes are common for atomic collisions in the keV range, and are observed as a photon peak in the DRS spectra. Excitation applies to all ion-surface interactions and is dependent on the impact parameter (p) [32]. Olsen et al. [56] conducted experiments in the collision of Na^+ with stationary Ne atoms between the incident energies of 0.2 and 12 keV. Their data indicated that when p >1.63 Å, the collision is purely elastic, and when p <1.63 Å excitation occurs.

Ionization is not only dependent on p, but also on the degree of ion-surface combination [52] that occurs, leading to neutralization. Several possible charge transfer processes are possible, including: a) resonant surface-to-particle (ion) charge transfer, b) resonant particle-to-surface charge transfer, and c) Auger surface-to-particle charge transfer.

The type of event occurring depends on the ionization energy potential of the ion (I), and the work function of the surface (Φ). For example, when the ionization energy of the ion (for He, $I = 24$ eV) is larger than the surface work function, the ion can be neutralized during the distance of closest approach [5]. In such a case, an electron from the conduction band of the surface can tunnel into the ion, neutralizing it. The excess energy associated with the process can be removed by ejection of a

second electron from the surface by a process similar to the Auger de-exictation process (case c, above).

In the ionization of DR species, the percentage of DR ion particles is highly dependent on the identity of the incident ion and surface atom, and the incident energy. With noble gas ions colliding with a metallic surface, the ion fractions range from 0 % to 80 % with the upper limit corresponding to higher incident energies [32]. For alkali ions the fraction can exceed 85 % at higher energies. However, for most non-metallic surface species this fraction is low, and the DR species are predominantly neutral.

In addition, the magnitude of the inelastic energy loss, either through excitation or ionization, is small when compared to the kinetic energy transferred in the collision process [52]. Such inelastic effect appears as an extra degree of broadening and tailing on the low-energy side of the scattering or recoiling peaks. For inelasticially DR species, the energy (E_{DR}') can be determined by [32]

$$E_{DR}' = [(m_2/m_1)E_o/((m_2/m_1)+1)^2]\cos^2\phi \qquad 2.6$$

This equation shows that at smaller recoil angles the inelastic (low energy) DR component can be separated from the elastic DR component by an amount of energy on the order of 1 eV.

2.4 COLLISION CROSS SECTIONS

Section 2.2 described the kinetic energies of the scattered or recoiled particles with respect to an outgoing trajectory. However, not every ion that approaches a surface with a particular incident angle will result in a collision into a given trajectory towards the detector. The concept of cross section (σ) is introduced as the probability of scattering or recoiling at a particular outgoing angle. Because the

colliding pairs are not hard spheres as described by BEC, to describe such probability correctly, the interatomic potential must be considered. Furthermore, as the collisions are in three dimensions, the solid angle ($d\Omega$) is necessary in the derivations of σ.

2.4.1 Mathematical description of the center-of-mass cross section

The mathematical description of the cross section is typically carried out in the center-of-mass (CM) frame (i.e. both projectile and target have a measurable velocity). For an incident ion approaching a surface atom, at p and Eo, the probability that it will scatter into the angular region $d\Omega$ between the CM scattering angle θ and $\theta + d\theta$ is given by [53]

$$\sigma\,(\Omega)_{CM} = d\,\sigma/d\,\Omega = |\,(p/\sin\theta)(d\,p/d\,\theta)| \qquad 2.7$$

This differential cross section ($\sigma\,(\Omega)_{CM}$) has units of $Å^2$, and as illustrated in Figure 2.7 can be viewed as an effective area presented by the scattering center (m_2) for deflection between θ and $\theta + d\theta$ [57].

The CM scattering angle, also know as the scattering integral, is dependent on the atomic potential between the projectile m_1 and the target m_2 at separation distance r, and the impact parameter p. The form of the integral is given as [57]

$$\theta = \pi - 2\,p \int_R^\infty dr / (\,r^2\,g(r)) \qquad 2.8$$

whereas R is the distance of closest approach between the collision partners, and g(r) is given as [57]

$$g\,(r) = (1 - p^2/r^2 - V(r))^{1/2} \qquad 2.9$$

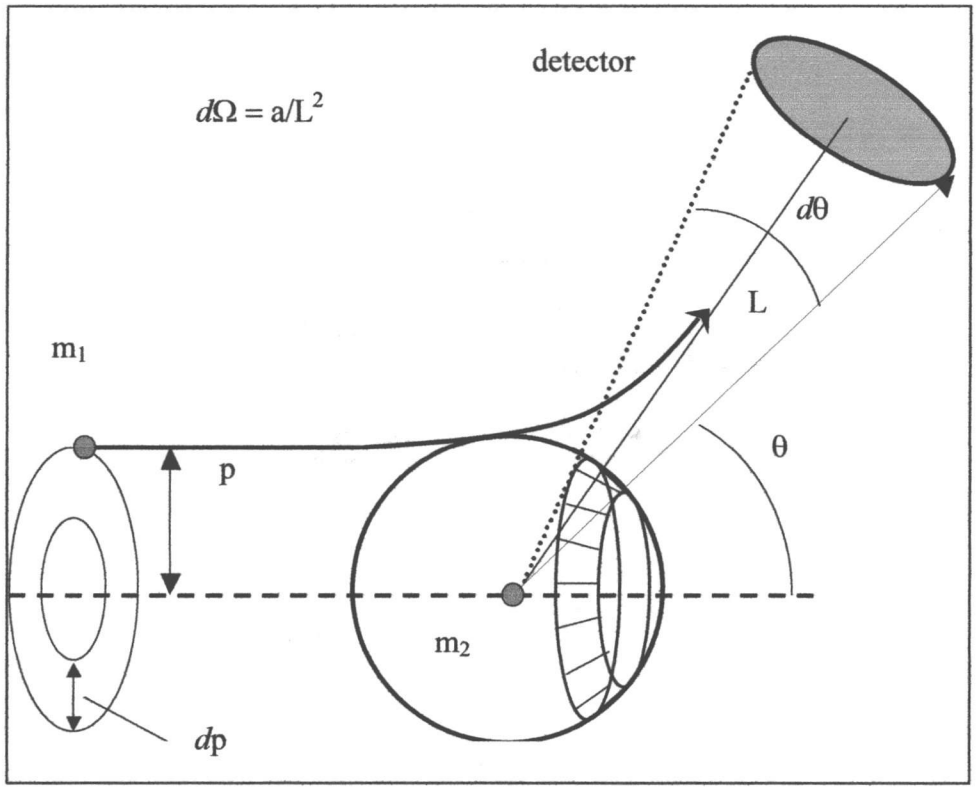

Figure 2.7 The relationship between the impact parameter (p), the CM scattering angle (θ), and the solid angle dΩ: L = the distance to the detector, and a = the surface area of the detector.

The value of $\sigma\ (\Omega)_{CM}$ obtained in these calculations is highly sensitive to the interaction potential (V(r)) used. At higher incident energies (E_o >100 keV), the ion approaches sufficiently close to the target atom such that the repulsive portion of the Coulombic potential dominates the Van der Waals attraction can be neglected [52]. However, at the energies involved in DRS (E_o <10 keV) the screening effects from the electron clouds, which partially effects the Coulombic potential has to be accounted for. Several modifications of the Coulombic potential have been proposed for scattering calculations, including the Moliere potential [56]. However, the one that has provided particularly good agreement with experimental data is that of the

Universal Interatomic Potential developed by Ziegler, Biersack, and Littmark [32]. It has the form of

$$V(r) = (Z_1 Z_2 e^2/r)[0.1818\, e^{(-3.2X)} + 0.5099\, e^{(-0.9423X)} + 0.2802\, e^{(-0.4028X)} + 0.02817\, e^{(-0.201X)}] \quad 2.10$$

where Z is the atomic number of a collision partner, e is the elementary charge, and

$$X = [r\,(Z_1^{0.23} + Z_2^{0.23})] / [(0.8854)a_o] \quad 2.11$$

However, in the case of the events involved in DRS, the target is stationary and therefore a transformation of the CM cross section into the LAB frame is required. The transformation of $\sigma\,(\Omega)_{CM}$ to the LAB frame scattering cross section $\sigma\,(\theta)_{LAB}$ is given as [32]

$$\sigma\,(\theta)_{LAB} = \sigma\,(\Omega)_{CM}\, \frac{[(m_1/m_2)\cos\theta + (1 - (m_1/m_2)\sin^2\theta)^2}{(1 - (m_1/m_2)\sin^2\theta)^{1/2}} \quad 2.12$$

The LAB frame recoiling cross section $\sigma\,(\phi)_{LAB}$ is calculated by

$$\sigma\,(\phi)_{LAB} = 4\,\sigma\,(\theta)_{CM}\cos\phi \quad 2.13$$

2.4.2 Effects of experimental parameters on the cross section

Both the recoiling and scattering cross sections are dependent on experimental factors such as primary energy, projectile/target mass, and scattering/recoiling angles. The trend for the scattering cross section is a decrease with decreasing E_o and θ, and to increase with m_2. For a given m_2, the direct recoiling cross section

increases with recoiling angle (ϕ) and with m_1, and E_o. For a given m_1, the DR cross section increases with m_2. The dependences of the DR cross section on such experimental parameters are illustrated in Figures 2.8, 2.9, and 2.10.

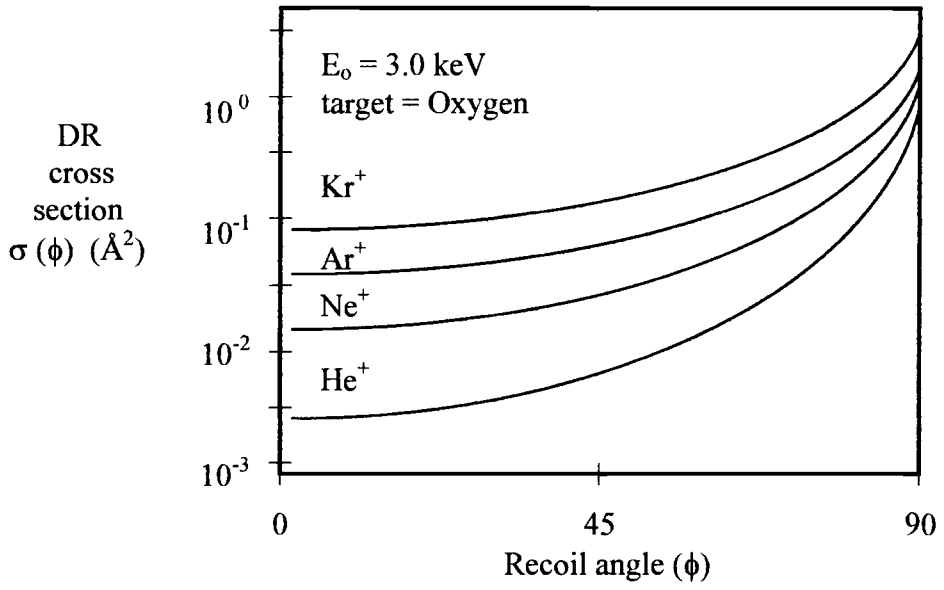

Figure 2.8 DR cross section as a function of recoil angle for oxygen atoms recoiled by various 3 ke-V noble gas ions.

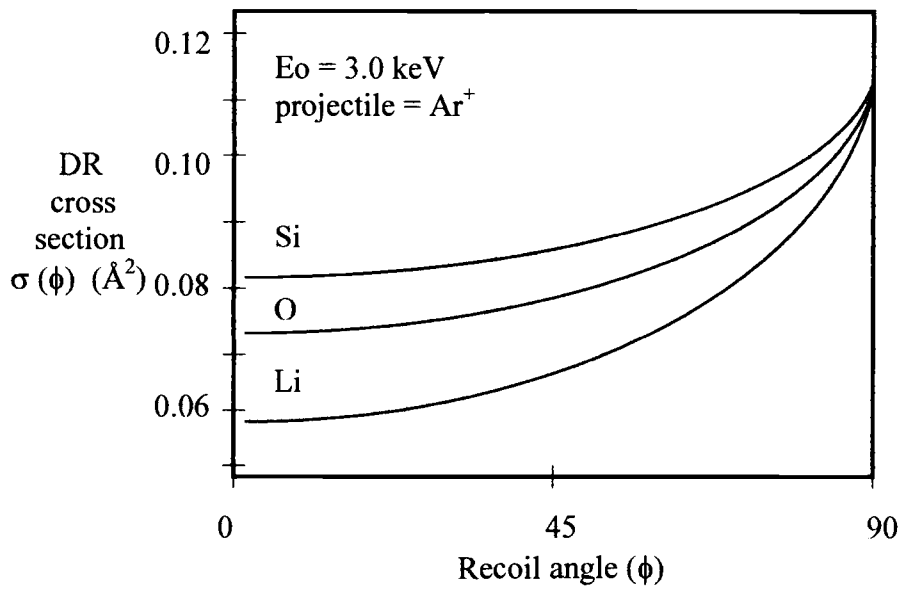

Figure 2.9 DR cross section as a function of recoil angle for various target atoms recoiled by 3 ke-V Ar^+ projectiles.

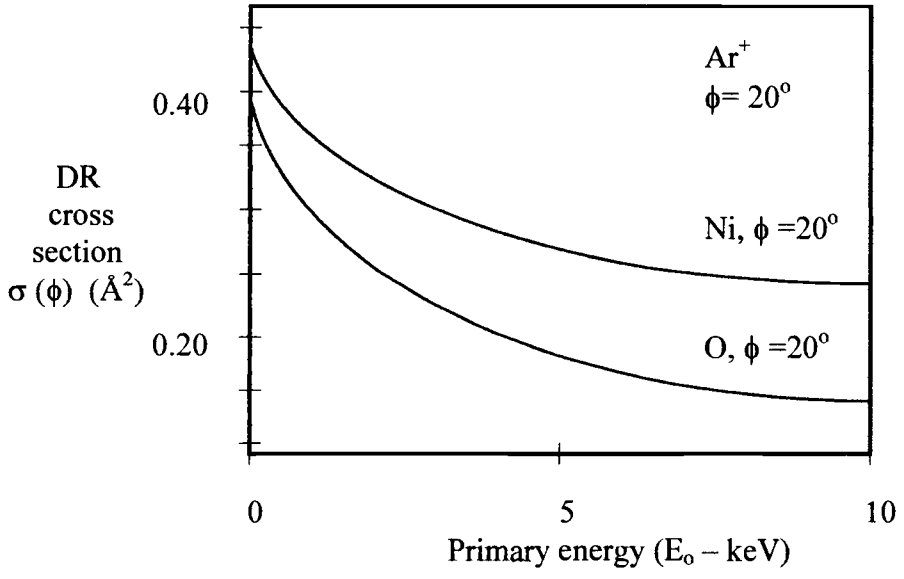

Figure 2.10 DR cross section as a function of primary energy for various target atoms recoiled by Ar^+ projectiles at a recoil angle of 20°.

2.5 SHADOWING AND BLOCKING

Both the kinematics described by the BEC model and the cross section calculations assume that the projectile and outgoing species only interacts with one atom in the course of the trajectory. The scattering/recoiling kinematics and dynamics increases in complexity when the target consists of multiple atoms. This is always the case with real solid and liquid surfaces. For the collision events to be treated as binary collisions, the projectile must possess sufficient kinetic energy, and the scattering/recoiling cross sections must be small with respect to the interatomic area between neighboring target atoms [18]. When such is not the case, shadowing and blocking events will result in anisotropy in the yield of scattered or recoiled particles.

In shadowing effects, the parallel flux of primary ions is deflected away from a region behind a target atom. In the case of $m_1 < m_2$, a small fraction of the ions are backscattered. But in all cases the majority of the ions are forward scattered. The region behind the target is known as a shadow cone, and is illustrated in Figure 2.11. As a result of shadowing neighboring atoms in this region are excluded from collision events. Those that are at the border of this region can have a flux of projectiles focused upon it [18]. Blocking, as shown in Figure 2.12 can be thought of as the inverse of shadowing. Typically, the outgoing trajectory of the divergent scattered or recoiled particles will be affected by an encounter with other atoms, which will 'block' its path out. Such effects on trajectories are typically observed in deviations in scattering and recoil intensities. But they are incorporated into trajectory tracing programs such as MARLOWE for solid substrates.

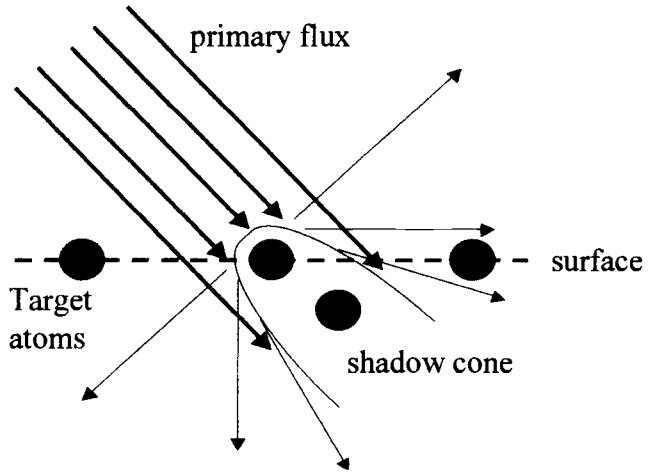

Figure 2.11 Schematic of shadowing with respect to the incident ion beam at the surface

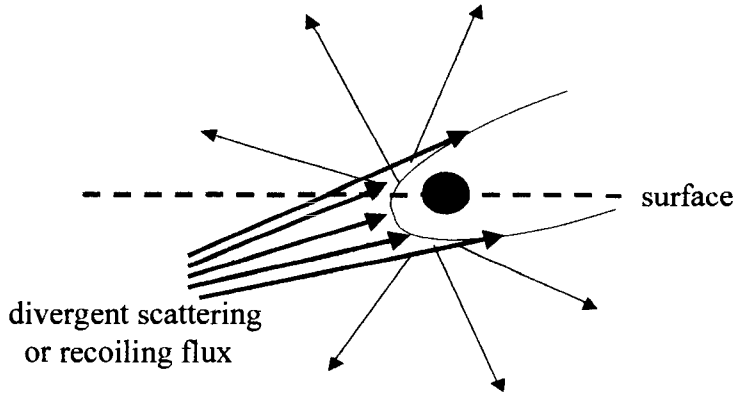

Figure 2.12 Schematic of blocking with respect to the divergent beam of scattered or recoiled particles

3.EXPERIMENTAL

3.1 DESCRIPTION OF DIRECT RECOIL SPECTROMETER

This work and those of previous graduate students have demonstrated the successful design, construction, and operation of a direct recoil spectrometer designed for liquid samples. The spectrometer design used in this laboratory was based on the instrument used by the Rabalais group at the University of Houston [32] for solid samples. Many of the details of our spectrometer's design and performance have been described elsewhere [50,51]. The purpose of this section is to give a general description of the spectrometer, which is shown schematically in Figure 3.1. Such a discussion will cover the four important systems associated with the spectrometer: the ion source, the ion optics, the sample cell, and the particle detector.

3.1.1 Ion source

The incident ions are generated by an ion-sputtering gun (OCI Vacuum Micro-engineering, Model IG 35/70) that contains both an ion source and ion focusing elements. The inert gas ions are produced via hot cathode electron impact, and then are accelerated and focused by electrostatic lens before exiting the gun. The gun is controlled by a power supply (OCI, Model IPS3) that allows for beam energies of up to 3.0 keV. At the maximum energy, the beam current is 15 μA with 5.0×10^{-6} torr of Ar .

3.1.2 Ion optics

The ion optics serves to select ions of proper mass and velocity, to focus the beam, to direct the beam towards the target, and to pulse the beam in order to collect

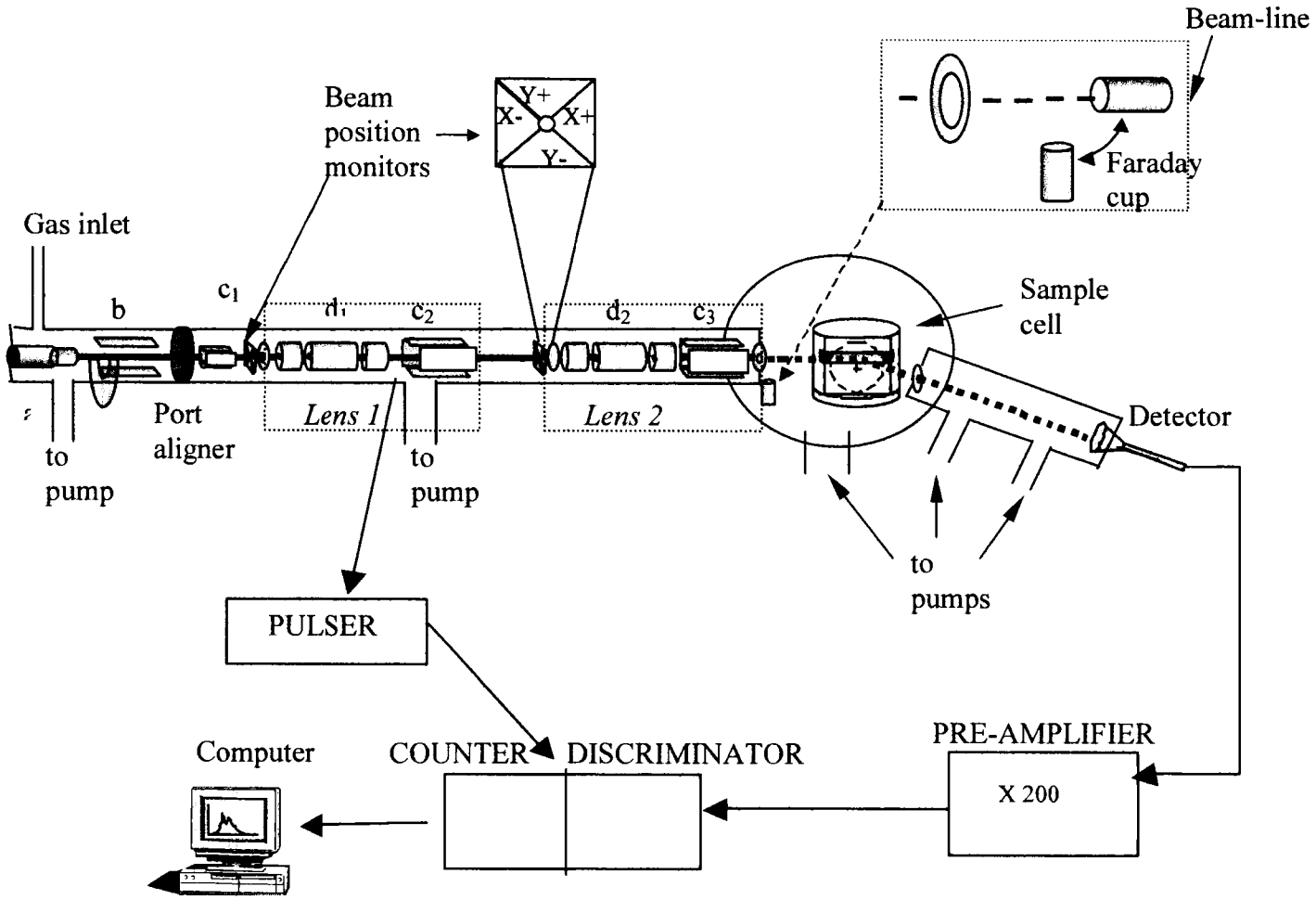

Figure 3.1 Schematic diagram of direct recoil spectrometer: a-ion source, b-Wien filter, c1- 1st deflection plates (X/Y-pos) , d1- Einzel lens for lens 1 assembly (L1), c2 – deflectors for lens 1 (X1/Y d2 –Einzel lens for lens 2 assembly (L2), and c3 – deflectors for lens 2 (X2/Y2)

TOF information. The system is composed of three sets of X-Y deflection plates, two Einzel lens, and a Wien filter, with two main collimating regions called lens 1 and lens 2.

The ions are mass and velocity selected to produce a beam of monochromatic ions by the Wien filter. Mass selection is carried out by the magnetic field from a 1200 Gauss magnet, while velocity separation is carried out by an applied electric field from two horizontal plates. The filter does not remove neutral particles within the beam. Positioning the ion gun off axis using the port aligner separates the neutrals by forcing them to miss the initial aperture that defines the ion beam.

The X-Y deflection plates use applied potentials to direct the ion beam towards the target. The maximum voltages are 200 V (X/Y-pos), 250 V (X1/Y1), and 50 V (X2/Y2). The X1/Y1 deflectors are also capable of providing a pulsed beam that is controlled by the pulse generator (Avtech AVR-G1-PC-OSU3). The deflectors in each lens assembly are complimented by a set of Einzel lens. These cylindrical lenses use a large positive potential to focus the beam towards center of the beam line. The maximum potential of each lens (L1 and L2) is 5 kV.

Beam current is measured at various test points in the ion optics region. These current monitors serve as guides in the directing and focusing of the ion beam. The beam position monitors are located between the X/Y-pos deflectors and lens 1, and between the two lens assemblies. Each monitor consists of four regions labeled X+, X-, Y+, and Y-. The ion beam current is also measured immediately in front of the target by a retractable Faraday cup.

3.1.3 Sample cell

A schematic of the liquid sample cell is shown in Figure 3.2. The sample cell is maintained within an ultra-high vacuum chamber ($\sim 10^{-6}$ torr) that was designed such that the scattering and recoil angles are fixed ($\theta = \phi = 45^{o}$). The cell was constructed

such that incident beam angle can be varied, sample evaporation is minimized, and the liquid surface is continuously refreshed.

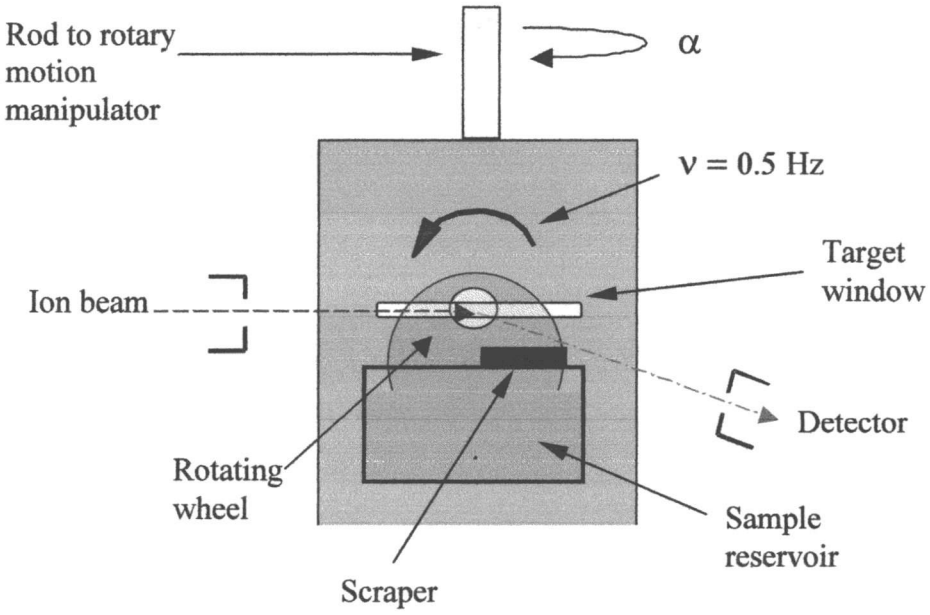

Figure 3.2 Schematic of DRS liquid sample cell

As shown in Figure 3.2, the liquid sample is contained within a reservoir that holds ~30 mL. This volume can be reduced to ~10 mL by placing Teflon within the reservoir. A liquid surface is generated on a rotating stainless steel wheel (ν = 0.5 Hz) that moves a liquid layer past a scraper to produce a film with a thickness of about 0.2 mm. This wheel also helps to minimize the adsorption of contaminants and sample charging by continuously generating a fresh surface. A target window of approximately three-square centimeters exposes the liquid surface to the ion beam. Such a limited vacuum exposure reduces the evaporation of the liquid. The rotary motion manipulator allows for the entire cell to rotate about an axis normal to the ion beam axis, therefore allowing for the angle of incidence.

3.1.4 Detection assembly

The detection assembly consists of the detector and data acquisition system. The detector used in the spectrometer is a continuous channel electron multiplier (CEM) that is attached to the data acquisition system consisting of a pre-amplifier (EG&G Ortec, VT120), and a multichannel scaler (EG&G Ortec, Turbo MCS). The CEM (Detector Technology, Detech 407-EIC) is capable of detecting electrons, photons, and both charged and neutral particles. In the pulse counting mode, it has a gain of 10^7 to 10^8. The MCS serves as a counter of the particles reaching the detector and a discriminator of electronic noises.

The detection assembly, along with the pulse generators, is essential in obtaining a TOF spectrum. Upon the creation of an ion pulse, the pulse generator sends a trigger output signal to the MCS. This signal is delayed by the time required for the pulsed beam to reach the target, after which the MCS begins the counting of input events. The collision of the recoil and scattered particles with the CEM creates such input signals, which are amplified and serves as a stop signal for the MCS. The MCS then sends a histogram of counts to a personal computer, which produces a TOF-spectrum using manufacturer-provided software.

3.1.5 Miscellaneous

During the course of the experiment the spectrometer is kept under high vacuum. In the region containing the ion optics, the sample chamber, and the TOF arm, the majority of the pumping is provided for by diffusion pumps (DP). While the region containing the detector used a turbomolecular pump (TMP), and that of the ion gun used a molecular drag pump (MDP). Both the DP and TMP offer the distinct advantage of running without fluids, preventing contamination of the systems from backstreaming of fluids. Furthermore, the vacuum system was designed such that

efficient differential pumping is achieved between the chamber, and both the ion optics and detector regions. In differential pumping, each region is physically separated by small diameter apertures. This produces a pressure gradient, which restricts flow of gas from the chamber to other regions, and minimizes the contamination to the source and the detector.

3.2 EXPERIMENTAL: OPERATION OF THE SPECTROMETER

In order to obtain a liquid surface DR spectrum, the spectrometer must be brought to high vacuum and the ion source must be initialized. As shown in Figure 3.3, the operation of the spectrometer involves a series of procedures that must be carried out in sequence. The procedures include

- *Prestart*: cleaning and reassembling the sample cell, filling it with the sample liquid, and then securing it into the sample chamber.
- *Initial pumpdown*: rough pumping of the spectrometer using only the rotary and turbomolecular pump. Once the backing pressures are adequate, the ion gun is baked out for ~ 12 hours to expedite outgassing. Diffusion pumps are not turned on to prevent contamination of sample by backstreaming of diffusion pump fluid.
- *Final pumpdown*: diffusion pumps are used to bring spectrometer to operating pressures (~ 10^{-6} torrs in sample chamber).
- *Ion gun initialization*: the filament current is slowly increased to remove contaminants from filament, and the nominal operating current (~2.5 –3.0 A) is allowed to stabilize.
- *Beam optimization*: to direct and focus a continuous ion beam towards the target using the optics system such that current is maximized . The beam is then pulsed and re-optimized.

The procedure for initializing the ion gun remains unchanged and will not be discussed in this section. The procedure has been previously mentioned [50] and can also be found in the TOF-SARS Users Manual. However, the optimization procedure for the ion beam has been modified for efficiency and will be discussed in this section.

3.2.1 Beam optimization: continuous current

Previously the optimization or collimation of the beam was a "trial-and-error" affair requiring 2-5 hours. With the addition of the beam position monitors, we were able to modify the procedures, reducing the optimization time to 2 hours or less. This process is carried out each time when a sample is changed, a new ion or beam energy is used, the gun is moved, or when there is a prolonged period between data acquisition for a particular experiment. The beam current that reaches the target can be effected by: a) the electron emission current of the source, b) partial pressure of the inert gas, and c) the applied potentials to the optical elements.

Before beam optimization with the optics system, the user should optimize both the gas pressure and the emission current (I_e). Both I_e and the partial pressure are directly proportional to ionization efficiencies (ions/atoms) [18] as well as the beam current. The general starting points for the I_e and the partial pressure are given in Table 3.1. Changing the filament current can vary the emission current. However, the amount of increased current is limited by the lifetime of the filament. A filament current exceeding 3.0 A to obtain the desired emission current indicates a filament near the end of its lifetime. Gas pressures should not exceed the values given below. While a higher pressure will produce more ions, the mean free path of the ions is decreased, making it more difficult for extraction and collimation.

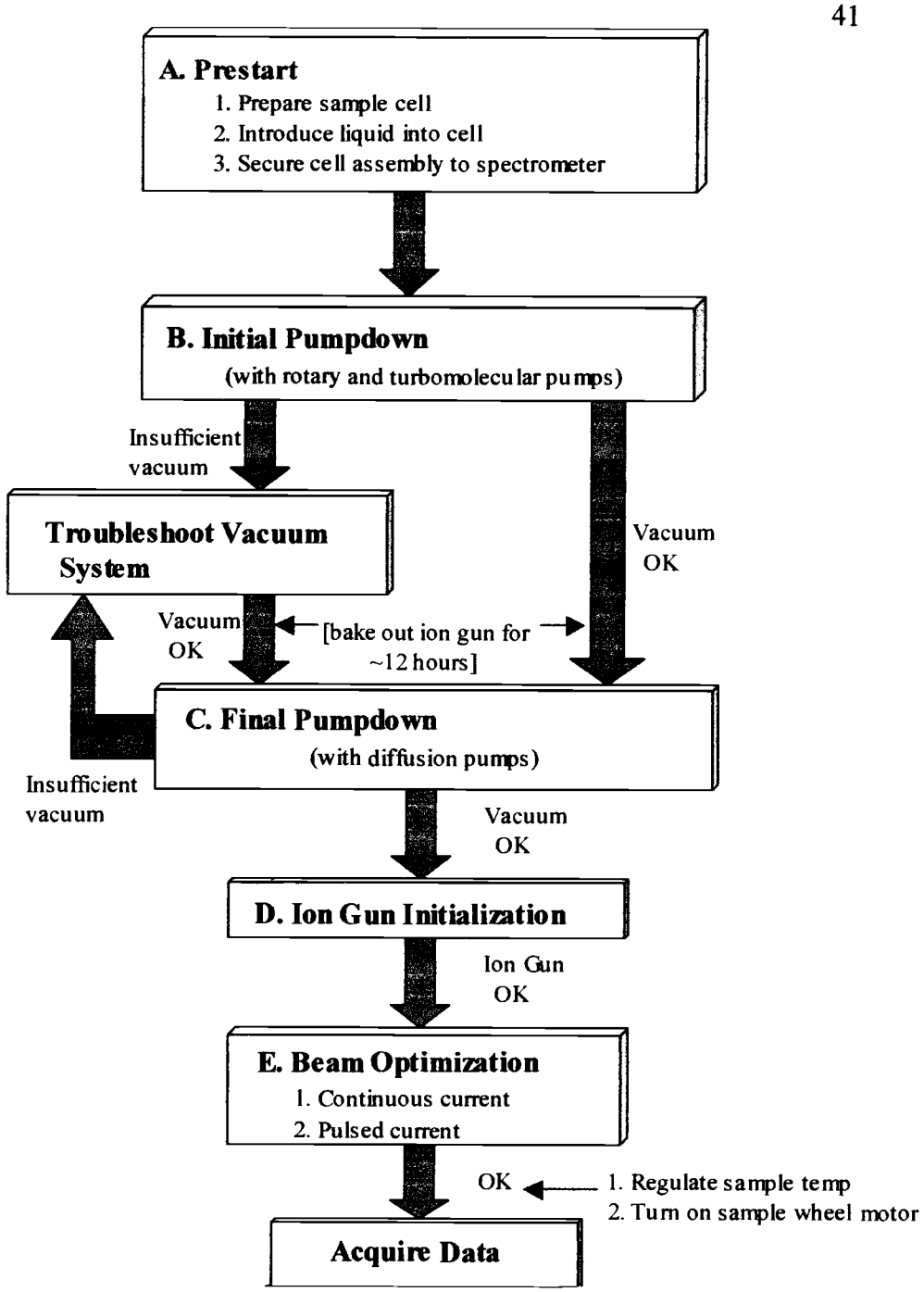

Figure 3.3 Overview of spectrometer operational procedures before data acqusition

Table 3.1 Approximate values of I_e, gas pressures, and Wien filter settings for beam optimization

Ion	E_o (keV)	I_e (mA)	Gas pressure* (mm Hg)	Wien filter (V)
Ar^+	2.50	30 - 35	10 - 12	165
Ne^+	2.00	35 - 40	12 - 15	210

* Measured with thermocouple gauge below ion gun

Once the emission current and gas pressures have stabilized, the port aligner should be aligned to a 2° offset, and appropriate potentials for the Wien filter, with magnet in place, should be dialed in. The total current from the previously mentioned test points should be then determined. For a 2.5-keV Ar^+ beam the total current should be 550 nA or greater, while for a 2.0-keV Ne^+, it should be 350 nA or greater. The continuous current should then be monitored using the first set of beam position monitors, and the ion gun focus and the position of the gun magnet are then adjusted to maximize the total current at this test point.

Ideally, once optimized, the ion beam should be uniform in current density and symmetrical at each of the first two test points. However, this cannot be achieved without an additional Einzel lens between the gun and the first set of monitors. Therefore, the current profile is only important at the second set of monitors. Once the current is maximized at the first test point, the beam is deflected before using the X/Y-pos deflectors such that much of the current is directed towards the X_1+ and Y_1+ quadrants of the beam monitors. For example, with a 2.5-keV Ar^+, a typical X_1+/X_1- current ratio can be 10:1 while for Y_1+/Y_1- can be 20:1. There are no rough

starting points for the potentials of X/Y-pos deflectors, but generally the user can start with the settings from the previous experiment.

Once this has been achieved the lens 1 assembly is used to collimate the beam, such that the current measured at the second set of beam monitors is uniform with the X_1+/- (Y_1+/-) current ratio is ~1:1, and X/Y current ratio ~1:1. Fine-tuning of the settings for the first deflectors, as well as the lens 1 assembly may be necessary to achieve this. The lens 2 assembly is then used to direct and focus the beam towards the target. The shield and the Faraday cup monitor the beam collimated by this optics region. Typical beam currents measured by the Faraday cup range from 35-50 nA for 2.5-keV Ar^+, and 25-35 nA for 2.0-keV Ne^+. Beam currents of less than 20 nA may make it difficult to maximize the pulsed beam current. As a guide, the rough range of settings for the component of the lens 1 and lens 2 systems are given in Table 3.2. Some combination of settings between the given values is typically sufficient to optimize the continuous beam.

Table 3.2 Approximate ranges of settings for the ion optics system

Lens 1	Ar^+ (2.5 keV)	Ne^+ (2.0 keV)	*Lens 2*	Ar^+ (2.5 keV)	Ne^+ (2.0 keV)
X1 (V)	-31 to +27	-1 to +35	X2 (V)	-13 to 0	-17 to 0
Y1 (V)	-34 to +28	-31 to +23	Y2 (V)	+9 to +45	+16 to +41
L1(kV)	1.24 to 1.44	1.08 to 1.22	L2(kV)	1.78 to 1.85	1.40 to 1.48

3.2.2 Beam optimization: pulsed current

After the continuous beam current has been optimized, the beam must be pulsed in order to obtain a spectrum. As shown in Figure 3.4, sweeping the beam in a

square-like pattern across the aperture produces the pulse. Initially, the continuous beam is directed downwards with an applied potential from the Y1 deflectors. The X1/Y1 deflectors are then used to sweep the beam across the aperture to determine the output voltages from the Avtec pulser. The operation of the pulser to optimize the pulsed current has been previously described. However, it is suggested that the pulsed current be monitored using both the Faraday cup and the particle detection system (i.e. Turbo-MCS). A typical pulsed currents for a 2.0-keV Ne^+ beam is $\geq$50 pA (S/N~25:1), which corresponds to a reading of ~25,000 counts with the Turbo-MCS at angle of incidence of 28°. While for a 2.5-keV Ar^+, the current is typically $\geq$100pA (S/N~50:1), with 50,000 counts.

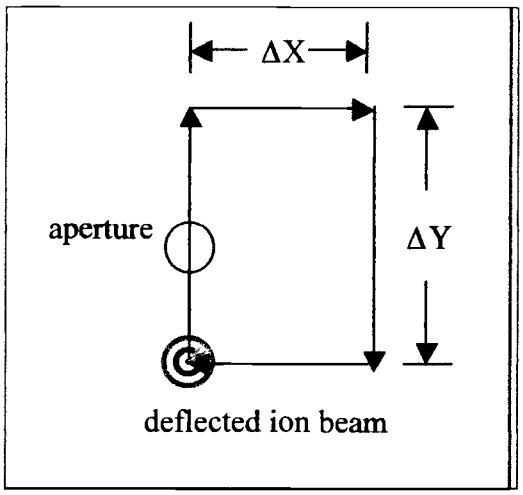

Figure 3.4 Ion beam pulsing scheme: ΔX = potential applied from X1 deflector plates, DY = potential from Y1 deflector plates.

3.3 DATA ANALYSIS

3.3.1 Spectral deconvolution

The qualitative identification of surface atoms from the recoil spectra is generally straightforward and can be carried out by comparing the measured TOF with those calculated from the equations mentioned in Chapter 2. Quantitative analysis requires relating the true or absolute signal intensities of DR to the surface atom density. However, this is made difficult from the overlapping of peaks from various surface

collisions, and the long tail associated with each peak. Simulations from this laboratory have confirmed that recoils with longer TOF, located in the tail, results from complex multiple–collision processes and is most likely not directly correlated to its depth of origin [33]. Furthermore, 50-75% of the recoil signals originate from the top 1 Å of the molecular layer of the liquid. Hence, the intensity of a DR signal for a particular atom is proportional to the atomic concentration at the surface. Therefore, an important first step in obtaining quantitative information from the spectra is to extract the true signal intensities by spectral deconvolution using the PeakFit™ Software (Jandel Scientific, Version 4).

The details of the deconvolution of the DR spectra are described in the PeakFit™ user's manual [34]. Several steps are taken before the spectra is "fitted" including

- the calibration of the spectra with the photon peak as time zero (e.g. 0 μs)
- the MCS file (*.mcs) is converted to an appropriate ASCII format (*.txt, *.dat or *.prn)
- the ASCII file is imported into PeakFit, and it is smoothed using Fast-Fourier Transform (FFT)

The individual spectral peaks are fitted, using modified Gaussian functions, through the second derivative option using a Savitsky-Golay algorithm. The functions were either chosen from the software's library or formulated from available functions, so that it could adequately describe the major portion of a recoil peak as well as the long tail. In the case of the non-hydrogen recoil and multiple scattering peaks, we found that exponentially modified Gaussian (EMG) functions to be sufficient in this task. The function is given as

$$F(x) = (a_0/2a_3)\exp[(a_2^2/2a_3^2)+ ((a_1-x)/a_3)][1+ \mathrm{erf}\{(x-a_1)/(2a_2)^{0.5} - a_2/(2a_3)^{0.5}\}] \quad 3.1$$

where a_0 is the peak area, a_1 is the peak center, a_2 is the peak width at half maximum, a_3 is the asymmetry, and x is the TOF. For a user-formulated function consisting of

the sum of two EMG was used to describe the hydrogen recoil peak. This function is described by

$$F(x) = (a_0/2a_3)\exp[(a_2^2/2a_3^2)+ ((a_1-x)/a_3)][1+ \mathrm{erf}\{(x-a_1)/(2a_2)^{0.5} - a_2/(2a_3)^{0.5}\}]$$
$$+ (b_0/2b_3)\exp[(b_2^2/2b_3^2)+((b_1-x)/b_3)][1 + \mathrm{erf}\{(x-b_1)/(2b_2)^{0.5} - b_2/(2b_3)^{0.5}\}] \quad 3.2$$

The first EMG describes major portion of the peak and the second EMG describes the tail. The parameters of the second function are scaled quantities of the first EMG, and are unique to the ion and energy in which the spectra was obtain. The relationships of the parameters in Equation 3.2 are given in Table 3.3.

Table 3.3 Relationship among parameters in Equation 3.2

	b_0	b_1	b_2	b_3
2.50 keV Ar^+	$0.63a_0$	$0.86a_1$	$1.69a_2$	$4.5a_3$
2.00 keV Ne^+	$0.63a_0$	$1.16a_1$	$1.69a_2$	$5.0a_3$

Initially, we allowed the software to automatically fit the individual peaks in a spectrum simultaneously. Unfortunately, such a method was ineffective because PeakFit^{Tm} tends to automatically fit the peaks without regards to the consistency of peak shapes, widths, and position of peak centers, and would generally produce fits where the peaks were shifted with respect to their predicted TOF. In order to overcome this, the hydrogen peak was isolated from the rest of the spectrum so that the major portion of the peak (ignoring the long TOF tail) is auto-fitted. Once this is done the parameters for the hydrogen function are constrained, and the other peaks are fitted using EMGs with constrained widths. This method allows for a reasonable and reproducible means for deconvolution of the overlapping peaks, without extreme shifts of the individual TOFs. For the spectra with low S/N ratios, reasonable errors limits for the fitted signal intensities of roughly $\pm$10% were typical.

3.3.2 Atomic ratios

Once the true signal intensities have been obtained, we can carry out the quantitative analysis. In the single scattering limit, the relationship of true spectral intensity from the direct recoil of an atom (I_i) to the surface density (N_i) is given by [18]

$$I_i = J_o \Delta\Omega \varepsilon_i \sigma_i N_i \qquad 3.3$$

where J_o is the incident ion beam density, $\Delta\Omega$ is the solid angle accepted by the detector, ε_i is the detector efficiency for atom i, and σ_i is the recoil cross section for atom I.

The detector efficiency is a function that is dependent of the particle atomic number (Z) and velocity (v). The expression is given as

$$\varepsilon_i = a\,(v - v/Z^c)\,Z_i^n \qquad 3.4$$

The constants have been determined in our laboratory for the CEM, with $a = 2.6\text{x}10^{-6}$ s/m, $b = 7.8\text{x}10^4$ m/s, $c = 0.26$, and $n = 0.39$ [51]. The DR cross-sections are generally calculated from standard computer codes but we have found that the cross section for hydrogen is overestimated in such calculations. The cross-sections between hydrogen and other atoms need to be reduced by 50% to correlate the simulations with experiments [33]. The dependence of the recoil cross sections on ion energy of both Ar^+, and Ne^+ was determined for various atomic species, including hydrogen. Examples of σ_i values are shown in Table 3.4, and these values were calculated from expressions that can be found in Appendix A.

Table 3.4 Examples of recoil cross sections (σ_i) for recoiling from 2.50-keV Ar^+ and 2.0-keV Ne^+

	2.50-keV Ar^+	2.00-keV Ne^+
σ_H (Å^2)	1.44	0.658
σ_C (Å^2)	1.80	0.870
σ_N (Å^2)	1.83	0.906
σ_O (Å^2)	1.86	0.941
σ_F (Å^2)	1.82	0.948

In DRS, surface compositional information is determined by surface atomic ratios. By taking the ratios of the intensities of two atoms i and j, the beam density and solid angle terms drop out, and the surface atomic ratios is determined by

$$N_i/N_j = (I_i\ \varepsilon_j\ \sigma_j)/\ (I_j\ \varepsilon_i\ \sigma_i) \qquad 3.5$$

Taking ratios eliminates the need to experimentally determine J_o and $\Delta\Omega$.

3.3.3 Surface orientation simulations

To determine the surface orientations, the atomic ratios are compared to the numbers of atoms accessible to the ion beam as calculated by a computer code known as Line-of-Sight (LOS). This program was developed in our laboratory. Prior to using the code, the molecule of interest is constructed and the geometry is optimized (with molecular mechanics calculations) using Hyperchem^{TM}. Once

optimized, the relative coordinates of the atomic centers are inputted into a computer program, known as Rotate, in order to orientate the molecule by rotation with respect to the x-, y-, and/or z-axis. The new coordinates are saved as a text-format file that is compatible to LOS. The LOS calculations take into account the mean intermolecular separation and the small random vertical surface molecular fluctuations, and then simulate the number of atoms that impinged by ions and the number that encounter intramolecular blocking over a 360° azimuthal rotation. Such azimuthal averaging is important because the number of atoms, at a given orientation, that is "seen" by the ion beam and the number that encounter blocking varies based on the direction of approach. The atomic ratios are determined from the number of atoms that are effectively "hit."

4. INVESTIGATION OF THE SURFACE ORIENTATION AND COMPOSITION OF ROOM TEMPERATURE IONIC LIQUIDS

4.1 INTRODUCTION

This chapter describes the DRS experiments carried out on neat ILs containing the 1-C_nH_{2n+1}-3-methylimidazolium cation $[C_nmim]^+$. The significance and purpose of this work was discussed in Chapter 1. As mentioned, the initial experiments were carried out on the air-and-water stable 1-butyl-3-methylimidazolium hexafluro-phosphate $[C_4mim][PF_6]$[36]. The results for this IL indicated that normal stoichiometry is maintained at the surface (e.g. no surface segregation). Also from DRS it was inferred that the $[C_4mim]^+$ cation adopts a preferential orientation with the imidazolium ring vertical such that the nitrogen atoms and alkyl substituents penetrate deeper within the surface. By examining others in this class of ILs, we were able to determine how the length of the 1-alkyl change and/or the identity of the anion affects the surface composition and orientation.

4.2 PROPERTIES OF IONIC LIQUIDS

The ILs examined have the general formula of $[C_nmim][X]$, where n = 4, 8, and 12, and X = PF_6^-, BF_4^-, Cl^-, or Br^-. Many of their bulk physical properties, including melting point, density, and viscosity, have been reported [59]. Studies on their polarities [60,61], and conductivities [61] have also been carried out. These studies are generally in agreement that many properties can be controlled to a large degree by variation in the nature of both the cation and the anion, or by creating mixtures of ILs. Examples of some properties of the $[C_nmim][X]$ ILs are shown in Table 4.1. The phase transition temperature (T_{trans}) in the table is given for transitions either from crystalline solid to liquid (C-> L), crystalline solid to smectic-A liquid crystal

(C- > S_A), or glass to liquid (g- > L) [62,63]. E_{NR} is the molar transition energy of the solvatochromic dye Nile Red in the IL, where an increasing value indicates decreasing polarity of the IL [59].

Table 4.1 Properties of [$C_n$mim][X] ionic liquids

	Molar Mass (g/mol)	Density (g/cm^3) [58]	T_{trans} (°C) [62,63]	E_{NR} (kJ/mol) [59,60]
[C_4mim][BF_4]	226.03	1.17 (30°C)	-81 (C->L)	217.2
[C_4mim][PF_6]	284.19	1.38 (30°C)	-61 (C->L)	218.5
[C_8mim][BF_4]	282.14	1.07 (60°C)	-78 (C->L)	217.7
[C_8mim][PF_6]	340.29	1.25 (22°C)	-70 (g->L)	217.6
[C_8mim][Br]	230.78	1.15 (62°C)	NR	NR
[C_8mim][Cl]	275.24	1.15 (62°C)	-82 (g->L)	NR
[C_{12}mim][BF_4]	338.24	1.02 (46°C)	26 (C->S_A) 39 (S_A->L)	NR
[C_{12}mim][PF_6]	396.40	1.13 (51°C)	60 (C->L)	NR

- NR- indicates properties not reported in literature

4.3 EXPERIMENTAL METHOD

The methods for the preparations of the ILs have been reported in the literature [41,44,64,65]. The ILs were obtained from Prof. K.R. Seddon, Queen's University, Belfast, Northern Ireland, and were used as received. In order to conserve the supply of ILs, a Teflon insert was placed within the sample reservoir, effectively reducing

the sample volume to 5 mL. This insert was constructed such that its dimensions allowed for the utilization of the rotating wheel assembly.

The preparation and operation of the spectrometer for data acquisition were carried out as discussed in Chapter 3. Liquid samples were transferred to the sample cell and thoroughly degassed in the spectrometer for ~12 hours. For hygroscopic samples, sample temperatures were maintained at 65°C during this period. DR data were obtained at room temperatures except for the case of $[C_{12}mim][BF_4]$ (m.p. ~40°C) and $[C_{12}mim][PF_6]$ (m.p. ~50°C) for which the data were taken at ~60°C. DR spectra were recorded using high-purity Ar (Matheson), and ultra-high-purity Ne (Matheson). The incident energies were 2.0 keV (Ne^+) and 2.5 keV (Ar^+), with angle of incidence from 8° to 36°. True spectral intensities were established using PeakFit™ as described in Chapter 3. The atomic ratios were calculated using Equation 3.5.

4.4 RESULTS

4.4.1 DRS spectra using 2.0-keV Ne^+

Figure 4.1 shows an example composite of the spectra obtained from $[C_{12}mim][PF_6]$ with 2.0-keV Ne^+ over the range of incidence angles a = 8° to 36°. In order to separate the spectra, scalar quantities were added to all but the 36° scan. Composite spectra for the other seven ILs taken from both Ne^+ and Ar^+ can be found in Appendix B.

The spectral features were compared to the predicted TOFs, presented in Table 4.2, calculated from Equations 2.1 (DR) and 2.3 (SS). The spectra in Figure 4.1 clearly exhibit a peak near a flight time of 5.8 μs, which is attributed to hydrogen recoils. Two other features observed are from carbon (~8.8 μs) recoils, and fluorine (~10.8 μs) recoils that are better resolved at higher angles of incidence. The C and F

peaks observed in the Ne^+ spectra are better separated than spectra taken with Ar^+. In addition, because of the closeness of the atomic masses of Ne and F, we can also expect contributions to the spectra by single scattering of Ne^+ from F (~11.4 μs). Such a signal complicates the spectral analysis because the SS and DR cross sections are similar (1.04 $Å^2$ and 0.948 $Å^2$, respectively). However, we will not differentiate between the SS and DR and lump all the events involving F as recoils.

Table 4.2 Predicted TOFs for 2.00-keV Ne^+ events

Atom (event)	Predicted TOF (μs)	Atom (event)	Predicted TOF (μs)
H (DR)	5.83	P (DR)	14.08
C (DR)	8.85	P (SS)	9.61
N (DR)	9.39	Cl (DR)	15.33
F (DR)	10.78	Cl (SS)	9.31
F (SS)	11.36	Br (DR)	24.59
		Br (SS)	8.41

We expect nitrogen recoils to occur at 9.39 μs. This is too close to completely resolve from the C(DR) signal, but examination of the spectra in Figure 4.1 reveals the C(DR) signal stands out cleanly, whereas the region in which the N(DR) signal occurs fills in substantially at higher α. Also, signals due to phosphorous recoils and Ne^+/P SS are not observed. The multiple scattering (MS) hump at long TOF is not very obvious in the Ne^+ spectra.

Normalized spectra for the complete series of ILs taken with 2.0-keV Ne^+ at $\alpha = 16^\circ$ is illustrated in Figure 4.2. The spectra demonstrate similar recoil features for each of the eight ILs. We also see definite changes in the relative experimental

intensities. For example, the fluorinated ILs, $[C_4mim][PF_6]$ has the highest F/H intensity ratios and $[C_{12}mim][PF_6]$ has the lowest. This is consistent with the change in the stochiometric atomic ratio with increasing cation size.

4.4.2 DR spectra using 2.5-keV Ar^+

Figure 4.3 shows normalized 2.5-keV Ar^+ spectra taken at $\alpha = 16^o$ for the eight ILs. Again the H(DR) and C(DR) signals are close to the predicted values (see Table 4.3). The F(DR) signal (~10.3 μs) presents itself as a more definite shoulder for the ILs containing the most fluorine. The nitrogen recoil would be between the C and DR signals, but is again unresolved for the Ar^+ data set. Under the experimental conditions in which the spectra were obtained, we would expect a peak from the single scattering of Ar^+ from P, but this is not visible. Also for several IL spectra, the broad feature centered at 14.8 μs is due to multiple scattering.

Table 4.3 Predicted TOFs for 2.50-keV Ar^+ events

Atom (event)	Predicted TOF (μs)	Atom (event)	Predicted TOF (μs)
H (DR)	7.16	P (DR)	12.40
C (DR)	9.08	P (SS)	17.13
N (DR)	9.43	Cl (DR)	13.19
F (DR)	10.31	Cl (SS)	15.00
F (SS)	-	Br (DR)	20.95
		Br (SS)	8.41

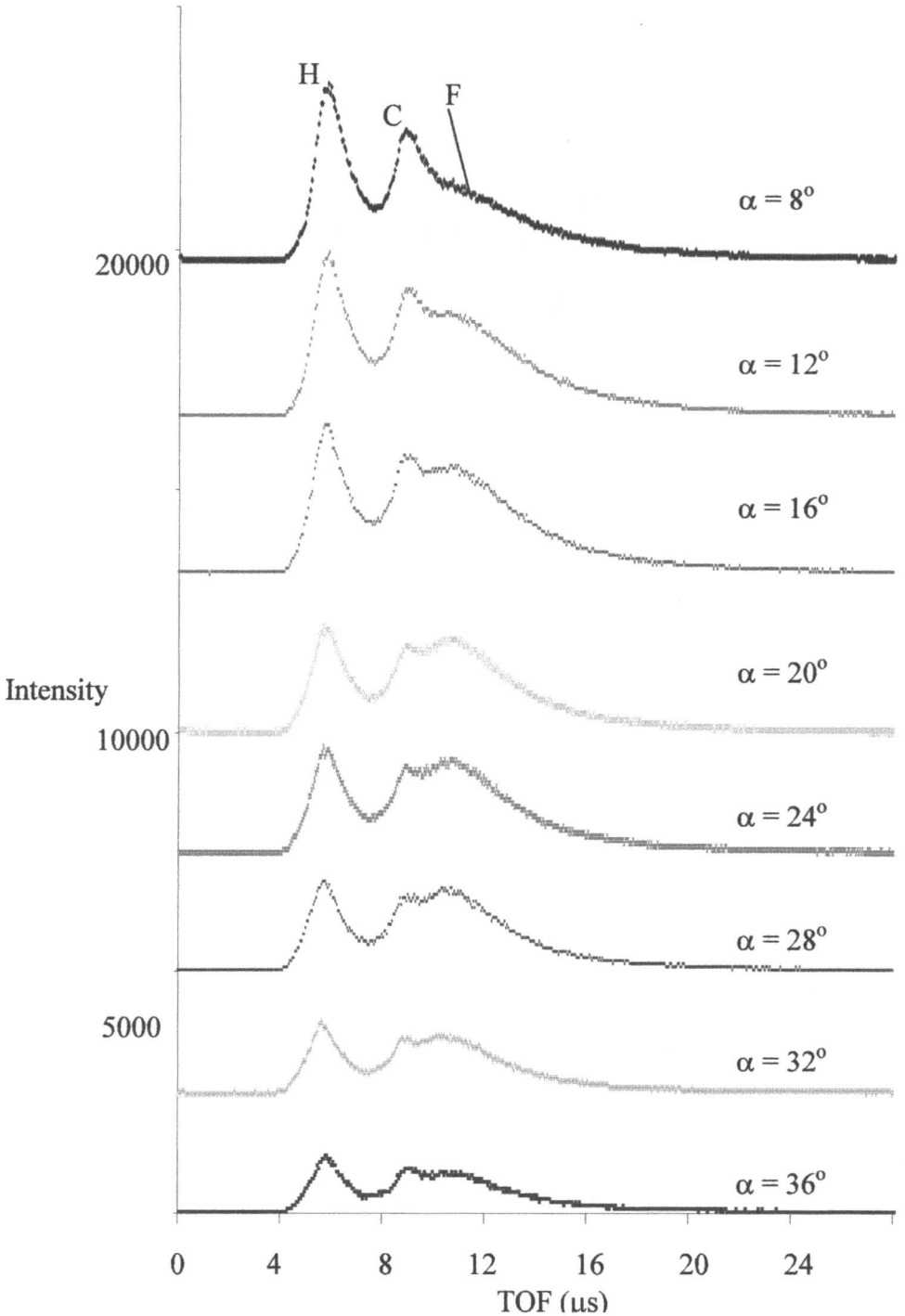

Figure 4.1 Composite DR spectra obtained from $[C_{12}mim][PF_6]$ using 2.0-keV Ne^+

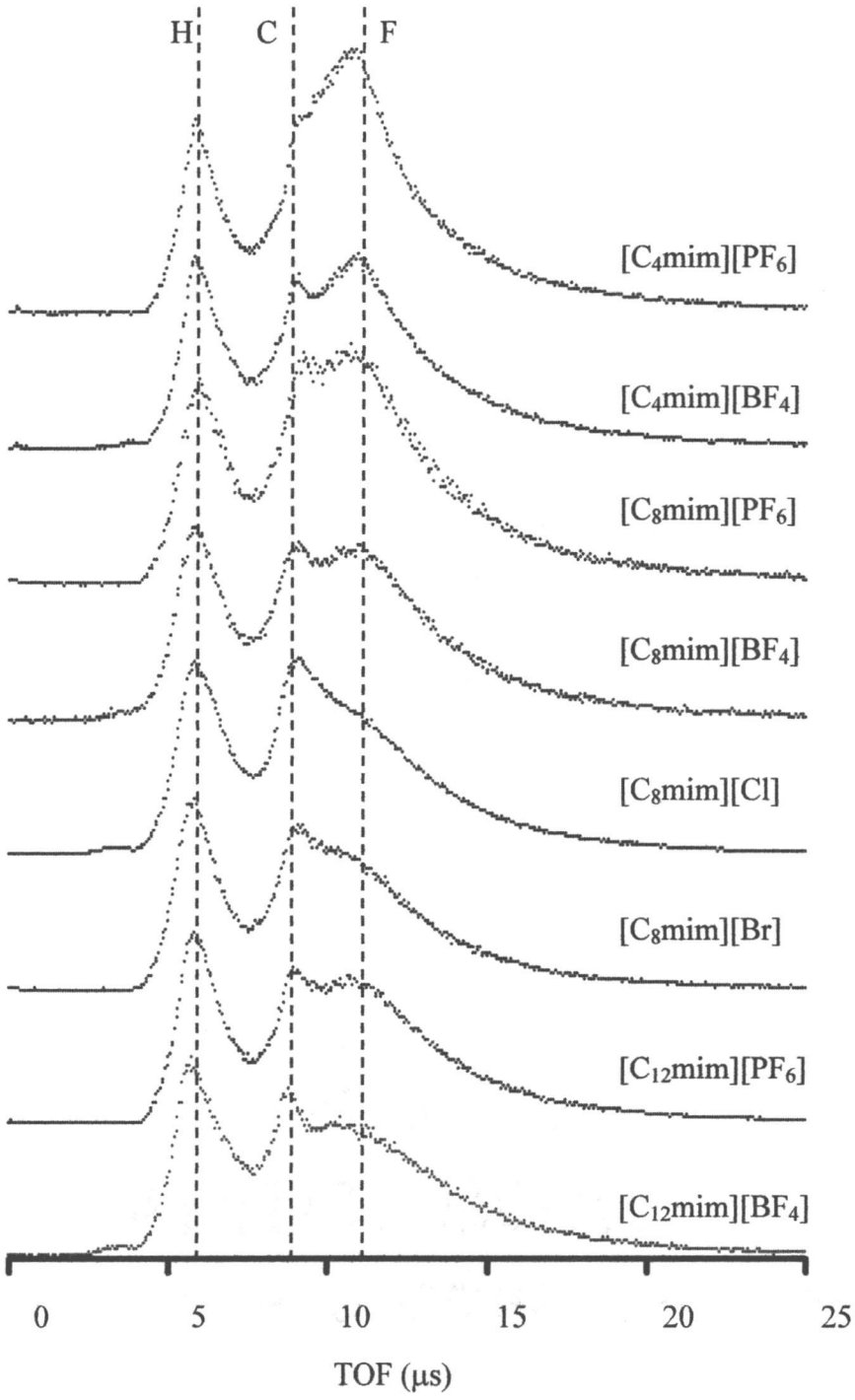

Figure 4.2 DR spectra of ionic liquids taken with 2.00-keV Ne^+ at $\alpha = 16^o$

4.4.3 Surface atomic ratios

Figure 4.4 shows an example of a spectrum deconvoluted with PeakFit™. Each spectrum contained H, C, F (and possibly N) recoil features plus a long TOF MS feature. In some spectra features due to hydrogen surface recoil are visible. Such small features were added to the fit where most necessary. The fits were carried out as previously described (in Chapter 3) using exponentially modified Gaussian functions. The species C, N, and F are very close in the periodic table and have similar scattering and recoiling cross sections. Therefore, we made the reasonable assumption that the width and symmetry parameters in the Gaussian functions for these peaks share the same values. In order to further simplify the fit process, the parameters for the MS contribution to the tail were established from the spectra from liquids with simple halide anions (Cl^- and Br^-). In such spectra, a strong halogen signal is not present, and therefore the tail structure is dominated by the MS contribution, allowing it to be clearly separated and its parameter established. These parameters for the MS peaks were then used to fit the fluorinated IL spectra. This additional step allowed for a more consistent fit from spectrum to spectrum, and produced acceptable standard errors in the parameter values. The errors in the true spectral intensities were calculated by standard error propagation methods from the parameterized EMGs.

There are problems in the deconvolution of the spectra obtained with both projectiles. In the case with Ar^+ spectra, we would expect more useful information regarding F atoms, since no Ar^+/F single scattering occurs at the experimental scattering angle. However, there was greater difficulty in fitting the Ar^+ data set due to the poorer resolution between C(DR) and F(DR) signals and the more complex tail structure. This was reflected in the high error associated with the fitted parameters for these data.

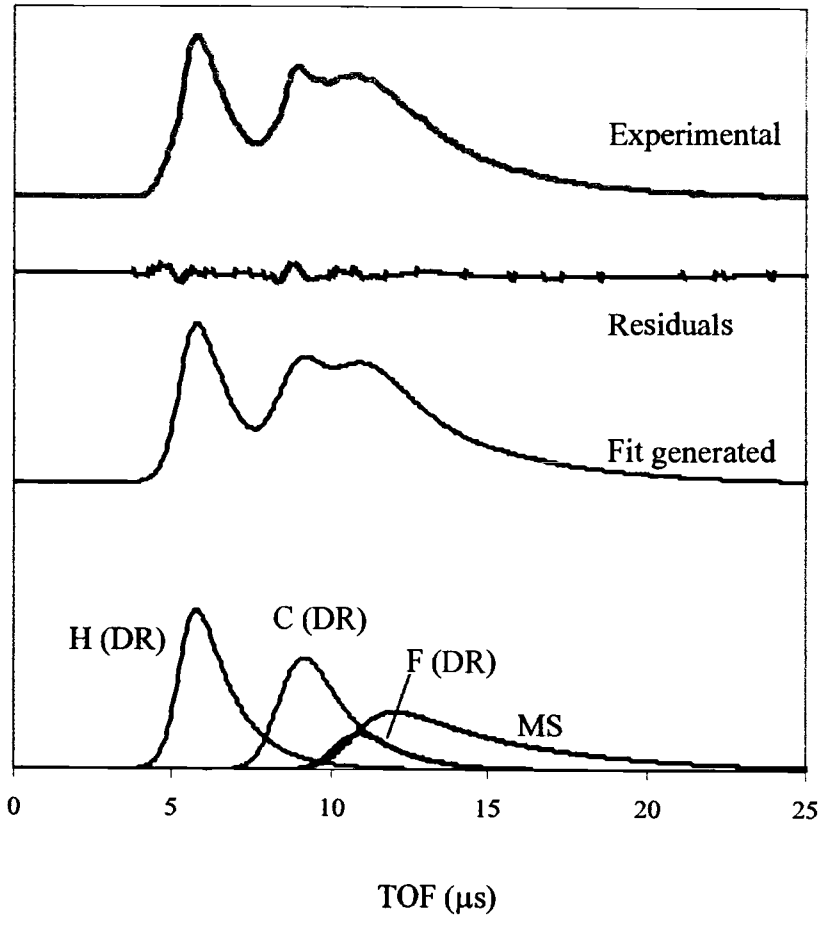

Figure 4.3 Deconvolution of peaks for $[C_{12}mim][PF_6]$:2.0-keV Ne^+, $\alpha = 16^o$

The neon data are appropriate for determining H/C atomic ratios due to the greater separation between the H(DR) and C(DR) peaks. The errors resulting from this dataset are more modest and we relied predominately upon these data for the analysis. Furthermore, the lighter Ne^+ projectile penetrates deeper than the slower and lighter Ar^+. This results in more variation of the spectra with the angle of incidence that, in turn, yields more information. While the Ne-F collision events combine to produce an indeterminable amount of F(DR) and Ne(SS) signals, both

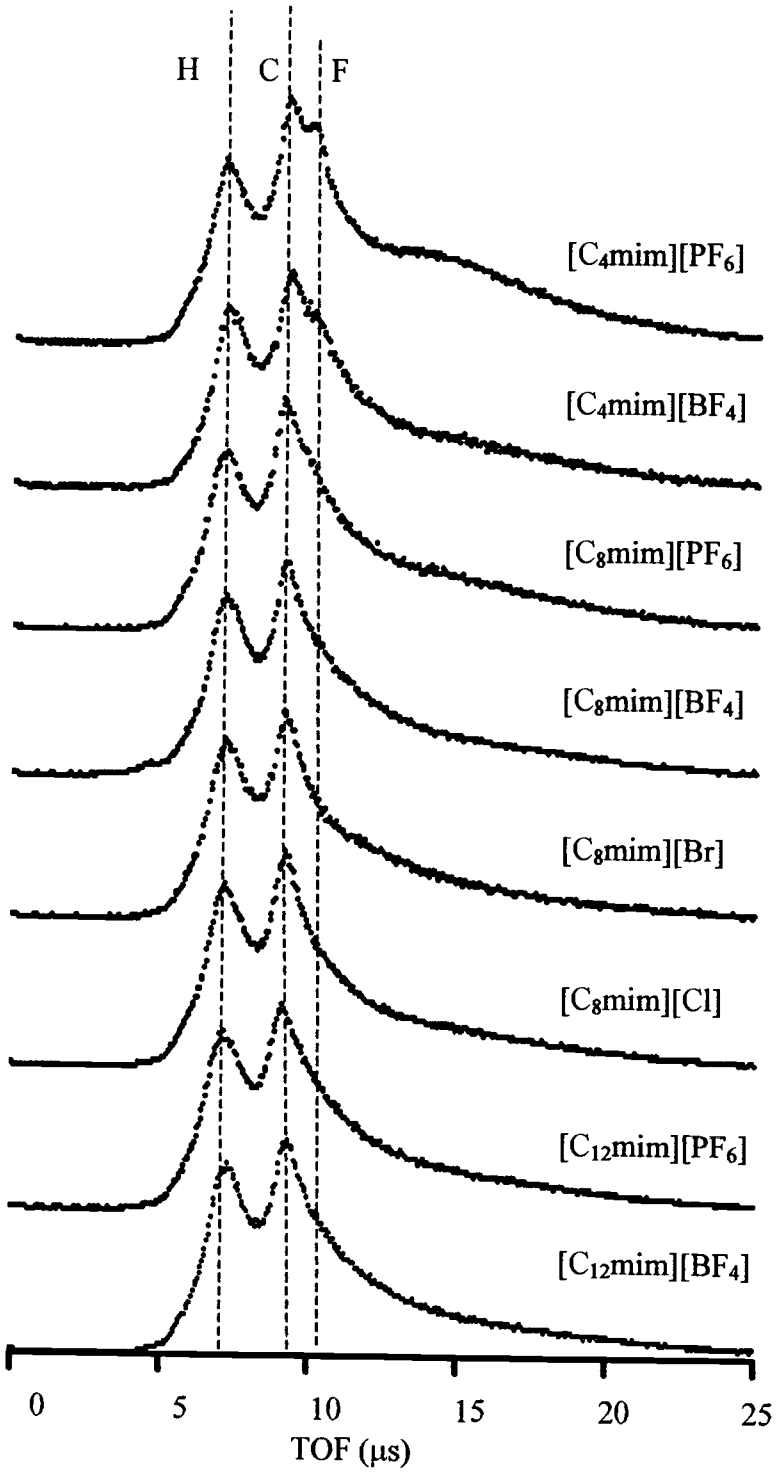

Figure 4.4 DR spectra of ionic liquids taken with 2.50 keV Ar^+ at $\alpha = 16^o$

event peaks are close enough to combine them together in the fit process as the recoil peak. Yet as the example of the fit shown in Figure 4.4 illustrates, the resolution between the F(DR) and MS peak is poor, and may produce uncertainties in using the F(DR) for analysis. However, the use the F/C ratios from Ne^+ data sets will be justified later on in the discussion.

The atomic ratios for the Ne^+ data set, which are more useful, are shown in Figure 4.5 (H/C ratios) for [C_8mim][Cl] and [C_8mim][Br]. The atomic ratios for the fluorine- containing ILs are shown in Figure 4.6 (H/C) and in Figure 4.7 (F/C).

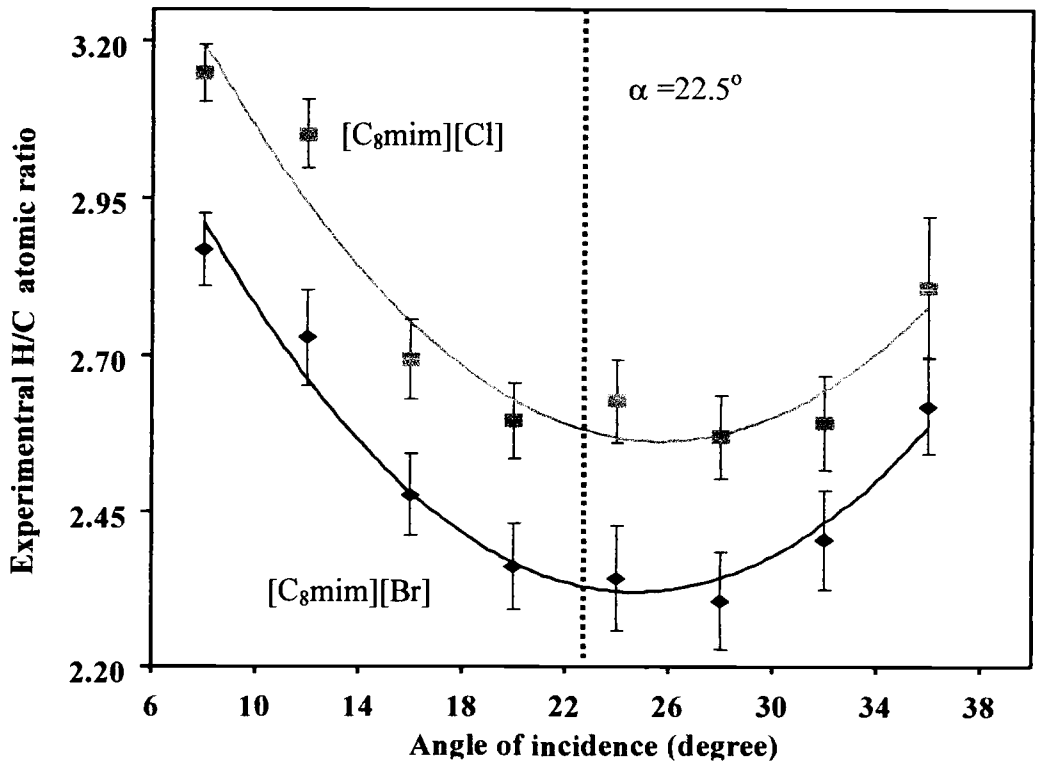

Figure 4.5 Experimental H/C ratios for [C_8mim][Cl] and [C_8mim][Br] from 2.0-keV Ne^+

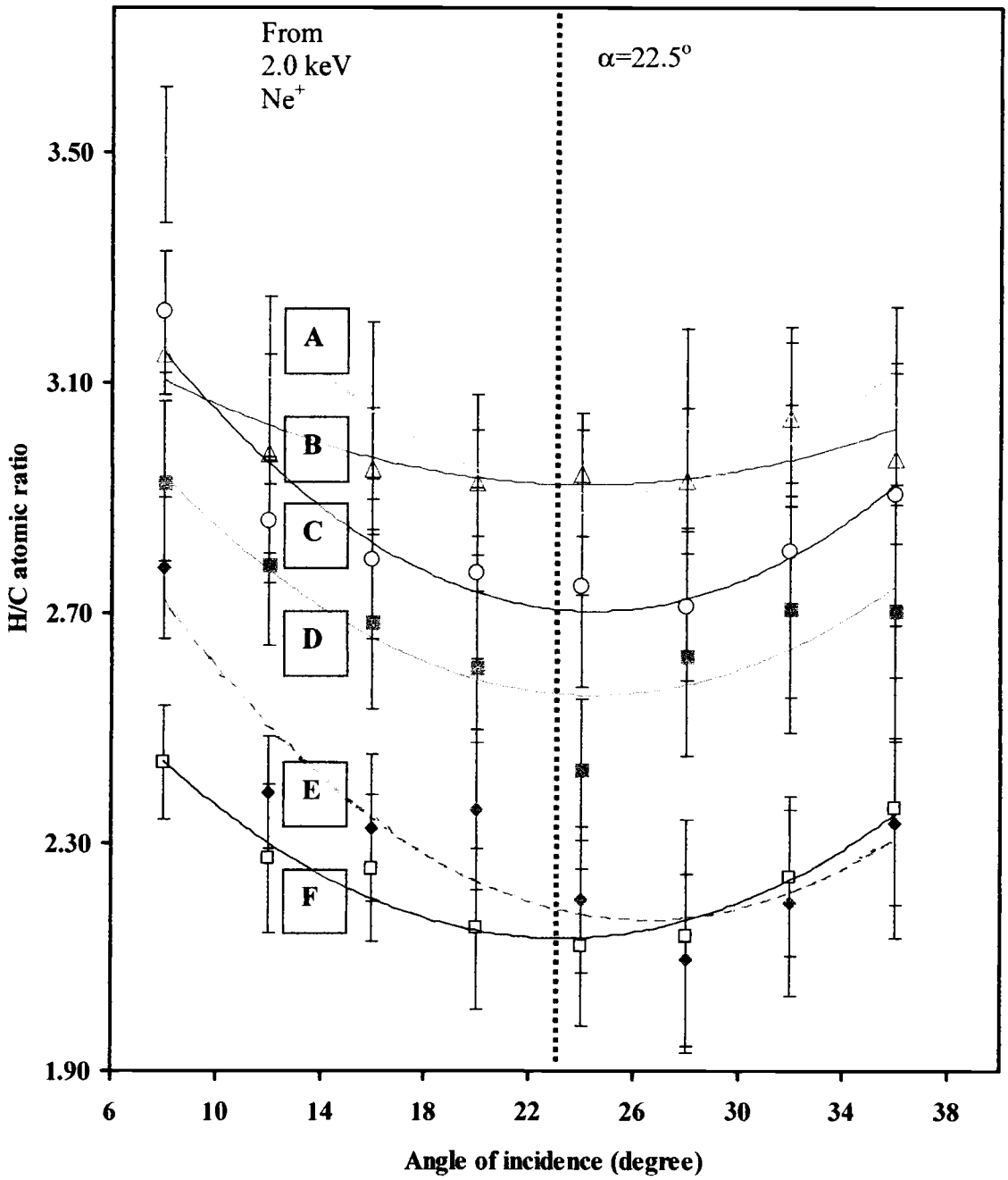

Figure 4.6 Experimental H/C atomic ratios from 2.0keV Ne^+: A) $[C_{12}mim][BF_4]$, B) $[C_{12}mim][PF_6]$, C) $[C_4mim][BF_4]$, D) $[C_8mim][BF_4]$, E) $[C_4mim][PF_6]$, and F) $[C_8mim][PF_6]$

4.5 DISCUSSION

4.5.1 Influence of incident angle (α) on atomic ratios

Much of the discussion concerning the surface composition and orientation of the ILs relies on the H/C and F/C ratios derived from the Ne^+ spectra. For the H/C ratios in Figure 4.5 and 4.6, a minimum value is observed between incident angles of 22° to 26°. The F/C ratio in Figure 4.7 shows a maximum between the same ranges. In general the surface penetration is at a maximum when α and β are of the same magnitude ($\alpha = \beta = \phi/2 = 22.5°$). This occurs because at low (glancing) or high incident angles the depth of from which the recoils originate are limited by either the effects of shadowing in the entrance channel (low α) or by blocking in the exit channel (high α). At $\alpha = 22.5°$ a compromise is reached between shadowing and blocking effects. Simulations from this laboratory have indicated that at $\alpha = 22.5°$, while a majority of the recoils originate from the top 2-4 Å, some can be generated from up to 10 Å below the surface [33]. An angle of incidence of 16° was shown to best represent a sampling depth of 2-4Å.

4.5.2 Structural considerations and line-of-sight (LOS) simulations

An important aspect of the analysis is the comparison of the experimental data with those predicted by the LOS simulations (described in Chapter 3). In order to simplify the construction of the molecular models with Hyperchem™, several considerations were made concerning the IL molecular structure in the liquid state. Assumptions were made concerning the location of the anion with respect to the cation, and the orientation of the 3-alkyl chain with respect to the imidazolium ring.

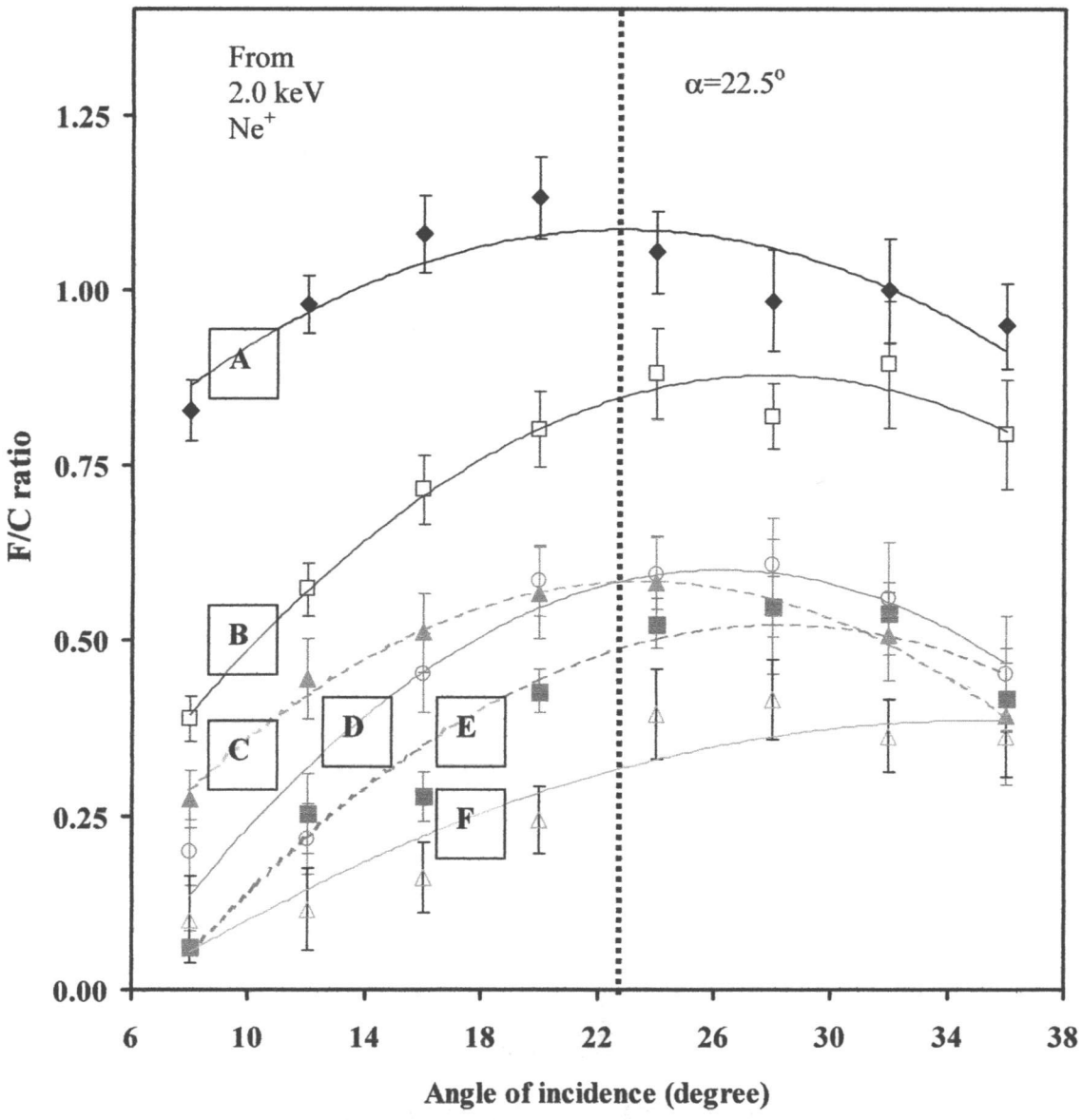

Figure 4.7 Experimental F/C atomic ratios from 2.0-keV Ne^+: A) $[C_4mim][PF_6]$, B) $[C_4mim][BF_4]$, C) $[C_8mim][PF_6]$, D) $[C_8mim][BF_4]$, E) $[C_{12}mim][PF_6]$, and F) $[C_{12}mim][BF_4]$

For the arrangement of the anion with respect to the cation, we can look to crystallographic investigations of $[C_2mim][PF_6]$ [66] and $[C_{12}mim][PF_6]$ [62] for guidance. Due to the difference in the length of the 1-alkyl chain in these two cases, variation in the crystal packing is observed. Yet, they share a similar structural feature in that the $[PF_6]^-$ anion is located above the C(2) carbon atom (see Figure 4.8)

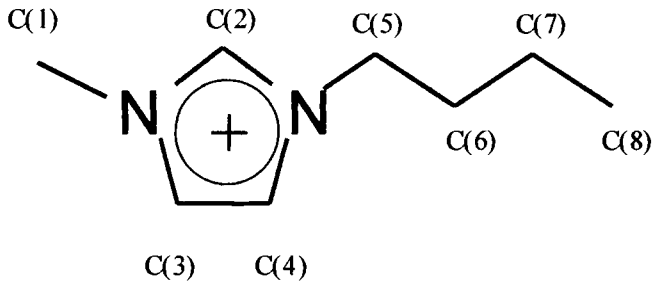

Figure 4.8 Structure of IL cation (n = 4)

of the heterocyclic ring, with a typical cation-anion separation (~3 Å) close to the Van der Waals distance. These separations are consistent with non-hydrogen bonded, simple Coulombic interactions between the ions. To the extent we can extrapolate such solid-state structures to the liquid salts, we can suppose that such interactions would lead the anions to remain centrally located over the N-end of the ring with a Van der Waals separation close to that in the solid state. This is justified by the smallness of the typical 3-4 % increase in the mean intermolecular separation going from the solid state to the liquid state observed for many molecular systems [67].

Now we must consider the alignment of the 3-alkyl chain with respect to the heterocyclic ring. Crystallographic data for $[C_{12}mim][PF_6]$ [62] indicated that the 3-alkyl chain is non-linear due to a gauche defect introduced by rotation of the C(7)-C(8) bond. In the liquid state, the alkyl chain is flexible and any of the C-C bonds

can rotate between the gauche and anti conformation. Furthermore, steric interactions with the anion restrict the complete folding of the chain. Assuming that interactions with neighboring molecules do not hinder C-C bond rotations, it is reasonable that an average chain conformation results in partial extension.

4.5.3 Cation/Anion surface composition

For ILs, the surface composition is dependent on the arrangement of the species at the surface. Some possible arrangements for the ILs are shown in Figure 4.9. An extreme case is that the surface is completely dominated by one ion or the other. Also if the ILs are likely to be associated in ion pairs, the surface can be composed of an equimixture of both ions, with the cation ring arranged parallel or perpendicular to the surface plane.

As shown in Figures 4.2 and 4.3, the spectra for $[C_n mim][BF_4]$ and $[C_n mim][PF_6]$ ILs shows the presence of recoiled species from both the cation (H, and C) and the anion (F). This probably is an indication that both ions are present at the surface. Therefore a high degree of surface enrichment by either the anion or the cation is improbable.

The molecular models of the cations were constructed and optimized following the previously mentioned assumptions. In order to account for molecular tumbling, the anion was centrally placed next to the heterocyclic ring such that for the anion-dominated surface, three F atoms (for PF_6^-) or two F atoms (for BF_4^-) would be fully exposed on the surface plane. LOS was then allowed to estimate the average numbers of each type of atoms accessible to the ion beam at $\alpha = 16^\circ$ over a 360° azimuthal angle.

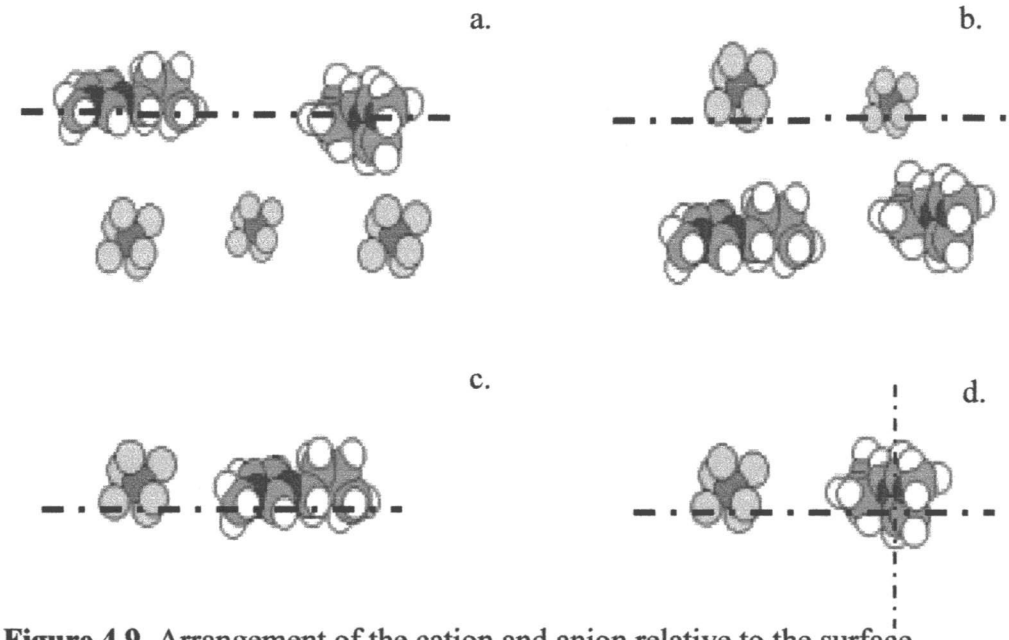

Figure 4.9 Arrangement of the cation and anion relative to the surface plane: a) cation dominated surface, b) anion dominated surface, c) cation-anion sharing of the surface with parallel cation ring, and d) cation-anion sharing of the surface with ring perpendicular

The simulations showed that with the anion-dominated surface, the fluorinated-anion layer shadows the underlying carbon-containing cations from the incident ions. The estimated F/C ratio was infinity, regardless of the cation size, indicating that the mean distance of underlying counter-ions from the top layer was greater than the 2-4 Å sampling depth. Whereas, for a cation-enriched surface the estimated number of recoiled F atoms was 0 for all fluorine-containing ILs. However, as inferred from the experimental data ($\alpha = 16^{o}$), the F/C varies between ~ 0.2 ($[C_{12}mim][BF_4]$) to ~1.1 ($[C_4mim][PF_6]$). This is indicative that both ions populate the surface. As we shall see in the discussion of the cation orientation, we can further narrow down the arrangement from the perpendicular or parallel cation models.

The qualitative analysis of $[C_8mim][Cl]$ and $[C_8mim][Br]$ is complicated by the lack of halide DR signals. It could be hypothesized that the surface is cation

enriched. However, even if the surface is shared equally between the cations and anions, there are two factors that would lead to the lack of a halide signal. First, the simple halides are small in size when compared to the $[PF_6]^-$ and $[BF_4]^-$ anions and would lead to them being shadowed by a neighboring cation. Furthermore, there is only one atom per anion and therefore will further reduce the relative size of the Cl(DR) or Br(DR) signal. As a result, we cannot provide a definitive answer concerning the surface composition of $[C_8mim][Cl]$ and $[C_8mim][Br]$ with the available data.

4.5.4 Cation surface orientation

Due to the symmetry of the anions used here, their orientations are not an issue in the following discussion. What is more important is whether the cation adopts some preferential average orientation of the cation at the surface or whether all orientational order is lost due to molecular tumbling. However, if molecular motions randomly distributed the ion pairs, little or no change would be observed in the spectra of the ILs with sampling depth (change in α). Such a change is not observed and it is highly likely that some degree of preferred orientation of the cation occurs at the surface. The two extreme cases of such an orientation are with the ring, on the average, parallel or perpendicular to the surface (shown in Figure 4.9).

4.5.4.1 Fluorine-containing ionic liquids

In the case where the heterocyclic ring is parallel to the surface, the 1-methyl substituent as well as a good portion of the 3-alkyl chain will lie at the surface. If we assume that the 3-alkyl group is fully extended, then almost all the carbons will be exposed at the surface. The number of C and F atoms per fluorine-containing IL unit that are exposed to the incident ions can be estimated. For the anions, the octahedral

PF_6^- will expose close to three F atoms, and the tetrahedral BF_4^- will expose close to two. However, such numbers may be lower due to the cation shadowing effects.

With the parallel orientation, the estimated F/C atomic ratio at maximum ion penetration (α ~22.5°) would be about 0.4 for [C_4mim][PF_6], and would decrease to ~0.2 for the other ILs in the homologous series. Taking shadowing effects into consideration, the F/C ratios would decrease from such estimates. However, as shown in Figure 4.7, the experimental F/C ratios at 22.5°, range from ~1.0 for [C_4mim][PF_6] to ~0.35 for [C_{12}mim][BF_4]. Furthermore, if the ring were parallel, most of the molecule's atoms would be at the surface. Increasing the sampling depth would not change the number of H and C atoms exposed per molecule to the incident ions. The H/C ratios would not change significantly with the sampling depth. Examination of the experimental H/C ratios in Figure 4.4 indicates a 10-15% change with α. We can then draw a conclusion that the ring parallel orientation is not likely, based on the deviation of the estimated F/C ratios to the experimental values, and the significant change of the H/C ratios with α.

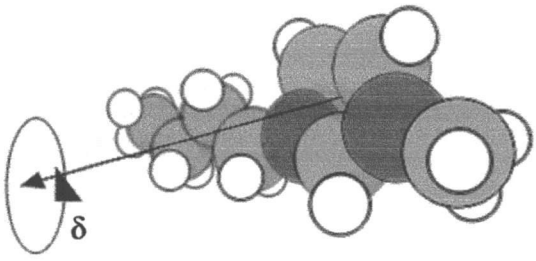

Figure 4.10 Axis of rotation of the cation defining δ: as shown δ is 180°

In the case of a ring that is perpendicular to the surface, the average cation

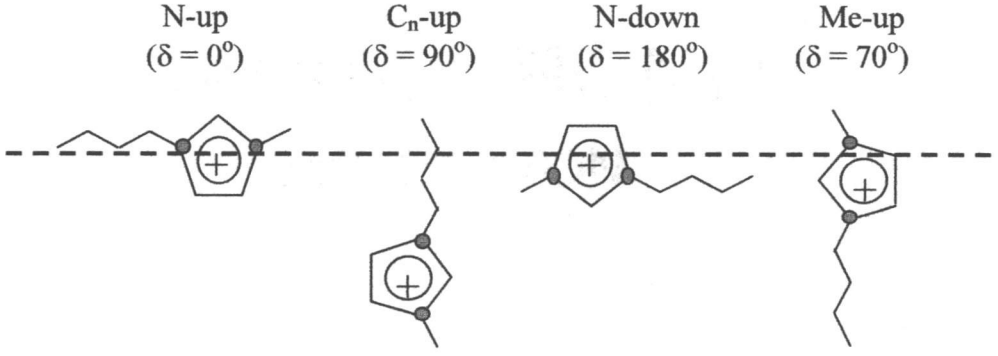

Figure 4.11 Surface orientations of the cation based on the rotational angle (δ)

orientation is dependent on δ that is defined by the axis that passes through the ring center (Figure 4.10). As illustrated in Figure 4.11, we have arbitrarily set values of angles with certain "reference" orientations as: nitrogen up (N-up) $\delta = 0^{o}$, 3-alkyl center (Figure 4.10). As illustrated in Figure 4.11, we have arbitrarily set values of angles with certain "reference" orientations as: nitrogen up (N-up) $\delta = 0^{o}$, 3-alkyl chain up (C_n-up) $\delta = 90^{o}$, nitrogen down (N-down) $\delta = 180^{o}$, and 1-methyl group up (Me-up) $\delta = 270^{o}$. Depending on δ, the numbers of atoms of any type accessible to the incident particles would change. For example, with the anion located close to the nitrogens, the H/C and F/C atomic ratios would be different when comparing a N-down orientation [i.e. C(3) and C(4) upwards] with that when the nitrogens are positioned on the plane. In addition, the orientation of the alkyl chains with respect to the surface plane would also change with the average rotational angle.

We shall discuss the probable ring orientation by first examining the C_n-up orientation. At $\delta = 90^{o}$, the surface environment would be similar to alkanes, with both CH_3- groups and a number of $-CH_2$- groups at the surface [68]. But in this orientation, the imidazolium ring and the closely associated anion would be expected to be positioned below the 2 Å ion-probing depth. If the cation, for a particular fluorine-containing IL, adopted this arrangement, F (DR) signals would not be observed and the F/C ratios would be zero at the glancing angles of incidence. The scans for all the $[BF_4]^-$ and $[PF_6]^-$ ILs show fluorine recoils, and this is a clear indication that the C_n-up orientation is unlikely regardless of n.

Using the LOS simulations, we related the experimental H/C or F/C atomic ratios to the N-up, N-down, or Me-up cation orientations. An optimized cation was positioned in the vertical plane such that the nitrogens were symmetrically uppermost (N-up, $\delta = 0^{o}$). The ion pairs were then rotated counterclockwise about the rotational axis in 30° increments to produce the orientations previously mention.

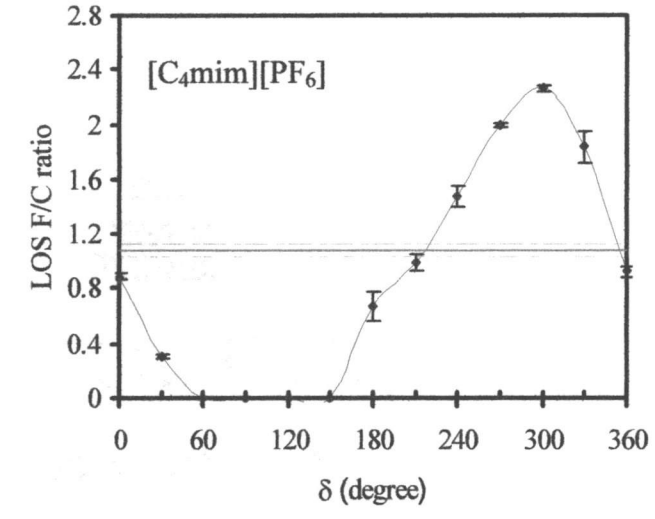

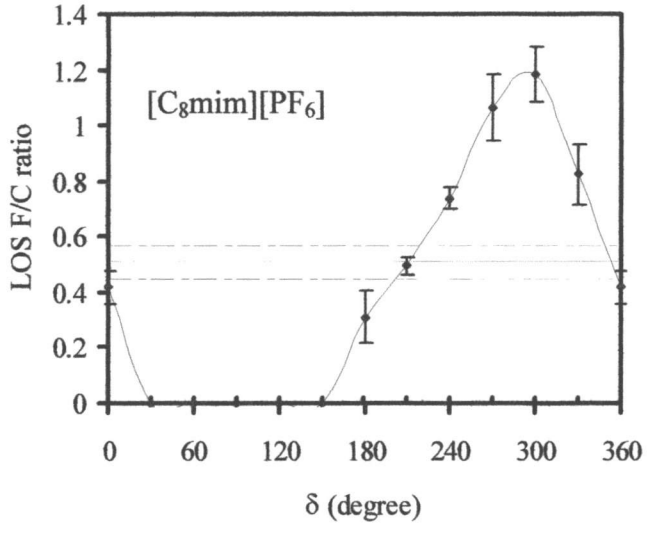

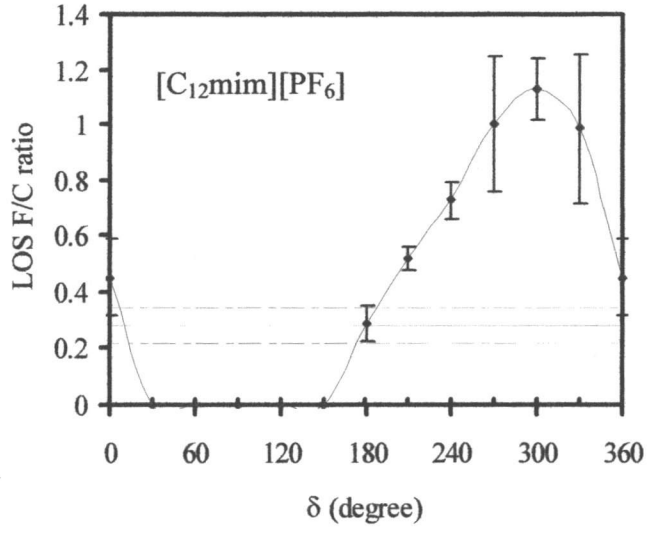

Figure 4.12
Estimated F/C ratios for $[C_nmim][PF_6]$ ILs from LOS simulations at α = 16°. The solid lines indicates the atomic ratios calculated from experimental data (α=16°), and the dashed lines indicates the calculated

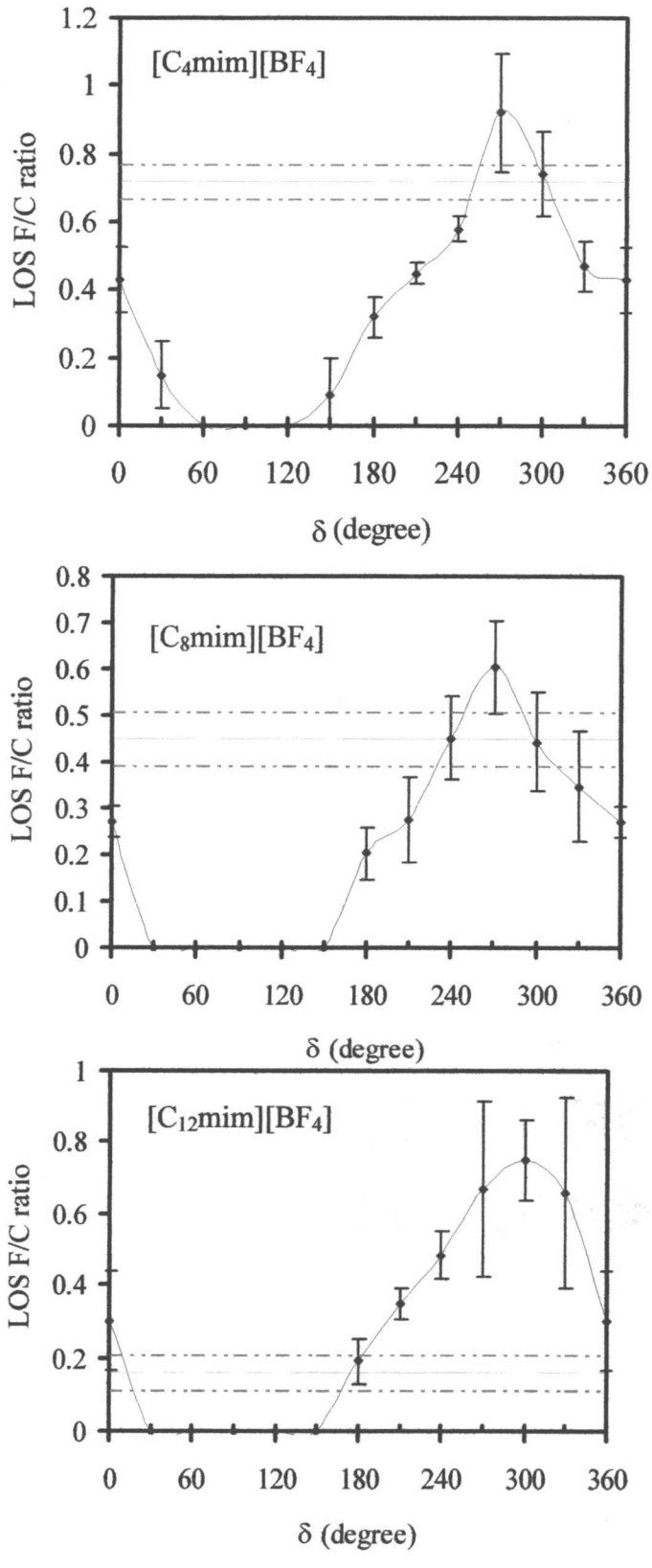

Figure 4.13
Estimated F/C ratios for $[C_nmim][BF_4]$ ILs from LOS simulations at $\alpha=16^o$. The solid lines indicates the atomic ratios calculated from experimental data ($\alpha=16^o$), and the dashed lines indicates the calculated errors.

Instead of estimating the atomic ratios at all angles of incidence, the angle of $\alpha = 16^{o}$ was chosen for these simulations. If the cation were arranged with either N-up, N-down, and within some small rotational range of these two orientations, it would then be expected that, at higher beam incident angles (such as 22.5^{o}), molecules below the topmost molecular layer might contribute to recoil signals. At $\alpha = 16^{o}$, with the 2-4 Å sampling depth, we can attribute the recoils to the surface layer regardless of the orientation. Because LOS simulates only the surface layer, the calculated ratios at 16° can then be compared to the experimental values. By contrast, errors would be introduced into the estimations when compared with the experimental results at 22.5^{o}, which may contain recoils from below the top layer.

Figures 4.12 and 4.13 show the estimated LOS F/C ratios (at $\alpha = 16^{o}$) as a function of the angle of rotation for the cation ring (with ring vertical) for the fluorine-containing ILs. The error bars are primarily from uncertainties in estimating the mean inter-molecular distances that enter into the LOS calculations. Also included in the plots are the experimentally derived atomic ratios (solid lines) and the associated errors (dashed lines). From these plots, the estimated LOS F/C ratios support the previous argument against the C_n–up orientation. In addition, rotations of $\pm 30^{o}$ from the C_n-up position would position the anion too deep in the surface to be accessible to the ion beam and the F/C ratio will be zero at all chain lengths. Another trend in the LOS F/C ratios is the decrease in the predicted F/C ratios for the three other reference orientations (N-up, N-down, and C_n-up) with increasing 3-alkyl chain length. Regardless of the cation, molecular tumbling keeps the number of F atoms, for a particular anion, exposed to the ion beam constant. As the cation size increases, we can expect the F concentration in the top 2 Å to become progressively diluted by the C atoms.

Clearly, the experimental data support ruling out the C_n-up orientations. The F/C ratios for $[C_4mim][PF_6]$ and $[C_8mim][PF_6]$ indicate best fits near two possible rotational angles near $\delta = 0^{o}$ and 210°. Substituting these ILs with the BF_4^- anion

brought the cation closer to the Me-up orientation. For the C12 homologue, the F/C data indicated that the ring adopted both a N-up and N-down orientation. However, as mentioned in the results section, the overlap in the F(DR) and MS peak inherent uncertainties in the calculated experimental F/C ratios. This makes it problematical to determine the actual orientation from this data alone. But these values can be used to eliminate certain ring orientation.

More details on the cation orientation can be attained by consideration of the H/C ratios. Figures 4.14 and 4.15 illustrate the estimated LOS H/C ratios (at $\alpha = 16^{o}$) as a function of the angle of rotation for the cation ring (with ring vertical) for the fluorine- containing ILs and its relationship to the experimental values. Again, the solid lines indicate the experimental H/C ratio, with the dashed lines illustrating the errors in these values. Rotation about the ring axis tends to produce calculated H/C ratios that fall between 1.7 and 2.9.

At $\delta = 0^{o}$ (N-up), the LOS H/C ratios are less than 2 for all ILs regardless of the identity of the cation and anion. The compounds that contain $[C_4mim]^+$ ion appear to show higher H/C ratios than $[C_8mim]^+$-containing compounds, but both $[C_{12}mim][PF_6]$ and $[C_{12}mim][BF_4]$ have higher ratios than the shorter-chain analogs. Otherwise, there appears to be little effect in exchanging one anion for another. At such an N-up orientation, the majority of the recoils is attributed to the alkyl chain. The anion, located near the ring, plays little role in the shadowing and blocking of the atoms in the chain. A similar effect is observed with the N-down orientation. In all cases, an increase in the H/C ratio is observed as the 3-alkyl group rotates upward from the N-up orientation, followed by a decrease in the ratio to ~2 at a rotational angle of 180°. When the molecule is tilted towards the C_n-up position, the number of methylene groups exposed to the ion beam decreases. The carbons in atoms in the deeper methylene groups are more effectively blocked by the higher carbon atoms than the hydrogen atoms are. As expected the H/C ratios are at a maximum near $\delta = 270^{o}$.

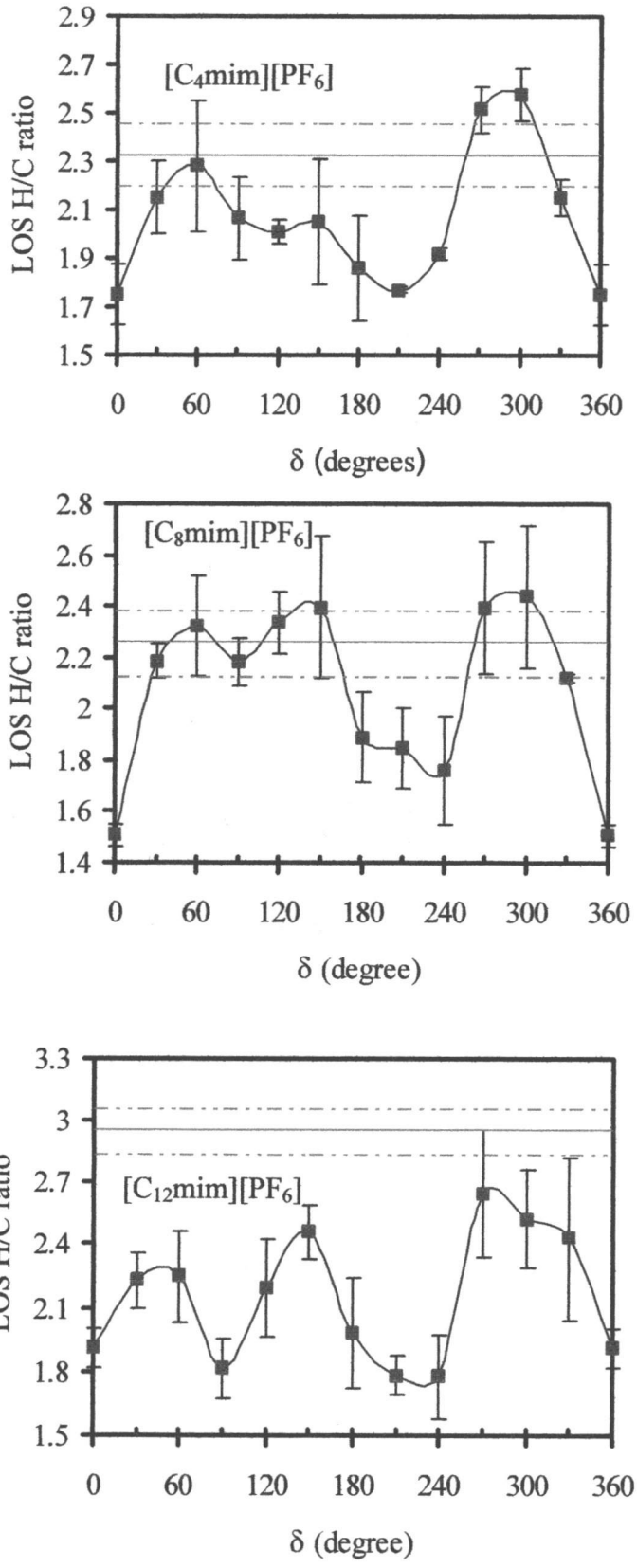

Figure 4.14
Estimated H/C ratios for $[C_nmim][PF_6]$ ILs from LOS simulations at $\alpha = 16^o$. The solid lines indicates the atomic ratios calculated from experimental data ($\alpha = 16^o$), and the dashed lines indicates the calculated errors.

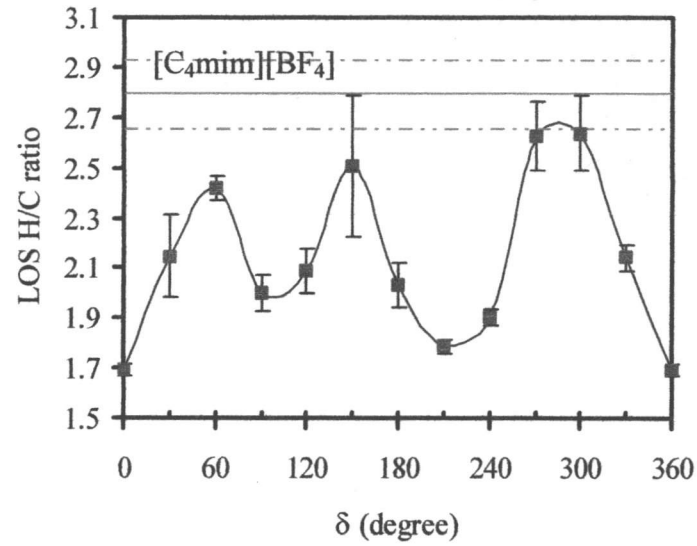

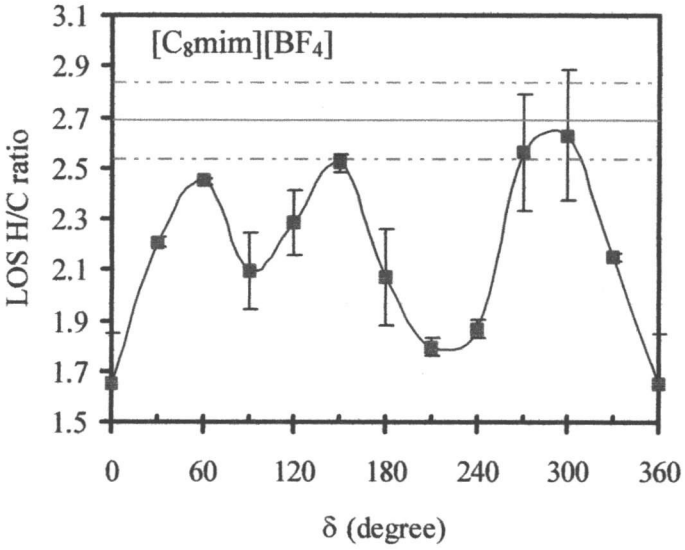

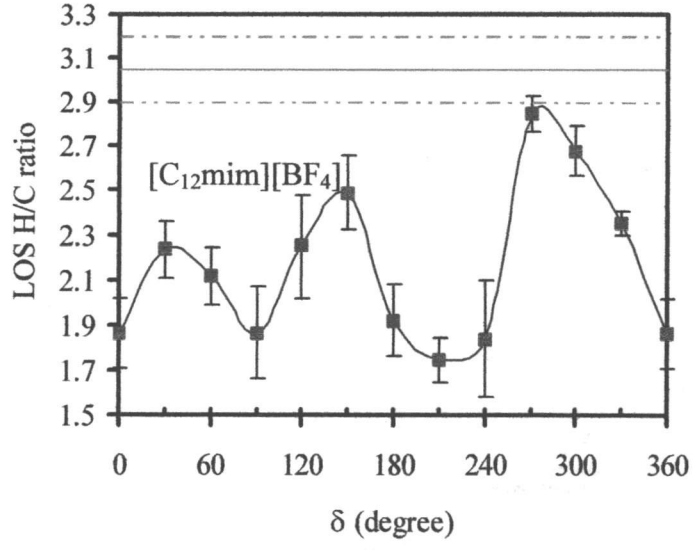

Figure 4.15
Estimated H/C ratios for $[C_nmim][BF_4]$ ILs from LOS simulations at $\alpha=16^{o}$. The solid lines indicates the atomic ratios calculated from experimental data ($\alpha=16^{o}$),and the dashed lines indicates the calculated errors.

With the 1-methyl group at the surface, those liquids with a hexafluorophosphate counterion show lower predicted H/C ratios than do those with a tetraflurophosphate anion. The origin of this trend is due to the effect of shadowing and blocking of the ring atoms. The hydrogen atoms in the imidazolium ring are effectively shadowed by the larger anion making them less accessible to the ion beam. The ring carbons are also shadowed, but those that are exposed to the ion beam encounter intramolecular blocking (i.e. by both the methyl group and the anion). Whereas, with both types of anion intramolecular blocking of the hydrogen is less effective. These series of events tends to increase the H/C ratio when the anion size is decreased.

As Figure 4.13 indicates for the 1-butyl and 1-octyl ILs, the experimental H/C ratios overlap with the LOS values at several rotational angles. Earlier we had shown that the F/C atomic ratios of all species effectively rule out C_n-up orientations close to $\delta = 90^\circ$. With this in mind, we see that for all the ILs the best areas of agreement in the H/C data are consistent with orientations near Me-up ($\delta = 270^\circ$). For both n = 4 and 8 hexaflurophosphates, the data indicate two average orientations at 260° and 320°. Both of which expose more of the heterocyclic ring to the surface. The data for n = 4 and 8 tetrafluroborate suggest similar orientations near 290°. With both $[C_{12}mim][PF_6]$ and $[C_{12}mim][BF_4]$, the experimental data overlap with LOS values at 270°, where the 1-methyl group is fully exposed at the surface. It is apparent that the length of the 1-alkyl chain plays little role in changing the cation surface orientation for the n = 4 and 8 ionic liquids. But the orientation is effected by increasing the alkyl chain length to n = 12. Furthermore, changing to the smaller tetrafluoroborate anion has a similar effect of bringing the methyl group close to the surface.

4.5.4.2 [C_8mim][Cl] and [C_8mim][Br]

From the previous discussion, we were inconclusive concerning the surface composition of the chloride- and bromide-containing ionic liquids. However, we will assume that replacement of the polyatomic anion with either Cl^- or Br^- would not drastically effect the surface orientation, and that the cation ring adopts some ring vertical orientation. As with the fluorinated-anion liquids, in the cases of [C_8mim][Br] and [C_8mim][Cl], the experimental H/C atomic ratio is higher for the smaller anion. The value at $\alpha = 16^o$ for the bromide liquid is approximately 2.5 (a similar value to [C_4mim][PF_6]) and for the chloride is 2.8 (similar to [C_8mim][BF_4]). LOS calculations at $\alpha = 16^o$ were also carried out for these two ILs over the range of cation rotational angles. The results of these simulations are illustrated in Figure 4.16. Again the horizontal lines indicate the experimental values and the associated errors.

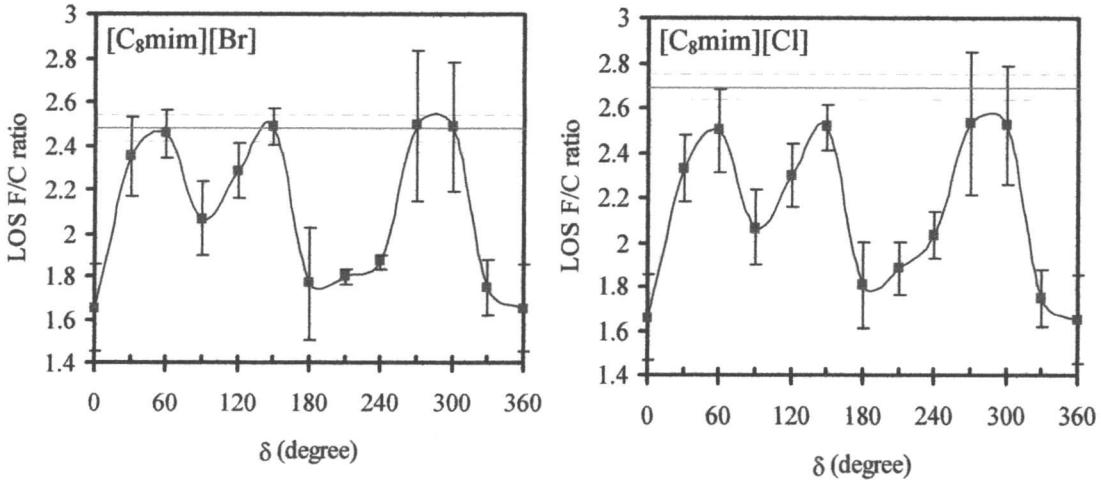

Figure 4.16 Estimated H/C ratios (α=16°) for [C_8mim][Br] and [C_8mim][Cl]

As the above figures show, both the chloride and bromide compounds exhibit similar H/C ratios over the entire rotational range. This would be expected as both anions have similar ionic radii (Br^- = 1.87Å and Cl^- = 1.67Å), and the molecular models were constructed assuming similar ring-anion separations (~3Å). As the overlap of the experimental data with the LOS values indicates more than one cation orientation. In the absence of halide signals, the experimental Br/C and Cl/C ratios are zero, and could not offer the same type of guidance as the F/C ratios of the fluorine-containing compounds. The LOS halide/carbon ratios were estimated to be zero for a majority of the ring vertical orientations. As a result, we cannot argue for or against a particular orientation suggested by the H/C data for these two ILs.

4.6 CONCLUSION

This chapter represents the first study concerning the composition and orientation of ILs containing the 1-C_nH_{2n+1}-3-methylimidazolium cation [$C_n$mim] derived from DRS. The findings include that bulk stoichiometry is conserved at the surface, i.e. neither type of ion is enriched at the surface, for those ILs with the hexafluorophosphate and tetrafluoroborate. Furthermore, the data best fit the cation ring being perpendicular rather than horizontal to the surface. However, the experimental data for both [C_8mim][Cl] and [C_8mim][Br] did not allow for support for any one surface arrangement. But it is speculated that the introduction of a halide anion would not drastically alter the surface composition from those of its fluorinated counterparts.

Comparing the experimental F/C and H/C atomic ratios for [$C_n$mim][PF_6] or [$C_n$mim][BF_4] (n = 4, 8, and 12) with ratios from LOS simulations favors an orientation that places the imidazolium ring close to the surface. With the hexafluorophosphates, the shorter chain cations (n = 4 and 8) appear to adopt similar orientations, favoring an average rotational angle on either side of $\delta = 270^o$ where the

methyl group is uppermost. For the n = 4 and 8 tetrafluoroborates, the cation appears to be oriented such that the average ring rotational angle is near 290°. For both $[C_{12}mim]^+$-containing ILs, the cations favor an orientation that fully exposes the 1-methyl group to the surface plane.

5. SURFACE TENSION MEASUREMENTS OF 1-ALKYL-3-METHYLIMIDAZOLIUM IONIC LIQUIDS

5.1 INTRODUCTION

The concept of surface tension (γ) originated from thermodynamic investigations of the 19th century physicists Gibbs [69] and Young [70] who focused on the dividing surface between two phases. Since the conception of surface tension, chemists have used this macroscopically measurable quantity to describe surface interactions and make generalizations regarding surface molecular orientations. Early 20th century chemists, including Langmuir, Hardy, and Harkins [4] developed principles correlating the surface tension to liquid surface structures. Later work by Good [71] indicated that the surface excess entropy (S_s), calculated from temperature dependent surface tension measurements, could be taken as a criterion for describing the surface orientation of strongly hydrogen-bonded and polar liquids.

Even with the tremendous advances in technology, simple surface tension measurements have proven to be useful to today's scientists in investigating surface phenomena. For example, the surface ordering of long chained *n*-alkanes was first observed from such measurements [72], and later affirmed by such "advanced" techniques as X-ray reflectivity [73] and surface vibrational spectroscopy [74]. As discussed in Chapter 4, we have investigated the surface orientation and composition of room-temperature ionic liquids (Ils) based on the 1-alkyl-3-methylimidazolium cation, utilizing direct recoil spectroscopy (DRS). The work presented in this chapter is an attempt to relate surface tension values, measured by the ring method, to the DRS results. Other surface thermodynamic quantities, such as the surface excess entropy (S_s) and surface excess energy (E_s) were derived from temperature-dependent surface tension measurements.

5.2 BRIEF OVERVIEW OF THE RING METHOD

The γ measurements of ILs were carried out by the ring method, employing a DuNouy tensiometer. As shown in Figure 5.1, a torsion wire is attached to a lever arm from which a ring contacts the liquid surface. Torque (T) is then applied to increase the force (W_{det}) necessary to detach the ring from the surface of a liquid. This detachment force can be determined by

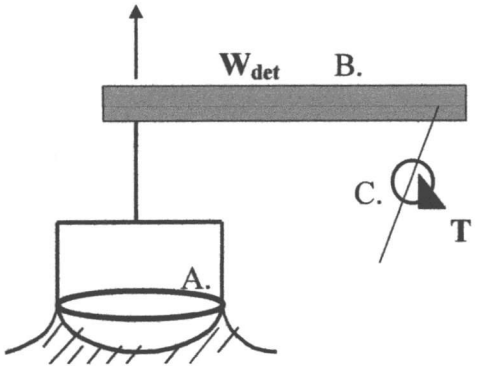

Figure 5.1 Schematic of ring tensiometer: A) Pd-Ir ring, B) lever arm, C) torsion wire

$$W_{det} = W_{ring} + 4\pi R\gamma' \qquad 5.1$$

where W_{ring} is the weight of the ring, R is the ring radius, and γ' is the measured surface tension. However, it was determined by Harkins and Jordan [75] that an empirical correction factor was required because the shapes of the surface inside and outside the ring are not the same. As a result, the vertical components of the force on the ring are not symmetrical. Furthermore, Zudemia and Waters [76] indicated that the liquid density (D) and the phase above the liquid (d) had to be incorporated into this correction factor (f), which can then determined by the relationship,

$$(f - a)^2 = (4b/[\pi^2 R^2])(\gamma'/(D-d)) + 0.04534 - 1.679/(R/r) \qquad 5.2$$

where a = 0.7250 and b = 0.0009075 are universal constants for all ring sizes, and r is the ring wire radius. In general, the second phase over the liquid is air, which has a density that is small relative to the sample liquid, and therefore d in Equation 5.2 can be ignored. The true γ of the liquid can then be calculated by,

$$\gamma = \gamma' f \qquad 5.3$$

5.3 EXPERIMENTAL METHOD

Equilibrium measurements of γ were carried out using a CSC-DuNouy Tensiometer (model 70535) with a platinum-iridium ring of mean circumference of 5.992 cm, and a ring/wire radius ratio (R/r) of 53.6. For this particular apparatus, it was determined that a 10-mL sample in a 50-mL beaker to be sufficient to completely wet the ring, and prevent its interaction with the liquid meniscus.

A sample-heating cell was constructed to measure γ over a range of temperatures. This cell was constructed from 1100-0 aluminum alloy (99% Al) and was mounted onto the tensiometer sample platform. A schematic of this heating cell, including its dimensions, is provided in Figure 5.2. This cell allows for rapid heating/cooling of the sample, and also acts as a thermal buffer. The cell dimensions are such that the spacing between the beaker and the cell walls is minimal, but sufficient to prevent the beaker from being wedged in the cell upon thermal expansion of both the beaker and cell material. To ensure efficient heat transfer to the sample this space was filled with water. Temperature regulated water was pumped from an MGW-Lauda RC3 recirculating chiller/heater through flexible clear plastic tubing to a hose fitting at the top of the cell. The water circulated throughout the cell and passed backed into the chiller/heater. We monitored the temperature using a K-type thermocouple, with the alumel-chromel junction positioned immediately below the liquid surface. Each sample was allowed to attain thermal equilibrium ($1^{\circ}C$ or better) for more than 10 minutes at each temperature setting before measurements. A Plexiglas^{TM} box was placed around the tensiometer to prevent temperature fluctuations due to drafts at the liquid surface. The measured γ values were accurate to 0.1 mJ/m^2. In order to insure cleanliness of the ring, before sample changes, it was cleaned using benzene and methyl ethyl ketone as prescribed by the apparatus manufacturer [77].

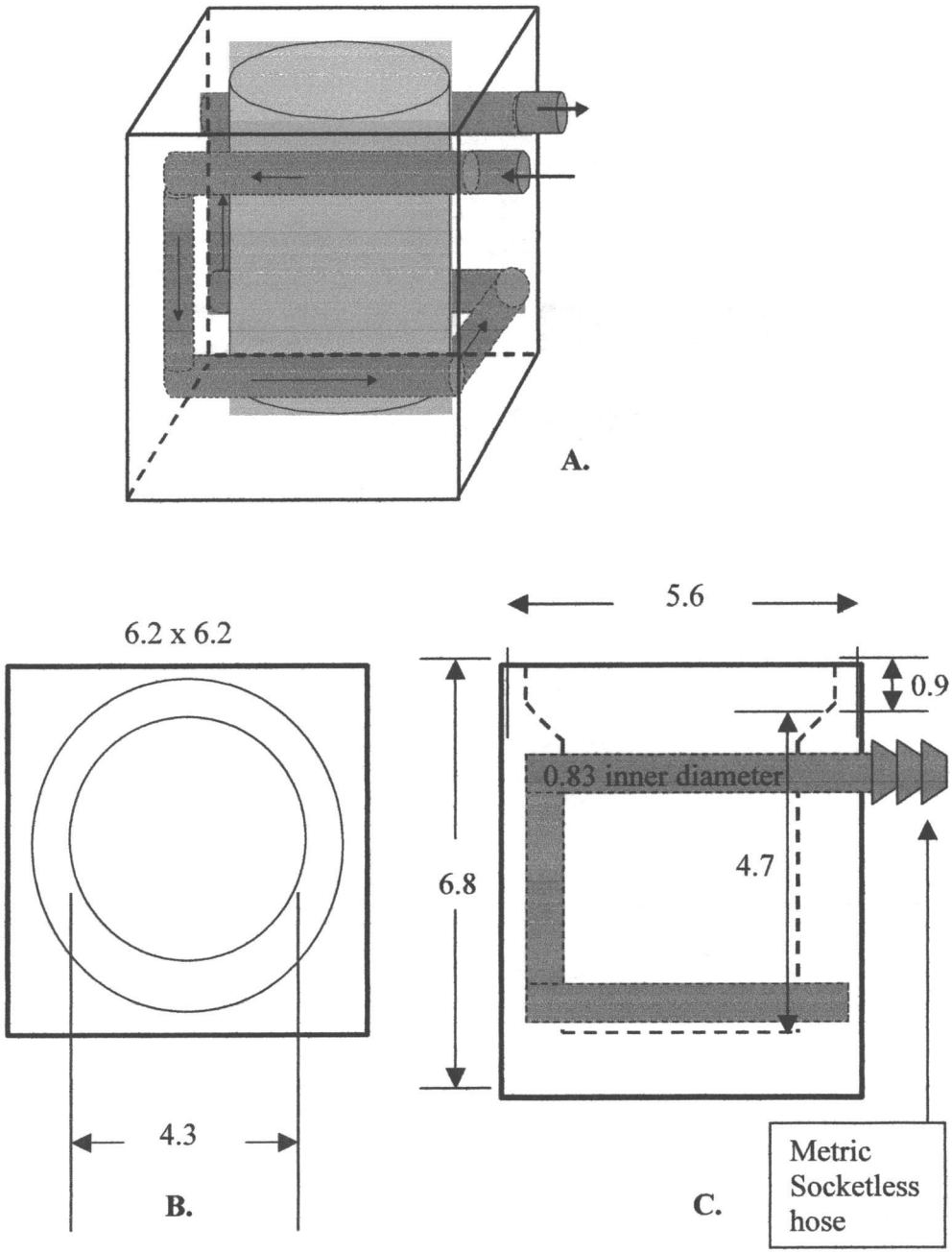

Figure 5.2 Schematic diagram of sample heating cell. A) Exposed view indicating water flow direction. B) Top view of cell. C) Side view. (all dimensions are in mm.)

The true surface tension values from the scaled reading of the tensiometer were obtained using the correction factor discussed in the previous section. The solutions for $(f\text{-}a)^2$ (Equation 5.2) was calculated from a spreadsheet, for the range $0 \leq [\gamma'/(D\text{-}d)] \leq 120$ (where d the density of dry air was approximated to be 0). The correction factors were then calculated and plotted as a function of γ'/D. A second-order fit of the data points generated a readily useable equation for the correction factor for our tensiometer, given by

$$f = -4.0\text{x}10\text{-}6\ (\gamma'/D)^2 + 0.0017(\gamma'/D) + 0.8468 \qquad 5.4$$

As the above equation shows, f depends on sample density, which increases with temperature. Temperature-dependent density measurements were determined by placing 10 mL of an IL sample in a 10-mL volumetric flask. The sample temperature was then increased within the heating cell, and upon thermal equilibrium excess liquid was removed until the sample volume was at 10 mL. The flask containing the sample was then weighed. By doing this over a range of temperature, the temperature dependence of density for an IL was established. The correction factor was then determined for the measured γ at the corresponding temperatures.

Fresh samples of the IL for γ measurements were used as received. The hygroscopic [C_8mim] halides were vacuum dried several times at above 60°C before use. These samples were then transferred directly to a preheated sample container (~60°C), and γ values were obtained at above this temperature. The data for [C_{12}mim][PF_6] were obtained at above its melting point (Tm ~50°C), and for [C_{12}mim][BF_4] data were obtained at above both the clearing (Tc ~29°C) and melting (39°C) points.

5.4 RESULTS

The γ(T) characteristic of ILs is shown in Figure 5.3. In general, for the [$C_n$mim] ILs containing the same anion, γ decreases with increasing alkyl chain length. For for [C_8mim] (n = 8) to 23.6 mJ/m^2 for [C_{12}mim] (n = 12). This temperature was chosen for the comparison as it is one where all the compounds exist as liquids. Table 5.1 lists the γ values, for other ILs at 336 K, and the same trend is observed for the homologous [BF_4]$^-$ series of ILs. This variation of γ with increasing n is the opposite to that observed for *n*-alkanes, *n*-alkenes, nitriles, and acids, but is similar to that of the more complicated *n*-alkyl-phosphonates and *n*-alkyl-diesters [78]. In general, for a fixed cation, the IL with the larger anion has the higher γ. Thus at 336K, for both the [C_4mim] and [C_8mim] series, the ILs containing PF_6^- has a higher γ than those with BF_4^-. Similarly for the halides, [C_8mim][Br] exhibited a higher γ than [C_8mim][Cl]. However, in the cases of the [C_{12}mim] ILs, the presence of a larger anion resulted in a slightly lower γ.

Table 5.1 Surface tension (γ) of the ionic liquids at 336 K

	γ (mJ/m^2) at 336 K		γ (mJ/m^2) at 336 K
[C_4mim][PF_6]	42.9	[C_8mim][Br]	32.0
[C_4mim][BF_4]	38.4	[C_8mim][Cl]	30.5
[C_8mim][PF_6]	32.9	[C_{12}mim][PF_6]	23.6
[C_8mim][BF_4]	29.8	[C_{12}mim][BF_4]	25.2

The behavior in the γ(T) curves for the ionic liquids is similar to most molecular liquids, where γ decreases with temperature. With rare exceptions of a few molten

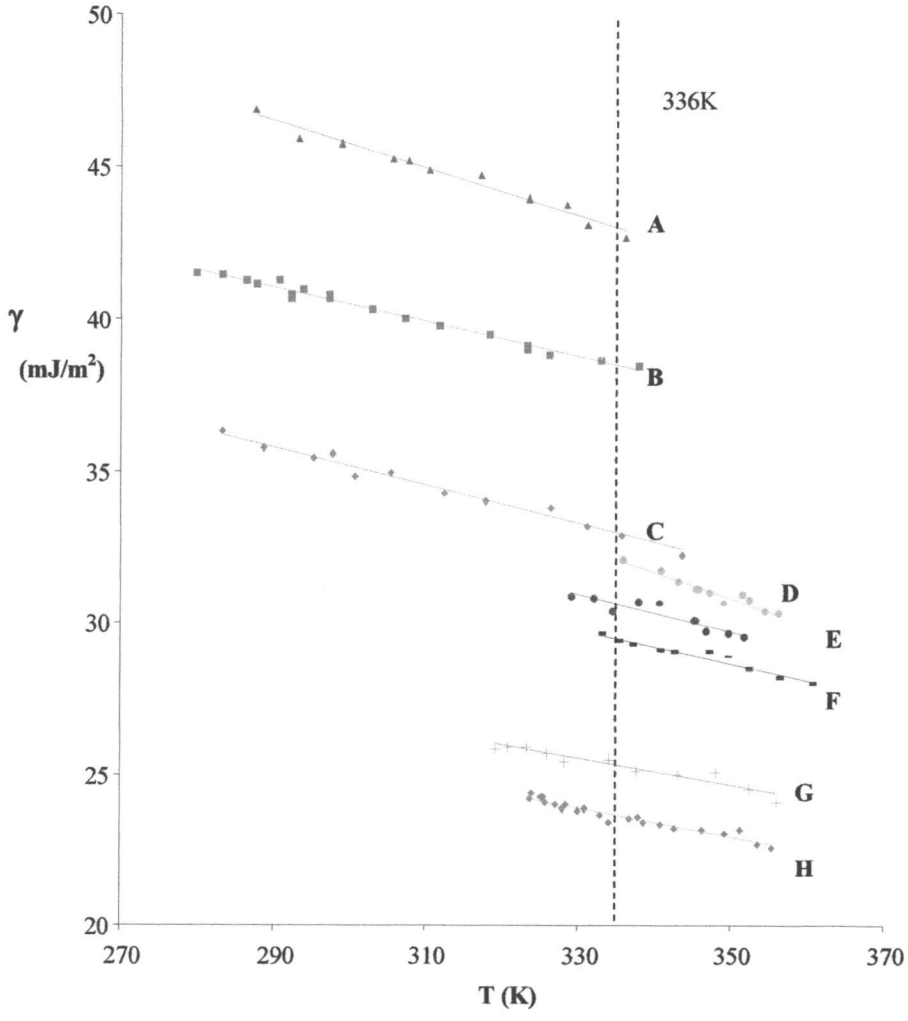

Fig. 5.3 γ (mJ/m^2, ±5 % error) as a function of temperature for the ionic liquids: A=[C_4mim][PF_6], B=[C_4mim][BF_4], C=[C_8mim][PF_6], D=[C_8mim][Br], E=[C_8mim][Cl], F=[C_8mim][BF_4], G=[C_{12}mim][BF_4], H=[C_{12}mim][PF_6]

salts at high temperatures [79], γ can be described as a linearly decreasing function of temperature by

$$\gamma\,(T) = E_s - S_s\,T \qquad 5.5$$

While there is a certain degree of scatter for the data points, γ for the ILs appears to be well described by Equation 5.5. Linear extrapolation of γ for different cations of a common anion show that $\gamma(T)$ converges slowly to high temperatures, which is a similar behavior for the previous mentioned complicated *n*-alkyl molecules. Both E_s and S_s were calculated for the ILs and are listed in Table 5.2. The data indicate that both excess quantities are chain length dependent, with both values decreasing as the 1-alkyl chain length is increased for a particular anion. Hence, the [C_{12}mim] ILs exhibits the lowest excess quantities. As shown in Figure 5.4, for a common cation, a reduction in S_s occurs with decreasing anion size. A similar effect occurs for E_s, as illustrated in Figure 5.5, but for the [C_{12}mim] liquids E_s for both anions are essentially equal.

Table 5.2 Surface excess entropy (Ss), and surface excess energy (Es) of ILs.

	Ss =-dγ/dT (mJ/m^2 K)	E_s (mJ/m^2)
[C_4mim][PF_6]	0.0783 ± 0.0044	69.2 ± 1.4
[C_4mim][BF_4]	0.0572 ± 0.0016	57.6 ± 0.5
[C_8mim][PF_6]	0.0634 ± 0.0029	54.2 ± 0.9
[C_8mim][BF_4]	0.0551 ± 0.0041	47.9 ± 1.4
[C_8mim][Br]	0.0853 ± 0.0081	60.7 ± 2.8
[C_8mim][Cl]	0.0592 ± 0.0088	50.4 ± 3.0
[C_{12}mim][BF_4]	0.0433 ± 0.0046	39.8 ± 1.6
[C_{12}mim][PF_6]	0.0486 ± 0.0026	40.0 ± 0.9

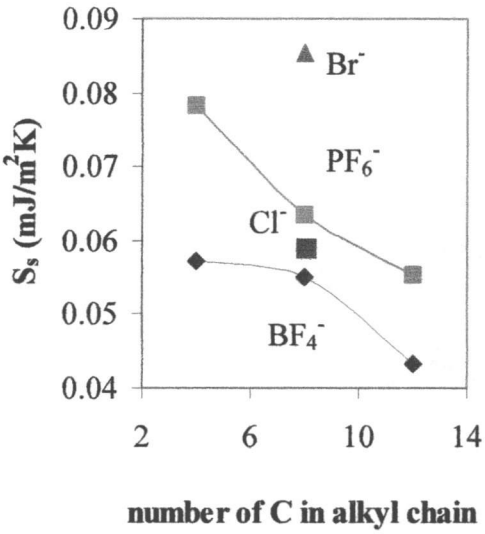

Figure 5.4 Surface excess entropy (Ss) as a function of the number of carbon in chain.

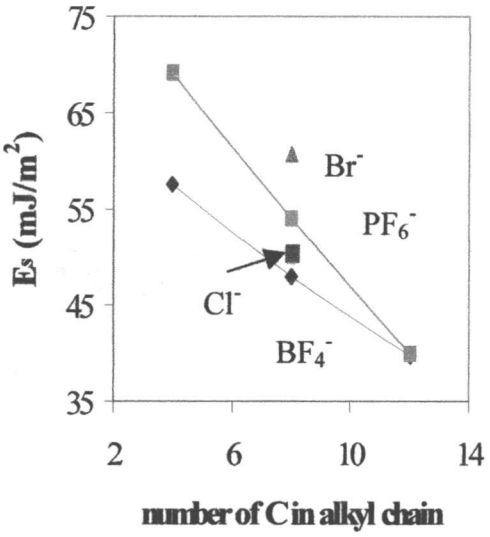

Figure 5.5 Surface excess energy (Es) as a function of the number of carbon in chain.

5.5 DISCUSSION

5.5.1 Surface tension and surface orientation

In general, γ is a reflection of the intermolecular forces between the molecules in the liquid. For example, for nearly spherical molecules of low molecular weight, those with of higher polarity tend to have higher γ. In the case of bulky asymmetrical molecules, as those in ionic liquids, such a generalization cannot be made. Polarity studies on imidazolium ILs using such solvatochromic dyes as Nile Red has shown for a fixed cation, the IL containing the PF_6^- anion is less polar than that with BF_4^- [59]. If we were to use polarity as the criterion in predicting γ, coupling a cation with BF_4^- might result in higher γ. But the data show that for both the 1-butyl and 1-octyl series, replacement of BF_4^- with PF_6^- increased γ. This trend

in γ can be attributed to either ionic segregation and/or to the modifications in molecular orientations of the ionic components.

DRS revealed that for the ILs investigated, the liquid phase boundary is populated by both ionic species with no segregation. So it follows logically that both types of ions contribute, to some degree, to the measured γ. In order to determine the structural contributions to γ, we considered the use of the principle of independent surface action, which was originally proposed by Langmuir [4].

According to this principle, each part or subgroup of an asymmetrical molecule possesses a local surface free energy corresponding to the part that is actually at the surface. For example, methanol has two possible extreme orientations, either the CH_3- or the –OH group can be positioned at the surface. The measured room temperature γ of methanol is 22.5 mJ/m^2, similar to that of many *n*-alkanes (typically 16-27 mJ/m^2)[78], and much lower than that of water (75.8 mJ/m^2)[78], suggesting that the alkyl subgroup is at the surface. This has been shown to be the case with recent studies on methanol using molecular dynamics calculations in conjunction with elliposometry [80]. Other γ investigations on smectic liquid crystals have supported the validity of this principle [81].

While Langmuir's principle has proved to be useful in one-component systems, it has apparently not been used to describe the orientations of more complex systems. The ILs studied here can be considered to be binary-component systems, consisting of the asymmetrical cation and the symmetrical anion. For such a mixture, whether segregation occurs or not, it is necessary to know the γ values of the pure components, the anion (γ_1) and the cation (γ_2), separately. We could not measure the γ of comparable compounds, such as similar substituted 1-alkyl-imidazole, because they are not available. Therefore, we required some model to deduce the individual γ values. Initially, it was assumed that we could make approximations of these values by assuming that the liquids behaved as regular solutions [78]. Then the individual contributions to the "total" γ could be determined by

$$\gamma_{12}=X_1\gamma_1 + X_2\gamma_2 -(A/2RT)(\gamma_1-\gamma_2)^2X_1X_2 \quad 5.6$$

where X_1 and X_2 are the mole fractions of the components, and A is the surface occupancy of the components. This regular solution model has been applied to molten salt mixtures and organic mixtures with some success.

Our assumption was tested using γ data for molten-salt mixtures of KCl-CsCl at 800°C [82]. In this "model" system, γ_{12} would be the γ of the binary mixture KCl-CsCl, and γ_1 and γ_2 would be the γ values of the individual salts. We then expanded Equation 5.6 so that the individual contributions included the anions and cations (γ_{Cs+}, γ_{K+}, and γ_{Cl-}), which resulted in a 5x5 mathematical matrix. Attempts to generate solutions to the ionic contributions were carried out using both Maple™ and Mathcad™, without success. With hindsight, such a method would not work for the spherical ions in a KCl-CsCl mixture. The surface could not consist of one type of ion, and in order to maintain electroneutrality the surface charge would have to be balanced by an equal but oppositely charged atmosphere of counterions.

We can still make generalizations concerning the contributions of the different molecular subgroups of the ILs to the measured γ. The γ of imidazole (Tm = 363 K) extrapolated to 336 K is 40.3 mJ/m^2 [83], while those for *n*-alkanes tend to range from 14 (6-carbon chain) to 25 mJ/m^2 (20-carbon chain) at the same temperature [6]. While there is no published γ data for fluorinated inorganic compounds containing boron or phosphorus (either BF_3 or PF_5), it can be noted that γ values of other similar halides tend to be low (at 336 K, γ is 23.5 for PCl_3, and is 14.8 mJ/m^2 for $SiCl_4$ [6]). Fluorination tends to lower γ further [81], and we can assume that fluorinated inorganics containing B or P to have a γ either close to or lower than PCl_3 or $SiCl_4$. Due to the symmetry of the anions of the ILs, anion orientation would not be a factor in variations in γ. The overall contribution to the measured γ for a particular IL is most likely based on the cation orientation with modifications by the presence of anions at the surface. However, it can pointed out that, for both the 1-octyl and 1-

butyl ILs, replacement of the larger PF_6^- anion with the smaller one resulted in a ~10% decrease in the surface tension.

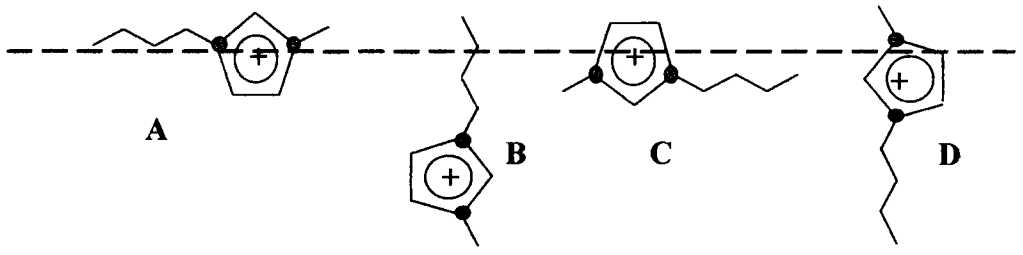

Figure 5.6 Extreme orientations of the imidazolium cation (C4) based on rotation about the ring axis (rotational angle = δ): A) N-up (δ = 0°), B) C_n-up (δ = 90°), C) N-down (δ = 180°), and D) Me-up (δ = 270°)

As shown in Figure 5.6, four extreme cation orientations are possible for the ILs. These orientations were described in the previous chapter, as defined by the rotational angle (δ) based on the ring axis. Because the Coulombic interaction is fairly strong, the anion would be expected to situate close to the imidazolium ring. With such an arrangement, the alkyl tails are flexible enough to lead to gauche conformations. Such conformation exposes a significant number of $-CH_2-$ groups at the interface, which increases with the alkyl chain length. Calculations carried out by Kloubek on *n*-alkanes [68] and perflurohydrocarbons [84] have indicated that the measured γ is additively composed of the individual group contributions (CH_3-, and $-CH_2-$ for *n*- alkanes), which can be used to explain the observed *increase* in γ with chain length. We saw earlier (Figure 5.3) that, for a particular anion, an increase in the alkyl chain length resulted in a *decrease* in the measured IL γ, suggesting that the 1-alkyl chain is not at the surface for all cases.

The DRS measurements suggest that the two average orientation of the imidazolium ring are possible (δ ~260°, and δ ~320°) for $[C_4mim][PF_6]$ and

$[C_8mim][PF_6]$, both of which place the ring near orientation D. For $[C_4mim][PF_6]$, the measured γ does not correlate with the DRS findings. The γ values suggest an orientation, which fully exposes the imidazolium ring at the surface (either N-up or N-down). For $[C_8mim][PF_6]$ with a similar orientation as the n = 4 analog, γ decreases by 23 % (as compared to $[C_4mim][PF_6]$) to values that are intermediate between those of alkanes and imidazole. A similar trend was observed for the tetrafluoroborate ILs with an increase in the chain length from n = 4 to n = 8, resulting in the measured γ decreasing by 23%. From DRS, it was suggested than both borates adopt an orientation with a rotational angle of ~290°. This may point out that for the ILs with the smaller cation, the imidazolium ring has a greater effect on γ. Whereas, for the n = 8 ILs, the 1-octyl chain has a larger effect in γ than the ring structure.

On the other hand, for the $[C_{12}mim]$ series, the γ values are close to those of alkanes, which is an indication that either the methyl or dodecyl group is at the surface. However, from γ data alone it is difficult to determine which is at the surface. But DRS data indicated that for the longer chain ILs, the ring rotates to put the 3-methyl group at the surface. The low γ values of both n = 12 compounds suggest that the methyl group has a greater influence on γ. Whereas, changing the anion type has little or no effect.

5.5.2 Surface excess quantities of ionic liquids

The temperature dependence of γ was previously described by Equation 5.5. Es can be described as the amount of energy required to transfer molecules from the bulk in extending the surface. Ss is related to the disordering or ordering of the molecules at the surface with respect to the bulk. If the molecules are more ordered at the surface relative to molecules in the bulk, Ss will be a positive value.

There is strong experimental evidence that the ordering of molecules at the surface is reflected in Es. Investigations from light scattering and heats of mixing measurements have indicated that this is the case for higher n-alkanes, where the molecules tend to orient parallel to the surface at temperatures near the melting point [6]. Only for simple molecules such as water and methanol, do empirical models exists to account for this orientational entropic effect [71]. Development of models to explain the lower entropy for complex molecules such as the ILs is beyond the scope of this investigation, and we shall adhere to a qualitative approach.

As shown in Figure 5.7, Es and Ss for the ILs have been compared to some n-alkanes and heterocycles [78]. For $[C_4mim][PF_6]$, the calculated Ss is close to that of imidazole. This IL exhibits a similar Es to heterocycles such as pyrrole and quinoline [78], but with a much lower Ss value. In fact, imidazole is unusual in this respect in the context of organic molecules in general, which usually have entropies greater than 0.075 mJ/m^2K. The fluorine-containing ILs other than $[C_4mim][PF_6]$ all have lower surface entropies than imidazole, and they decrease with increasing alkyl chain length. The decrease in surface entropy with chain length is also seen for *n*-alkanes and linear aliphatic compounds, and is usually taken to indicate an increased degree of surface orientation [6]. While Ss values offer an insight on the relative order of the surface molecules compared to those in the bulk, it is not clear how the values imply to the preferential orientation of the molecules at the surface. The lower entropies of those ILs with bulkier cation may suggest preference of one molecular group over others at the surface.

In comparing Es, the ILs exhibit a decrease in this value with increasing 1-alkyl chain length, similar to that observed with linear aliphatic compounds such as *n*-alcohols, *n*-acids, and amines. On increasing the alkyl chain length, Van der Waals

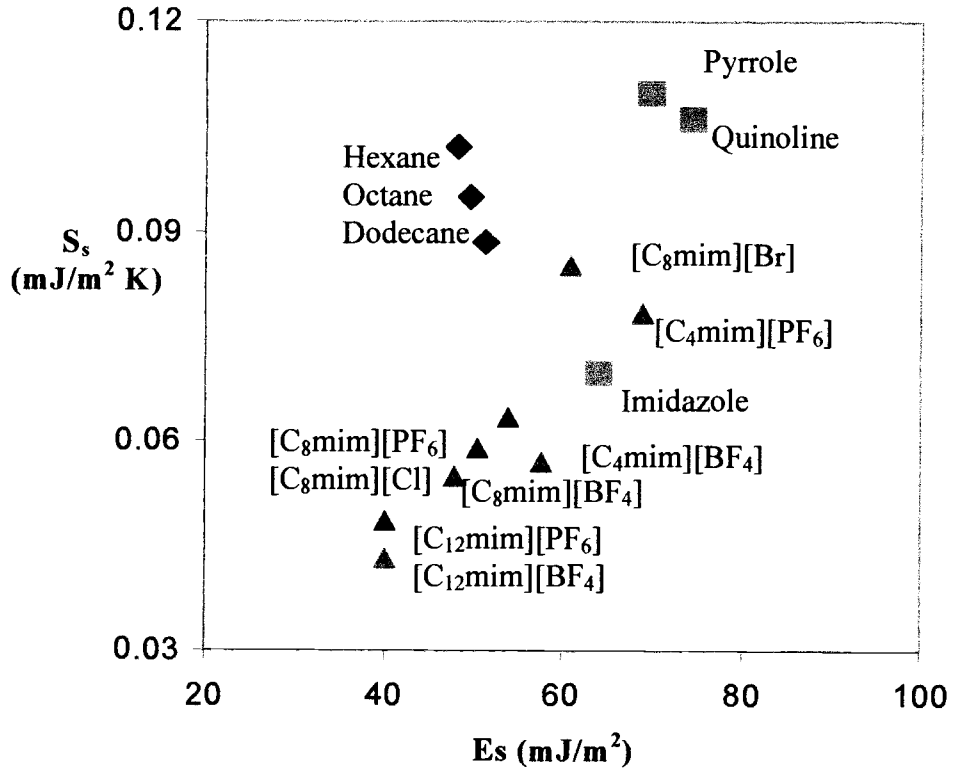

Figure 5.7 Plot of surface excess entropy (Ss) versus surface excess energy (Es) for the ionic liquids, and a series of *n*-alkanes and heterocycles.

interactions increase and such compounds exhibit amphiphilic characteristics. This chain length dependence of the surface energy may be an indication that as the chain length increases any influence of the anion on the surface energy is rapidly quenched, and for the dodecyl ILs the surface energy is dominated by the cation. For ILs the increased amphiphilicity of those with bulkier cations is apparent since they exhibit surface energies similar to n-alkanes. Also for ILs with the same alkyl chain length, we observed a drop in the surface energy for a smaller anion (BF_4^- versus PF_6^-).

5.6 CONCLUSION

The surface tensions of a series of 1-alkyl-3-methylimidazolium ionic liquids were measured over a range of temperatures using a DuNouy tensiometer. The measured γ values indicate a trend based on the 1-alkyl substituent chain length. For example, for those coupled with the phosphate anion, the measured values decreased from 45 mJ/m^2 (for $[C_4mim]$) to 33 mJ/m^2 (for $[C_8mim]$) to 24 mJ/m^2 (for $[C_{12}mim]$). Also for a particular cation, the ILs with the smaller anion had a lower γ value. The γ data do not clearly support the DRS findings, but do suggest that for the 1-octyl and 1-dodecyl salts, the 1-methyl group has a greater effect on the surface energetic. The γ values showed a linear decrease with increasing temperature, allowing for the calculations of Es and Ss. Both excess quantities are alkyl chain length dependent, and decrease as the chain length increases. This indicates some increased degree of order with the larger cations. For a common cation, a reduction in Ss occurs with decreasing anion size. A similar effect occurs in Es when changing the anion for the shorter alkyl chain compounds.

6. SURFACE COMPOSITION OF MIXTURES OF ROOM TEMPERATURE IONIC LIQUIDS

6.1 INTRODUCTION

The previous two chapters described the DRS and γ experiments carried out on neat ILs. With this understanding of the pure liquids, the next step would be to study the surface behavior of ILs in catalyst solutions. Reports of biphasic catalysts used with ILs include $[H_4Ru_4(\eta^6\text{-}C_6H_6)_4][BF_4]_2$ dissolved in $[C_4mim][BF_4]$ for arene hydrogenation [85], and Pd in [C4mim][Cl] for allylic alkylation [86]. Dialkylimidazolium IL mixtures have also been utilized in the biphasic hydrogenation of poly(acrylonitrile-butadiene) rubbers (NBR) catalyzed by $RuHCl(CO)(PCy_3)_2$ [86]. Several important questions arise regarding the interface of such solutions. What would be the surface composition of the catalyst? Does the introduction of the catalyst change the surface orientation of the IL cation?

Prior to answering such questions, we must determine if it is possible to use DRS to analyze the surfaces of liquids. However such experiments are not without difficulties. For dilute solutions in which the surface composition is similar to that of the bulk, we may expect a weak or absence of DR signals from the solvent atoms. Furthermore, for solutions in which the solute and solvent contain the same atomic species (such as $H_4Ru_4(\eta^6\text{-}C_6H_6)_4][BF_4]_2$ dissolved in $[C_4mim][BF_4]$), the overlapping of the DR peaks may present obstacles in the analysis. The work discussed in this chapter represents the first attempt to examine the surface behavior of mixtures (solutions) of room-temperature ILs containing the 1-alkyl-3-methylimidazolium cation using DRS. As with the neat liquids, the DRS results were compared to those from γ measurements.

6.2 EXPERIMENTAL METHOD

The ILs were obtained from Professor Seddon. The mixtures were prepared by dissolving either $[C_{12}mim][BF_4]$ or $[C_{12}mim][PF_6]$ in $[C_4mim][BF_4]$. The γ values of the mixtures were measured as described in Chapter 5.

For DRS, the samples were degassed in the spectrometer for ~12 hours. The ion beams were generated from ultra-high-purity Ne (Matheson), and high-purity Ar (Matheson). In order to ensure that the solutes remained in solution, the scans were taken at 55°C. The temperature was regulated with the MGW-Lauda RC3 recirculating chiller/heater ($\pm$1°C stability), while the temperature in the liquid cell was monitored with a K-type thermocouple. The spectra were obtained using incident energies of 2.0-keV Ne^+ and 2.5-keV Ar^+, over an α range from 8° to 36°. The data analysis was carried out according to procedures mentioned in previous chapters.

6.3 RESULTS

6.3.1 DR spectra of ionic liquid mixtures

6.3.1.1 $[C_{12}mim][BF_4]$ (25.5 mole %) in $[C_4mim][BF_4]$

The spectra obtained from 25.5 mole % solution of $[C_{12}mim][BF_4]$ in $[C_4mim][BF_4]$, obtaining using 2.0-keV Ne^+ over 8° to 36° for α is shown in Figure 6.1. The three spectral features are attributed to hydrogen recoils (~5.8 μs), carbon recoils (~8.8 μs), and fluorine recoils (~10.8 μs). The latter two recoil peaks are better resolved at higher α. The nitrogen recoils (expected at ~9.39 μs) is too close to completely resolve from the C(DR) peak, and signals due to phosphorus recoils

and the single scattering of Ne^+ from P are not observed. The MS features at longer flight times are not very obvious in the Ne^+ spectra.

Figure 6.2 illustrates the spectra of this mixture taken with 2.50-keV Ar^+. The H(DR) and C(DR) signals are close to the predicted values (~7.16 μs and ~9.1 μs, respectively). Unlike the ILs containing the smaller cation, the F(DR) signal (~10.31 μs) for the mixture is not well defined as a shoulder, and the N(DR) peak is unresolved. The broad feature, centered at ~15 μs, that is attributed to the multiple scattering of Ar^+ is not observed in this data set.

The normalized spectra for $[C_{12}mim][BF_4]$ in $[C_4mim][BF_4]$, neat $[C_4mim][BF_4]$, and neat $[C_{12}mim][BF_4]$ taken with 2.0-keV Ne^+ at $\alpha = 16^o$ are shown in Figure 6.3. The mixture exhibits similar DR features as both neat ILs. As the figure clearly displays, the C (DR) signal intensity is approximately similar for all three liquids. The F (DR) signal intensity of the mixture is between the neat liquids but closer to $[C_{12}mim][BF_4]$. These two observations were true at all α.

6.3.1.2 $[C_{12}mim][PF_6]$ (25.3 mole %) in $[C_4mim][BF_4]$

DR spectra were also obtained for 25.3 mole % $[C_{12}mim][PF_6]$ in $[C_4mim][BF_4]$ from 2.0-keV Ne^+ and from 2.5-keV Ar^+. The spectra for this mixture taken with both ions can be found in Appendix B. Figure 6.4 illustrates the normalized spectra for this mixture, and both the neat solute and solvent from 2.0-keV Ne^+ at $\alpha = 16^o$. For this scan, as with Ne^+ at all α, the direct recoil signals of H, C, and F are observed at their predicted TOF. The spectral features observed for this mixture with 2.5-keV Ar^+ are also consistent with those of the neat liquids. As shown in the figure, C signal is similar in intensity for all three liquids. However, the F (DR) signal is the smallest when compared to the neat liquids.

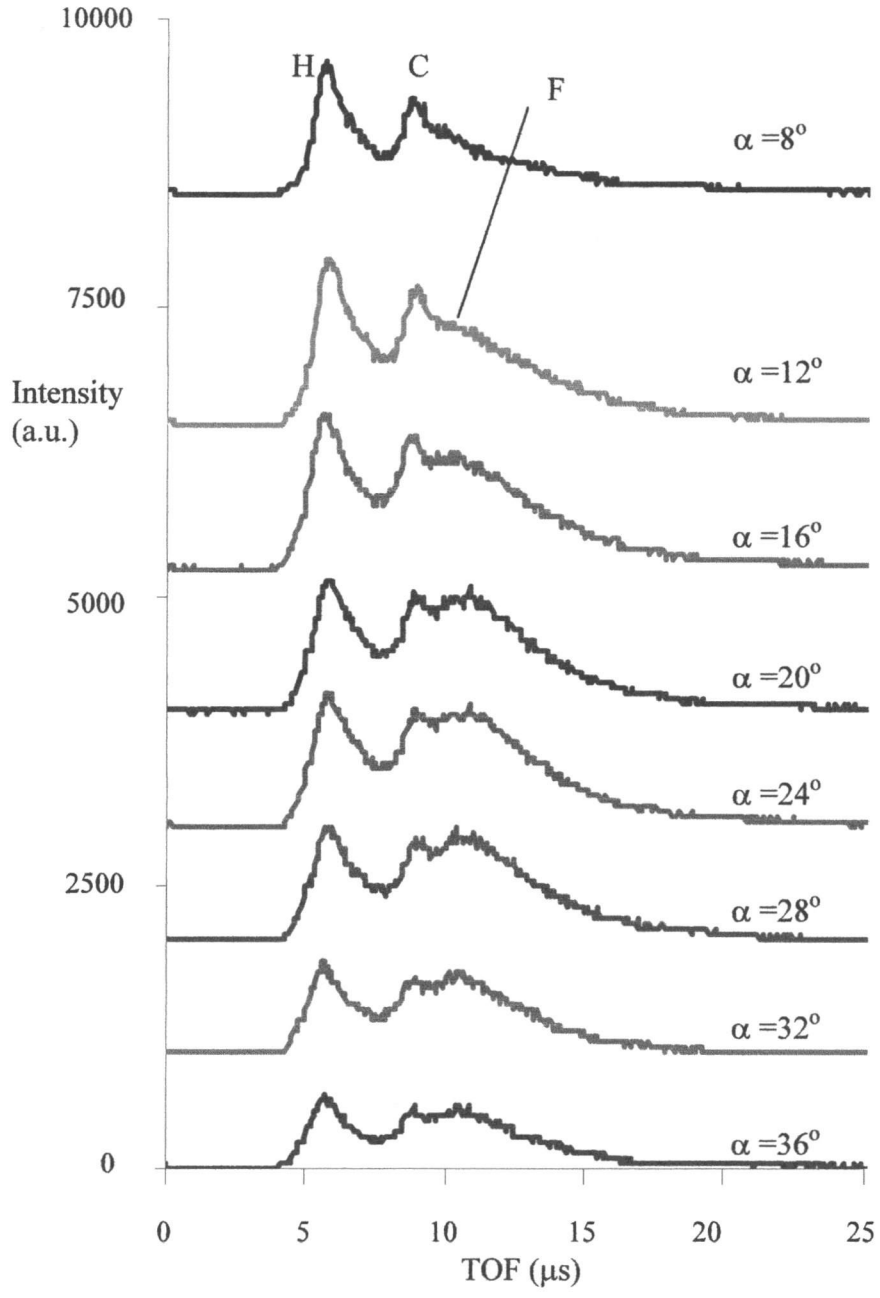

Figure 6.1 – Spectra obtained from $[C_{12}mim][BF_4]$ (25.5 mole %) in $[C_4mim][BF_4]$ using 2.0-keV Ne^+

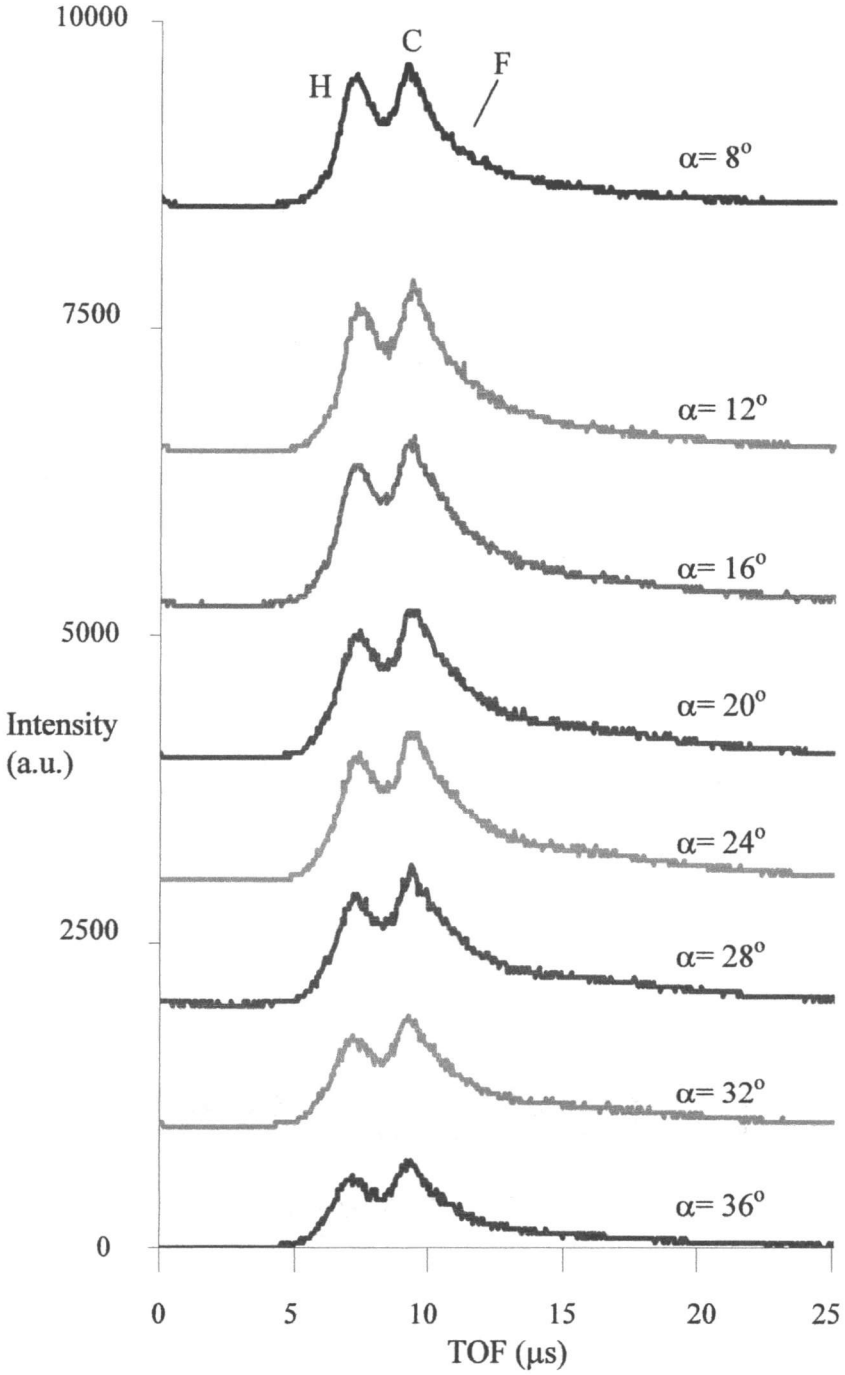

Figure 6.2 Spectra obtained from $[C_{12}mim][BF_4]$ (25.5 mole %) in $[C_4mim][BF_4]$ using 2.5-keV Ar^+

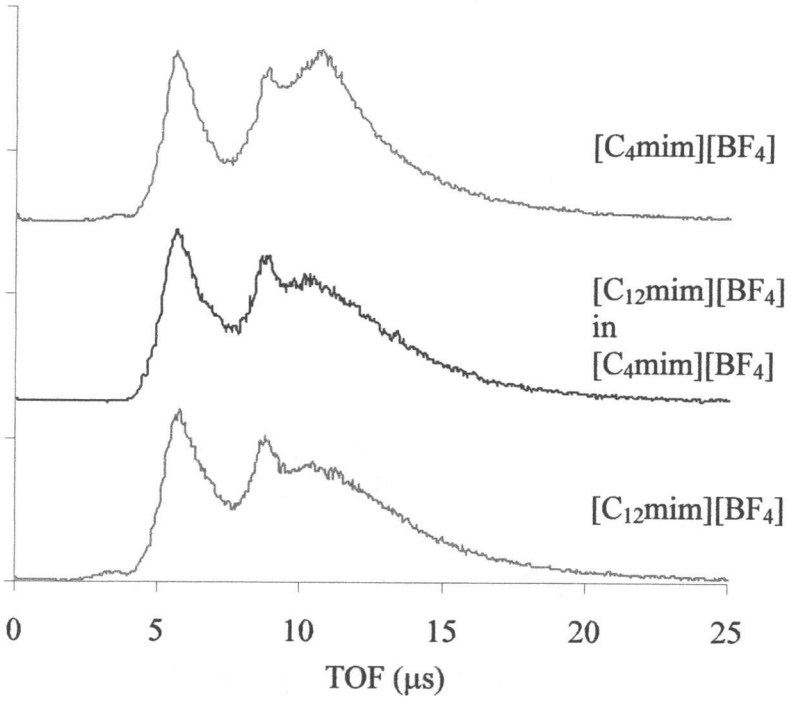

Figure 6.3 Normalized DR spectra of $[C_{12}mim][BF_4]$ (25.5 mole %) in $[C_4mim][BF_4]$, neat $[C_4mim][BF_4]$, and $[C_{12}mim][BF_4]$ taken with 2.00-keV Ne^+ at $\alpha = 16^o$

6.3.2 Surface tension of the ionic liquid mixtures

The surface tensions (γ) as a function of temperature for the two mixtures, as well as the fluorinated ILs containing the $[C_4mim]$ and $[C_{12}mim]$ cations are shown in Figure 6.5. The $\gamma(T)$ curves of the two mixtures are located somewhere between the respective solutes and solvents. In the case of **solution A** (25.5 mole % $[C_{12}mim][BF_4]$ in $[C_4mim][BF_4]$), the γ values are closer to that of the neat solute (at 328 K: 26.7 mJ/m^2 for mixture B, 25.6 mJ/m^2 for the solute). With **solution B** (25.3 mole % $[C_{12}mim][PF_6]$ in $[C_4mim][BF_4]$), the curve is located about midway between that of $[C_4mim][BF_4]$ and $[C_{12}mim][PF_6]$. At 328 K, γ of this mixture is 32.3 mJ/m^2, and 24.1 mJ/m^2 for the solute, and 38.8 mJ/m^2 for the solvent.

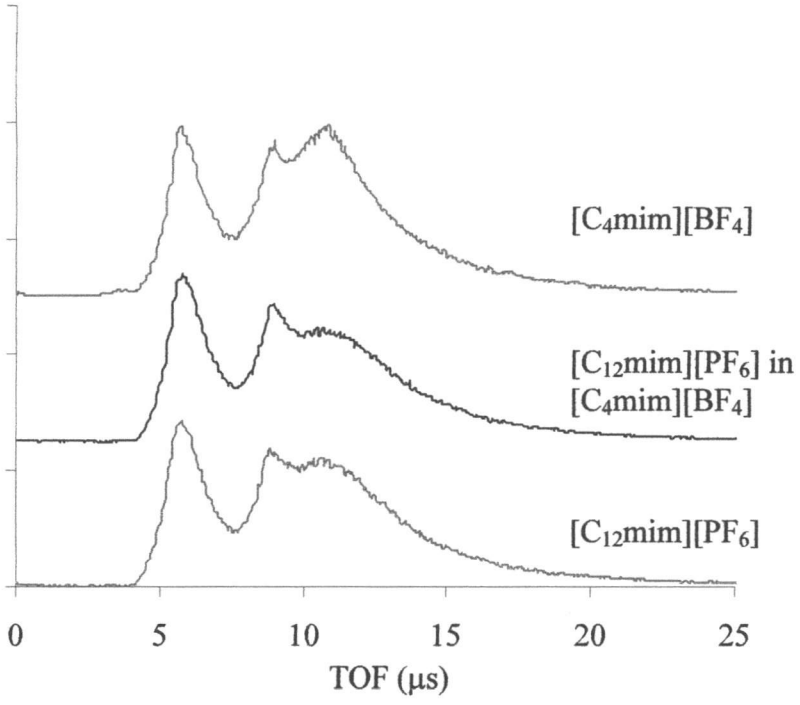

Figure 6.4 Normalized DR spectra of the $[C_{12}mim][PF_6]$ (25.3 mole %) in $[C_4mim][BF_4]$, neat $[C_4mim][BF_4]$, and $[C_{12}mim][BF_4]$ taken with 2.00-keV Ne^+ at $\alpha = 16^o$

As with most liquids, γ of the ILs and the mixtures decreases with temperature. The $\gamma(T)$ curve can be described by Equation 5.5. Ss and Es of the mixtures and the neat ILs were calculated using this equation and are listed in Table 6.1 along with the values of γ at 328 K. Again the Ss value is assumed to be temperature independent.

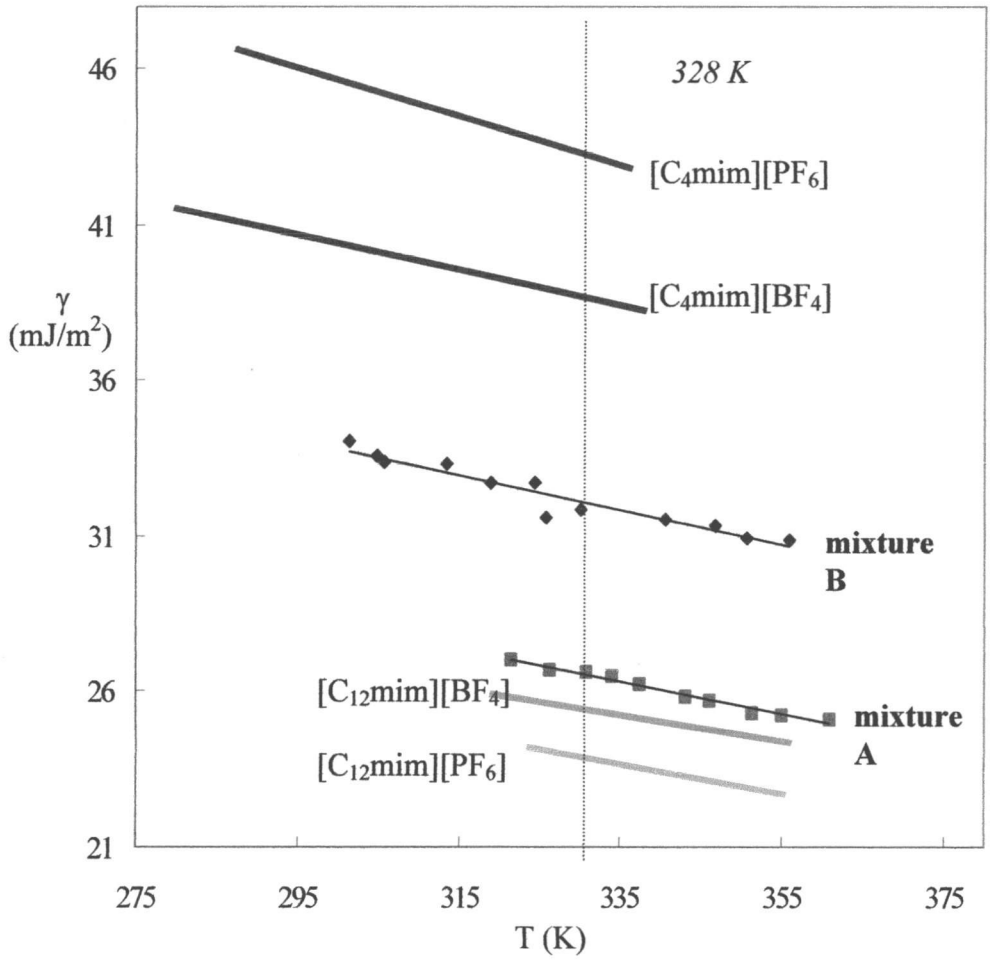

Figure 6.5 Surface tension (γ, ±5 %) as a function of temperature for several neat ILs and the two mixtures: solution A is $[C_{12}mim][BF_4]$ (25.5 mole%) in $[C_4mim][BF_4]$, and solution B is $[C_{12}mim][PF_6]$ (25.3 mole %) in $[C_4mim][BF_4]$

6.4 DISCUSSION

For both solutions, the presence of recoiled species from H and C in both the Ne^+ and Ar^+ spectra indicates the presence in the surface of at least one type of cation. Similarly the occurrence of F signals in all spectra shows the presence of the anion.

Table 6.1 Surface excess entropy (S_s), surface excess energy (E_s), and surface tension (γ) (at 328 K) of the IL mixtures and some neat ILs

	γ (mJ/m^2) at 328 K	Ss (mJ/m^{2}K)	Es (mJ/m^2)
Mixture A	26.7	0.0523±0.0031	43.9±0.9
Mixture B	32.3	0.0565±0.0024	50.8±1.2
[C_4mim][PF_6]	43.5	0.0783±0.0044	69.2±1.4
[C_4mim][BF_4]	38.8	0.0572±0.0016	57.6±0.5
[C_{12}mim][BF_4]	25.6	0.0433±0.0046	39.8±1.6
[C_{12}mim][PF_6]	24.1	0.0486±0.0026	40.0±0.9

As mentioned in Chapter 4, with the pure ILs both types of charges share the surface as ion pairs, with a 1:1 cation-anion stochiometric ratio. Works on molten salt binary mixtures [87] have shown that the electroneutrality constraints (1:1 anion/cation ratio) are maintained at the surface. Here the question of interest is whether the bulk cation composition (~25 mol%) is maintained at the surface.

6.4.1 Mixture A – (25.5 mol % [C_{12}mim][BF_4] in [C_4mim][BF_4])

As shown in Figure 6.3, the spectral intensities of mixture A ([C_{12}mim][BF_4] in [C_4mim][BF_4]) are similar to that of the pure solute. Furthermore, γ of the mixture (shown in Figure 6.5) is close to that of [C_{12}mim][BF_4]. These observations indicate that the surface is composed predominately of that material. This simple argument relies on the assumption that the DR spectrum or the γ of each component of the mixture remains the same as the pure components. This is only likely true, for the DR spectra at least, if the cations involved do not undergo significant reorientation in

the mixture relative to the pure liquid. The anions are spherically symmetric, so anion orientation is not an issue.

We can advance arguments that it is improbable that the surface orientation of the [C_{12}mim] and/or the [C_4mim] cation would change significantly in solution compared to the pure liquids. In the pure ILs both cations have similar surface orientations where the imidazolium ring is perpendicular to the surface, with an average rotational angle that exposes the 1-methyl group at the surface ($\delta \sim 270^{o}$). The similar cation orientation in the pure materials is reflected in the closely similar H(DR) and C(DR) regions in the spectra of these materials (Figure 6.3). The main difference in the DR spectra of [C_4mim][BF_4] and [C_{12}mim][BF_4] lies in the reduced F(DR) signal in the latter, which is attributed to the dilution of F atoms in the longer alkyl chain molecule.

The measured surface entropies of [C_4mim][BF_4] (0.0433 mJ/m^{2}K) and [C_{12}mim][BF_4] (0.0572 mJ/m^{2}K) are also quite similar. The surface entropy of mixture A (0.0523 mJ/m^2) is between the values of the pure component. If we argue that the surface entropy is related to the surface orientation then it is reasonable to suppose that the orientations of the solvent and solute cations, in the mixture A, are similar to their counterparts in the neat liquids.

We can also pursue the logical result, in terms of surface tension, of a solution A that is highly enriched in solute. A surface solute [C_{12}mim] cation in such an environment would find itself largely surrounded by [BF_4] anions, as both the solute and solvent have common anions, and by other [C_{12}mim] cations. Hence, the local surface environment of a cation (and anion) in a highly enriched solution A is little different from that in pure [C_{12}mim][BF_4]. Thus, there would be little incentive for the cation to change its orientation in the mixture from that in the pure IL.

So, a solution A that is highly surface enriched in solute would be expected to have surface [C_{12}mim] cations with a similar orientation to those in the pure IL and therefore a γ value close to that of pure [C_{12}mim][BF_4]. As this is exactly what is

observed, there is no need, or reason, to invoke orientation changes to adequately explain the observed γ values.

We can go further and quantify the surface composition from γ measurements within the assumption of no cation reorientation. In the case where the polar components are of different molecular dimensions, the solution's γ ($\gamma_{1\text{-}2}$) can be related to the individual surface tensions (γ_1 and γ_2) by [84]

$$\gamma_{1\text{-}2} = y_1^{\sigma}\gamma_1 + y_2^{\sigma}\gamma_2 + 0.5\,(\gamma_1 - \gamma_2)^2/RT\,(y_1^{\sigma}\Sigma_2 + y_2^{\sigma}\Sigma_1)(y_1^{\sigma}\,y_2^{\sigma}) \qquad 6.1$$

In equation 6.1, Σ_1 and Σ_2 are the molar surface areas of respective species in the neat liquid, and y_1^{σ} and y_2^{σ} are the surface fractions. The molar surface area can be estimated using $\Sigma_i = N^{1/3}\,V_i^{2/3}$ (N is Avagadro's number, and V_i is the molar volume of species *i*). The surface fractions are defined as follows

$$y_1^{\sigma} = x_1^{\sigma}\Sigma_1 / (x_1^{\sigma}\Sigma_1 + x_2^{\sigma}\Sigma_2) \qquad 6.2$$

and

$$y_2^{\sigma} = x_2^{\sigma}\Sigma_2 / (x_1^{\sigma}\Sigma_1 + x_2^{\sigma}\Sigma_2) \qquad 6.3$$

where x_1^{σ} and x_2^{σ} are the surface mole fractions. The values of the fractions and the various parameters utilized in this mathematical treatment are shown in Table 6.3. We obtain a value (from Equation 6.1) for the surface mole fraction for $[C_{12}mim][BF_4]$ of $x_1^{\sigma} = 0.93$, confirming our intial impression of a highly solute-enriched surface.

Table 6.3 – Surface mole fractions (x_i^{σ}) of ionic liquid mixture A, calculated with Equation 6.4.1, at 328 K

	Mixture A $[C_{12}mim][BF_4]$ = liquid 1 $[C_4mim][BF_4]$ = liquid 2
V_1 (cm^2/mol)	337.8
V_2 (cm^2/mol)	196.5
Σ_1 (cm^2/mol)	4.10×10^9
Σ_2 (cm^2/mol)	2.85×10^9
y_1^{σ}	0.95
y_2^{σ}	0.05
x_1^{σ}	0.93
x_2^{σ}	0.07

For the recoil spectrum, the signal intensities of the solution are then linearly dependent on the surface mole fraction (x_i^{σ}) and the intensities of the pure components (I_i). The binary mixture's spectral intensity (I_{mix}) at any TOF can then be determined by

$$I_{mix} = x_1^{\sigma} I_1 + x_2^{\sigma} I_2 \qquad 6.4$$

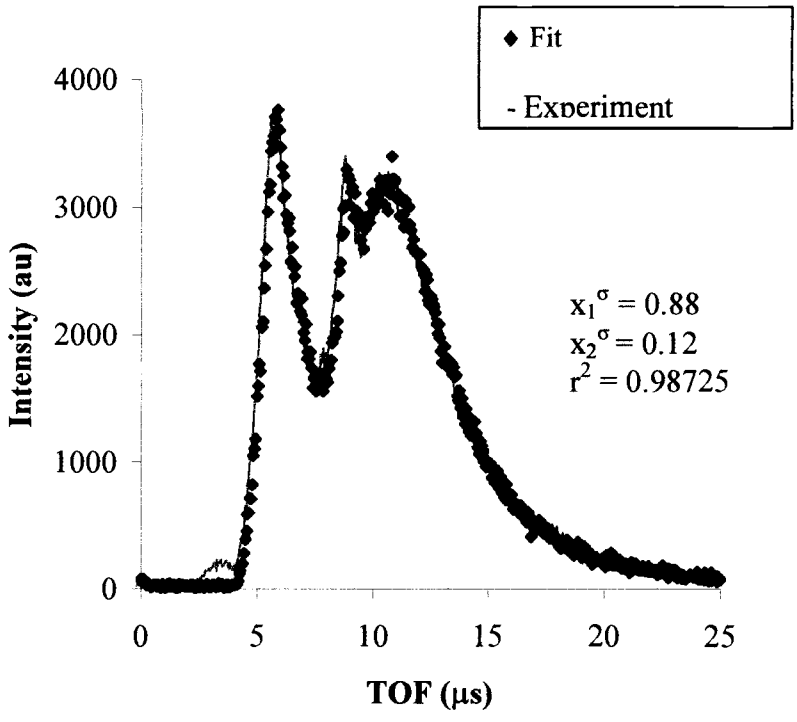

Figure 6.6 Example of Solver fit for solution A: Spectra obtained from 2.0-keV Ne^+ at a = 16°; liquid 1 is $[C_{12}mim][BF_4]$ and 2 is $[C_4mim][BF_4]$

To solve for the surface mole fractions, a non-linear fit of the pure liquid spectra to that of the mixture. An example of such a fit for solution A (taken with 2.0-keV Ne^+ at $\alpha = 24°$) is shown in Figure 6.6. The fit generated DR peaks overlap well with those from experiment, and the only region that does not fit well, at a TOF of ~4 μs, corresponds to the H (SR) surface recoils. These are recoiled H atoms that have been subsequently scattered by interaction with another atom as they leave the surface. Surface recoil peaks are always very small and their appearance in spectra is not very well understood and this region of the spectrum was not included in the fit. Values of x_1^{σ} were determined from the solver spectral fits of mixture A, at all α,

yielding an average value of 0.86 (average deviation = $\pm$0.10). This value compares well (7.8% difference) with that obtained from the surface tension data.

6.4.2 Mixture B – (25.3 mol % $[C_{12}mim][PF_6]$ in $[C_4mim][BF_4]$)

The analysis of solution B (25.3 mol % $[C_{12}mim][PF_6]$ in $[C_4mim][BF_4]$) is complicated by the absence of common ions between the components. In this solution, there may be the possibility of the formation of four ion pairs ($[C_{12}mim][PF_6]$, $[C_4mim][BF_4]$, $[C_{12}mim][BF_4]$, and $[C_4mim][PF_6]$) at the surface. Figure 6.5 shows that both $[C_{12}mim]$ species are low-surface-energy materials and hence we might expect surface enhancement of them in a similar manner that we saw in mixture A.

From Figure 6.4 we can see that the DR spectrum from the mixture does resemble that of the solute rather than that of the solvent. In particular, the F region of the spectra (near 11 μs) clearly points to a surface with a low concentration of that element. We attempted to fit the DR spectra from mixture B to the sum of the spectra from the pure solute and solvent components assuming no change in cation orientation (as with mixture A). However, for mixture B, we found difficulty in finding fits that accurately reproduced the H and C regions (example is shown in Figure 6.7). Although on the scale of Figure 6.4, the H and C regions of all spectra look very similar, there are significant differences in the shapes of the H and C peaks and the dip in between them from spectrum to spectrum. The best-fit values for the surface mole fraction of $[C_{12}mim][PF_6]$ in $[C_4mim][BF_4]$ over all angles averaged 0.8 but the fits are sufficiently poor that we cannot regard this value as being reliable.

The γ data from Figure 6.5 clearly shows that changing the anion for a common cation produces a much less dramatic change in γ than changing the cation for a common anion. The effect of changing the anion is more marked for the smaller $[C_4mim]$ cation, but even that change is dwarfed by the effect of increasing the size

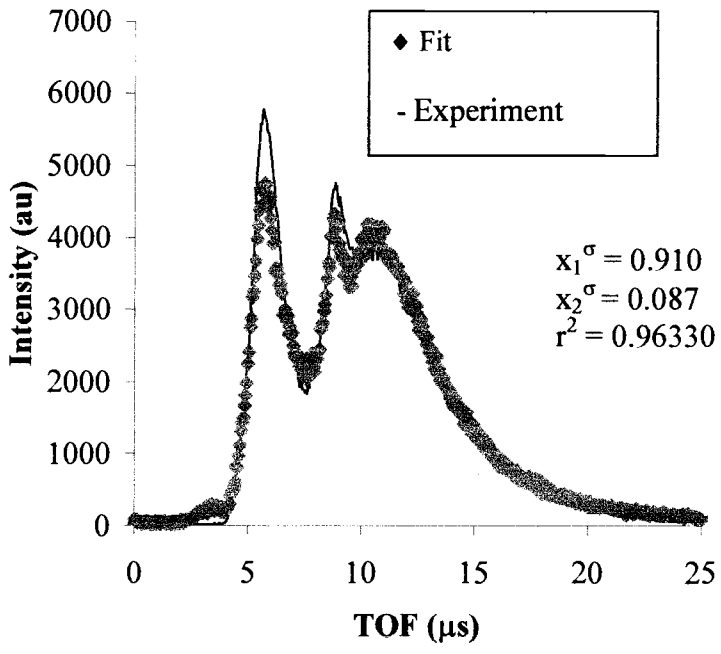

Figure 6.7 Example of Solver fit for solution B: Spectra obtained from 2.0-keV Ne^+ at a = 16°; liquid 1 is $[C_{12}mim][PF_6]$ and 2 is $[C_4mim][BF_4]$

of the cation. Yet, at the same time, the γ values of mixtures A and B, which only differ by the identity of the solute anion, are quite different. An analysis using Equation 6.1 leads to a surface mole fraction of 0.55-0.58 for the $[C_{12}mim]$ cation in mixture B. The γ data indicate that in mixture B there appears to be some segregation of the $[C_{12}mim]$ cation to the surface from the bulk, where its concentration was only 25 mol %, but the surface appears to be almost equal in the composition of the two materials.

This result is surprising both in view of the low surface energy of the $[C_{12}mim]$ cation, which in mixture A appears to be the majority of the surface cation, and the DR spectra, which also points towards a solute dominated surface. A possible origin for these discrepancies is that the solute is dominant at the surface but it exhibits a change in surface orientation resulting in its γ being increased, while remaining much lower than that of the solvent. However, the question arises why should the

orientation of a cation that is dominant at the surface change from that in the pure material if the only difference in the local environment is the replacement of a small percentage of $[PF_6]$ anions by $[BF_4]$ anions, a change that in the pure ILs only produces a change in the γ by a few percent?

A second scenario for mixture B is that indeed both cations share the surface, as the γ data suggest, but both have perturbed orientations. The presence of a second cation in sizable amounts might induce such changes in orientations relative to the pure materials. Such changes could explain the unusual γ results. It might also explain the difficulties in fitting the DR spectra as we could not be using the correct spectra, corresponding to reoriented cations, as the fit components. However, the physical reasons why such changes should occur as a result of apparently minor changes in the make-up of the anions in the system remain elusive.

6.5 CONCLUSION

The surface composition of two ionic liquid mixtures was investigated using DRS and γ measurements. The two mixtures consisted of approximately roughly 25 mol % of $[C_{12}mim][BF_4]$ in $[C_4mim][BF_4]$ (solution A) and 25 mol % $[C_{12}mim][PF_6]$ in $[C_4mim][BF_4]$ (solution B). Assuming that, the orientations of the solvent-solute ILs cations did not vary upon mixing as compared to the neat surface, the surface mole fractions of the solute (x_1^{σ}) were determined using the DR spectra and the γ values. For mixture A, the surface mole fraction of $[C_{12}mim][BF_4]$ calculated from both methods was ~0.90, indicating that the surface is enriched with the solute. However, with mixture B, there was disagreement between the x_1^{σ} values obtained from DRS and γ measurements. The former data set indicated sharing of the surface between the solute and solvent ILs, while the latter pointed to extreme surface enrichment by the solute. However, the DRs fits were very poor indicating that pure IL spectra were not good components for the fit. It seems likely that the cations

shared the surface and induced a mutual change in their surface orientations (compared to the neat ILs). As the solutions A and B differ in only anion content, it seems that the presence of an anion mixture allows for this change to occur.

7. GENERAL CONCLUSION

7.1 SUMMARY

This thesis represent the natural progression of the work performed in this laboratory concerning the application of DRS as an analytical technique to examine liquid surfaces. The instrument used in this laboratory was designed and constructed by Thomas Gannon and Michael Tassotto. Initial studies, by Gannon, on such liquids as dioctyl phthalate, bis (2-ethylhexyl) chlorendate, and glycerol showed the capabilities of the DRS technique to answer questions concerning the molecular composition and the preferential orientation at the vacuum-liquid interface [50]. At the same time Tassotto [51] used simulations and experimental DRS spectra to examine such fundamental issues as the depth distributions of recoils and the actual interaction potential between hydrogen and primary projectiles.

The logical "next step" was to utilize the DRS on a liquid system where the surface molecular arrangement may affect the kinetics or the product identities in a complex chemical reaction. The room-temperature ILs of the type described here have been used as solvents in multiphasic catalytic reactions where reactions occur at the liquid-liquid interface. The DRS experiments on such ILs, described in this thesis, shows that this tool can be used to provide an understanding of surface characteristics of molecules involved in reactions.

Chapter 4 described the first DRS study on neat ILs containing the 1-alkyl-3-methylimidazolium cation with the general formula $[C_n mim][X]$ (where n = 4, 8, and 12, and X = BF_4^-, PF_6^-, Cl^- and Br^-). DRS spectral data were obtained with Ne^+ projectiles with kinetic energies of 2.0 keV, and Ar^+ with energies of 2.5 keV. Analysis of the spectra, over the range of incidence angles, revealed that for fluorinated ILs a normal cation-anion stochiometric ratio (1:1) was maintained at the interface. However, with $[C_8mim][Cl]$ and $[C_8mim][Br]$, the absence of the halide

recoil signal did not allow for the determination of the surface composition. For the fluorine-containing ILs, the data revealed that the cation was arranged such that the imidazolium ring is perpendicular to the surface, where the average cation orientation is dependent on the angle of rotation (δ). Comparing the experimental atomic ratios with those derived from simulations allowed for determination of δ. In general, the [$C_n$mim] cations adopted δ value close to 270°, which placed the 3-methyl group near the surface. With the C12 ILs, the DRS data indicated that the cation favors an average orientation that fully exposes the methyl group at the surface.

Chapter 5 describes an attempt to relate γ measurements to the DRS findings. Such measurements were carried out for the [$C_n$mim] class of ILs, over a range of temperatures using a DuNouy tensiometer. The γ of ILs with a common anion was dependent on the length of the 1-alkyl chain. For example, with the tetrafluoroborate salts, γ (at 336 K) increased from 25.2 mJ/m^2 (n = 12) to 29.8 mJ/m^2 (n = 8) to 38.4 mJ/m^2 (n = 4). As is the case with many molecules, the γ values can be used to infer the molecule's surface orientation (Langmuir's Principle). However, the γ data for the [C_4mim][X] ILs did not clearly support the surface orientations from DRS. The γ values suggest an orientation that fully exposes the imdazolium ring at the surface (δ = 0° or 180°). But DRS data indicated an orientation, which places the methyl group uppermost. However, for the [C_8mim] ILs, the DRS data point to orientations similar to the C4 analogs, and the γ values consistent with such an arrangement. The γ values of the C4 and C8 ILs may suggest that for the ILs with the smaller cation, the ring has a greater effect on γ. In the case of the C12 ILs, the DRS data indicate the methyl group at the surface, but the γ values indicate that either the methyl or dodecyl group is at the surface. From γ, we were able to calculate Es and Ss, which showed that both values decreased with increasing n. For the ILs with a common

cation, Ss decreased with a reduction in anion size. The effects of decreasing anion size only resulted in a decrease of Es with the C4 and C8 ILs.

Both the DRS data and γ measurements provided a wealth of knowledge concerning neat ILs of the $[C_n mim][X]$ class. As discussed in Chapter 6, this work allowed for the determination of the surface characteristics of two ionic liquid mixtures with ~25 mole % solute and $[C_4mim][BF_4]$ as the solvent. In the solution in which $[C_{12}mim][BF_4]$ was the solute, the DRS and γ data indicated that the surface was enriched with the solute. With the assumption that the orientations of the cations did not change as relative to the pure ILs, we determined the surface mole fraction of the solute to be ~0.90. Such an enrichment of the $[C_{12}mim]$ cation at the surface may be attributed to its increased amphiphilic behavior relative to the $[C_4mim]$ cation. The analysis of a second mixture with $[C_{12}mim][PF_6]$ as the solute proved to be more difficult. The surface mole fractions calculated from DRS (x_1^{σ} = ~0.83) were not within agreement with those obtained from γ measurements (x_1^{σ} = ~0.55). However, we were able to argue that in this solution, where the components differ in both cation and anion identity, that the cations shared the surface and induced a mutual change in their surface orientations relative to the pure ILs.

7.2 FUTURE STUDIES

Much work remains to be done in the understanding of the surface characteristics of room-temperature ILs. In terms of pure ILs, we can extend the DRS studies to include other ILs families. However, since there are 10^{18} accessible ILs, the focus should be on those classes that are important as solvents in biphasic catalytic reactions. One class of ILs that shows promise as catalysis solvents, like the $[C_n mim]$ ILs, are those containing N-alkylpyridinium cations $[C_n py]$. Members of this family, such as $[C_6py][PF_6]$ and $[C_6py][BF_4]$, have been used in heck reactions. The DRS and γ investigations would be similar to those of the 1-alkyl-3-

methylimidazolium ILs, as to probe the effects of increasing the alkyl chain and changing the anion type on the surface composition and orientation.

Once we have an understanding of the neat ILs the next step would be to use DRS to explore the surface behavior of the catalyst solutions. However, as the investigation of mixtures, discussed in Chapter 6 indicates, such studies are difficult without comparing the experimental atomic ratios to those from predictions. Therefore, such studies of ILs solutions must be accompanied by the development of a surface simulation similar to LOS which can account for surface enrichment and changes in the ILs' orientation relative to the pure liquid. Such a simulation should allow for the estimation of atomic ratios within reasonable computational times. Then it would be possible to investigate the effects of the IL solvent on the surface composition of catalysts, and determine the influence of the catalyst on the orientation of the IL.

BIBLIOGRAPHY

[1] Birdi, K.S., Handbook of Surface and Colloid Chemistry, CRC Press, New York, 1997.

[2] Joos, P., Dynamic Surface Phenomena, VSP BV, Netherlands, 1999.

[3] Moore, W.J., Physical Chemistry, 4th ed., Prentice-Hall, New Jersey, 1972.

[4] Adamson, A.W., Physical Chemistry of Surfaces, 4th ed., Wiley, New York, 1982.

[5] Hudson, J.B., Surface Science: An Introduction, Wiley, New York, 1992.

[6] Lykema, J., Fundamentals of Interface and Colloid Science, Vol. I, Academic Press, London, 2000.

[7] Shen, Y.R., *Nature*, **337**, (1989), 519.

[8] Eisenthal, K.B., *Chem. Rev.*, **96**, (1996), 1343.

[9] Conboy, J.C., Messmer, M.C., and Richmond, G.L., *J. Phys.Chem.*, **100**, (1996), 7617.

[10] Goodall, D.G., Stevens, G.W., Beaglehole, D., and Gee, M.L.,, *Langmuir*, **15**, (1999), 4579.

[11] Beaglehole, D., *J. Phys. Chem.*, **93**, (1989), 893.

[12] Pfohl, T., Beaglehole, D., and Riegler, H., *Chem. Phys. Lett*, **260**, (1996), 82.

[13] Thoma, M., Schwendler, M., Baltes, H., Helm, C.A., Pfohl, T., Riegler, H., and Mohwald, H., *Langmuir*, **12**, (1996), 1722.

[14] Ocko, B.M., Wu, X.Z., Sirota, E.B., Sinha, S.K., Gang, O., and Deutsch, M., *Phys. Rev. E*, **55**, (1997), 3164.

[15] Gang, O., Wu, X.Z., Ocko, B.M., Sirota, E.B., and Deutsch, M., *Phys. Rev. E*, **58**, (1998), 6086.

[16] Lucht, R., Marczuk, P., Bahr, Ch., and Fidenegg, G.H., *Phys. Rev. E*, **63**, (2001), 7041.

[17] Morton, S., Information on surface analysis techniques from http://www.uksaf.org/tech/iss.html (2001).

[18] Williams, R.S., "Quantitative Intensity Analysis of Low-energy Scattering and Recoiling from Crystal Surfaces," in: Low Energy Ion-Surface Interactions, ed. J.W. Rabalais, Wiley, New York, 1994.

[19] Turkevich, A.L., Surveyor Project Final Report, Part II: Scientific Results, NASA Tech. Rep., NBS, Washington DC, 32-1265, 303 (1968).

[20] Datz, S.D., and Snoek, C., *Phys. Rev. A*, **134**, (1964), 347.

[21] Mashkova, E.S., and Molchanov, V.A., *Zh. Tekh. Fiz.*, **35**, (1965), 1321.

[22] Mashkova, E.S., and Molchanov, V.A., *Sov. Phys. Tech. Phys.*, **10**, (1966), 1024.

[23] Smith, D.P., *J. Appl. Phys.*, **38**, (1968), 340.

[24] Chu, W.K., Mayer, J.W., Nicolet, M.A., Buck, T.M., Amsel, G., and Eisen, E., *Thin Solid Films*, **17**, (1973), 1.

[25] Brongersma, H.H., and Mul, P.M., *Surf. Sci.*, **35**, (1973), 393.

[26] Chen, Y.S., Miller, G.L., Robinson, D.A.H., Wheatley, G.H., and Buck, T.M., *Surf. Sci.*, **62**, (1977), 133.

[27] Luitjens, S.B., Algra, A.J., Suurmijer, E.P., and Boers, A.L., *Appl. Phys.*, **21**, (1980), 205.

[28] Schneider, P.J., Eckstein, W., and Verbeek, H., *Nucl. Instrum. Methods*, **218**, (1983), 713.

[29] Schultz, J.A., Kumar, R., and Rabalais, J.W., *Chem. Phys. Lett*, **100**, (1983), 214.

[30] Jo, Y.S., Schultz, J.A., Tachi, S., Contarini, S., and Rabalais, J.W., *J. Appl. Phys.*, **60**, (1986), 2564.

[31] Schmidt, H.K., Schultz, J.A., Tachi, S., Contarini, S., Adura, S., Rabalais, J.W., and Margrave, J.L., *J. Vac. Sci. Technol. A*, **5**, (1987), 2961.

[32] Rabalais, J.W., *CRC Critical Rev. Sol. St. Mat. Sci.*, **14**, (1988), 319.

[33] Tassotto, M., and Watson, P.R., *Surf. Sci.*, **464**, (2000), 251.

[34] Tassotto, M., Gannon, T.J., and Watson, P.R., *J. Chem. Phys.*, **107**, (1997), 8899.

[35] Gannon, T.J., Tassotto, M., and Watson, P.R., *Chem. Phys. Lett.*, **300**, (1998), 163.

[36] Gannon, T.J., Law, G., and Watson P.J., *Langmuir*, **15**, (1999), 8429.

[37] Ubbelohde, A.R., "Research on Molten Salts: Introduction," in: Ionic Liquids, ed. D. Inman, and D.G. Lovering, Plenum Press, New York, 1981.

[38] Sugden, S., and Wilkins, H., *J. Chem. Soc.*, (1929), 1291.

[39] Hussey, C.L., *Pure Appl. Chem.*, **60**, (1988), 1763.

[40] Seddon, K.R., *J. Chem. Tech. Biotechnol.*, **68**, (1997), 351.

[41] Welton, T., *Chem. Rev.*, **99**, (1999), 2071.

[42] Holbrey, J.D., and Seddon, K.R., *Clean Prod. Processes*, **1**, (1999), 223.

[43] Earle, M.J., and Seddon, K.R., *Pure Appl. Chem.*, **72**, (2000), 1391.

[44] Bowlas, C.J., Bruce, D.W., and Seddon, K.R., *J. Chem. Soc. Chem. Comm.*, **147**, (1996), 1625.

[45] Freemantle, M., *C&EN*, (March 30, 1998), 32.

[46] Herrmann, W.A., and Kocher, C., *Angew. Chem. Int. Ed. Engl.*, **36**, (1997), 2163.

[47] Carmichael, A.J., Earle, M.J., Holbrey, J.D., McCormac, P.B., and Seddon, K.R., *Org. Lett.*, **1**, (1999), 997.

[48] Chauvin, Y., Einloft, S., and Oliver, H., *Ind. Eng. Chem. Res.*, **34**, (1995), 1149.

[49] Heck, R.F., Organic Reactions, vol. 27, Wiley, New York, 1982.

[50] Gannon, T.J., "Time-of-Flight Scattering and Recoil Spectrometry (TOF-SARS) Applied to Molecular Liquid Surfaces: A New Approach to Surface Composition and Orientation," Ph.D. Thesis, Oregon State University, 1999.

[51] Tassotto, M., "Time-of-Flight Direct Recoil Spectrometry: Application to Liquid Surfaces and Steps Toward Quantification," Ph.D. Thesis, 2000.

[52] Rabalais, J.W.., "Ion Scattering and Recoiling for Elemental Analysis and Structural Determination," in: Low Energy Ion-Surface Interactions, ed. J.W. Rabalais, Wiley, New York, 1994.

[53] Johnson, R.E., Introduction to Atomic and Molecular Collisions, Plenum Press, New York, 1982.

[54] Halliday, D., Resnick, R., and Walker, J., Fundamentals of Physics , 4th ed., Wiley and Sons, New York, 1993.

[55] Robinson, M.T., Torres, I.M., *Phys. Rev. B*, **9**, (1974), 5008.

[56] Olsen, J.O., Anderson, T., Barat, M., Courbin-Gaussorgues, Ch., Sidis, V., Pommier, J., Agusti, J., Anderson, N., Russek, A., *Phys. Rev. A*, **19**, (1979), 1457.

[57] McDaniel, E.W., Mitchell, J.B.A., and Rudd, M.E., Atomic Collisions: Heavy Particle Projectiles, Wiley and Sons, New York, 1993.

[58] Seddon, K.R., Stark, A., and Torres, M.-J., *Pure Appl. Chem.*, **72**, (2000), 2275.

[59] Carmichael, A.J., and Seddon, K.R., *J. Phys. Org. Chem.*, **13**, (2000), 591.

[60] Sudhir, N.K., Brennecke, J., and Samanta, A., *Chem. Comm.*, (2001), 413.

[61] Hagiwara, R., and Yasuhiko, I., *J. Fluorine Chem.*, **105**, (2000), 221.

[62] Gordon, C.M., Holbrey, J.D., Kennedy, A.R., and Seddon, K.R., *J. Mater. Chem.*, **12**, (1998), 2627.

[63] Holbrey, J.D., and Seddon, K.R., *J. Chem. Soc., Dalton Trans.*, **13**, (1999), 2133.

[64] Abdul-Sada, A.K., Atkins, M.P., Ellis, B., Hodgson, P.K.G., Morgan, M.L.M., and Seddon, K.R., World Pat., WO9521806, 1995.

[65] Abdul-Sada, A.K., Ambler, P.W., Hodgsen, P.K.G., Seddon, K.R., and Stewart, N.J., World Pat., WO9521871, 1995.

[66] Fuller, J., Carlin, R.T., De Long, H.C., and Haworth, D., *J. Chem. Soc. Chem. Comm.*, (1994), 299.

[67] Frenkel, J., Kinetic Theory of Liquids, Dover, New York, 1955.

[68] Kloubek, J., *Colloids Surf.*, **48** (1990), 323.

[69] Gibbs, J.W., Collected Works, Vol. I., Dover, New York, 1961.

[70] Young, T., *Trans. Roy. Soc.*, **95**, (1805), 95.

[71] Good, R.J., *J. Chem. Phys.*, **61**, (1957), 810.

[72] Earnshaw, J.C., and Hughes, C.J., *Phys. Rev. A*, **46**, (1992), 4494.

[73] Wu, X.Z., Sirota, E.B., Sinha, S.K., Ocko, B.M., and Deutsch, M., *Phys. Rev. Lett.*, **70**, (1993), 958.

[74] Sefler, G.A., Du, Q., Miranda, P.B., and Shen, Y.R., *Chem. Phys. Lett.*, **235**, (1995), 347.

[75] Harkins, W.D., and Jordan, H.F., *J. Am. Chem. Soc.*, **52** (1930), 1751.

[76] Zuidema, H.H., and Waters, G.W., *Ind. Eng. Chem. Anal. Ed.*, **13** (1941), 312.

[77] CSC DuNouy Tensiometers CSC No. 70535 and 70545, CSC Scientific Company Inc., Fairfax, 1990.

[78] Birdi, K.S., Handbook of Surface and Colloid Chemistry, CRC Press, New York, 1997.

[79] Janz, G.J., Lankshminarayanan, G.R., Tomkins, R.P.T., and Wong, J., Molten Salts: Volume 2, Section 2. Surface Tension Data, National Bureau of Standards, NBS, Washington DC, CODEN:NSRDA, NSRDS-NBS 28 (1969).

[80] Matsumoto, M., and Kataoka, Y., *J. Chem. Phys.*, **90**, (1989), 2398.

[81] Mach, P., Huang, C.C., Stoebe, T., Wedell, E.D., Ngygen, T., Jeu, W.H.D., Guittard, F., Naciri, J., Shashidhar, R., Clark, N., Jiang, I.M., Kao, F.J., Liu, H., and Nohira, H., *Langmuir*, **14**, (1998) 4330.

[82] Goodisman, J., *J. Colloid Interface Chem.*, **73**, (1980), 115.

[83] Hoffman, K., Imidazole and its Derivatives, Vol: I, Interscience, New York, 1953.

[84] Kloubek, J., *Colloids Surf.*, **55** (1991), 191.

[85] Wasserscheild, P., and Keil, W., Angew. Chem. Int. Ed., 39 (2000), 3772.

[86] Dupont, J., Consorti, C.S., and Spencer, J., J. Braz. Chem. Soc., 11 (2000), 337.

[87] Hildebrand, J.H., and Scott, R.L., The Solubility of Nonelectrolytes, New York, 1950.

APPENDICES

Appendix A. Recoil Cross Sections

The dependence of the recoil cross sections (σ_i) on ion energy (E_o) of both Ar^+ and Ne^+ was determined for various atomic species from experiments carried out in this laboratory [33]. The general expression is given as

$$\sigma_i = A\, E_o^{-B}$$

where A and B are constants determined from the fit of recoil cross section versus projectile energy curves. The values of the constants for the projectiles used to obtain the spectra discussed in this thesis are shown on the next page in Tables A.1 and A.2 for the experimental recoil angle (ϕ) of 45°.

Table A.1 Constants A and B for various atomic species (projectile = Ne^+)

Atomic Species	A	B
Hydrogen	814.24	0.9369
Carbon	1911.8	1.0124
Nitrogen	1883.5	1.0051
Oxygen	1860.6	0.9985
Fluorine	1821.9	0.9948
Phosphorus	1722.1	0.9611
Chlorine	1676.0	0.9512
Bromine	1218.3	0.8683

Table A.2 Constants A and B for various atomic species (projectile = Ar^+)

Atomic Species	A	B
Hydrogen	426.16	0.7268
Carbon	1866.4	0.8890
Nitrogen	1795.1	0.8807
Oxygen	1712.1	0.8726
Fluorine	1651.8	0.8704
Phosphorus	1294.1	0.8254
Chlorine	1206.6	0.8134
Bromine	734.38	0.7290

Appendix B. Supplemental DRS Spectra

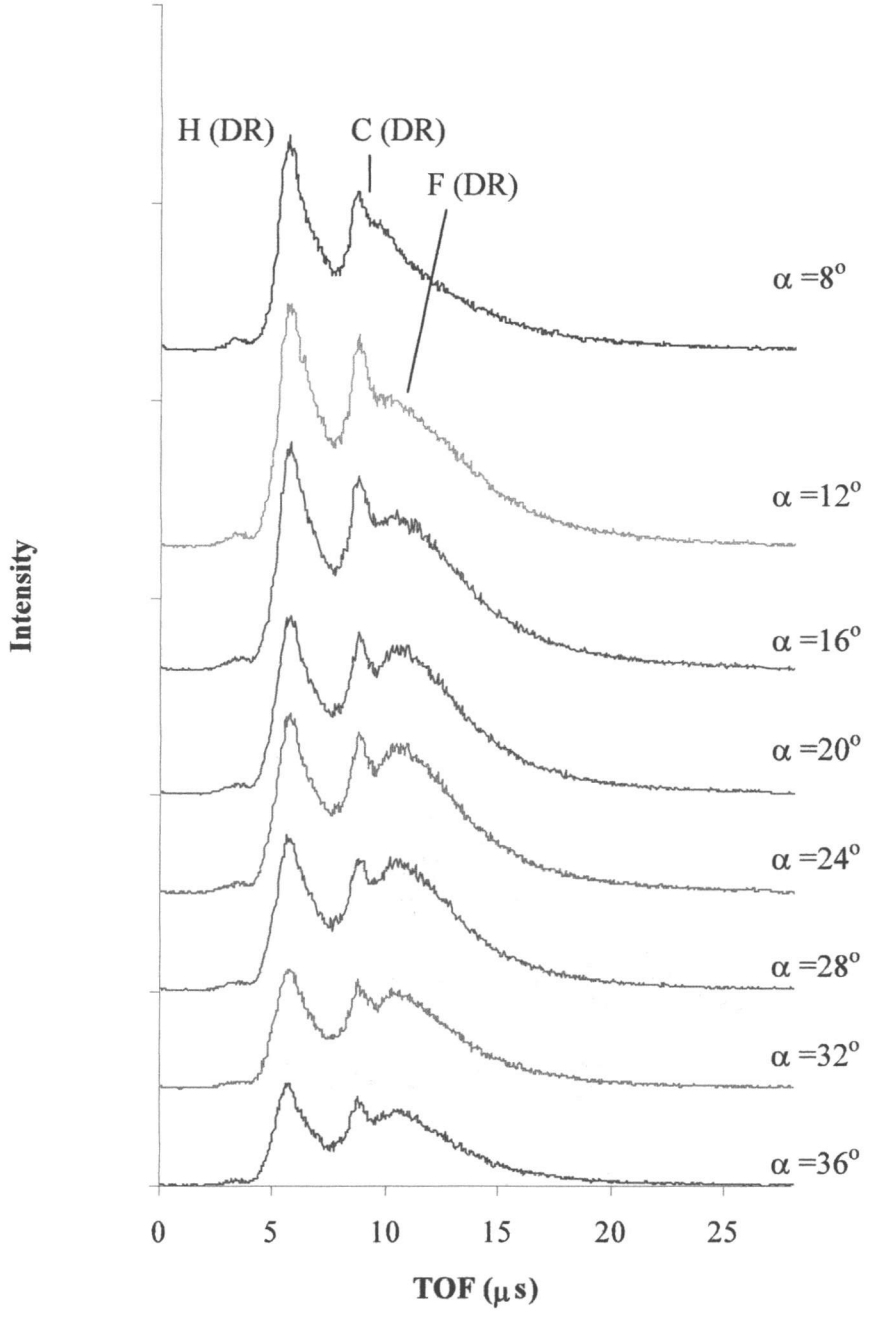

Figure B.1 DR Spectra of $[C_{12}mim][BF_4]$ obtained from 2.0-keV Ne^+

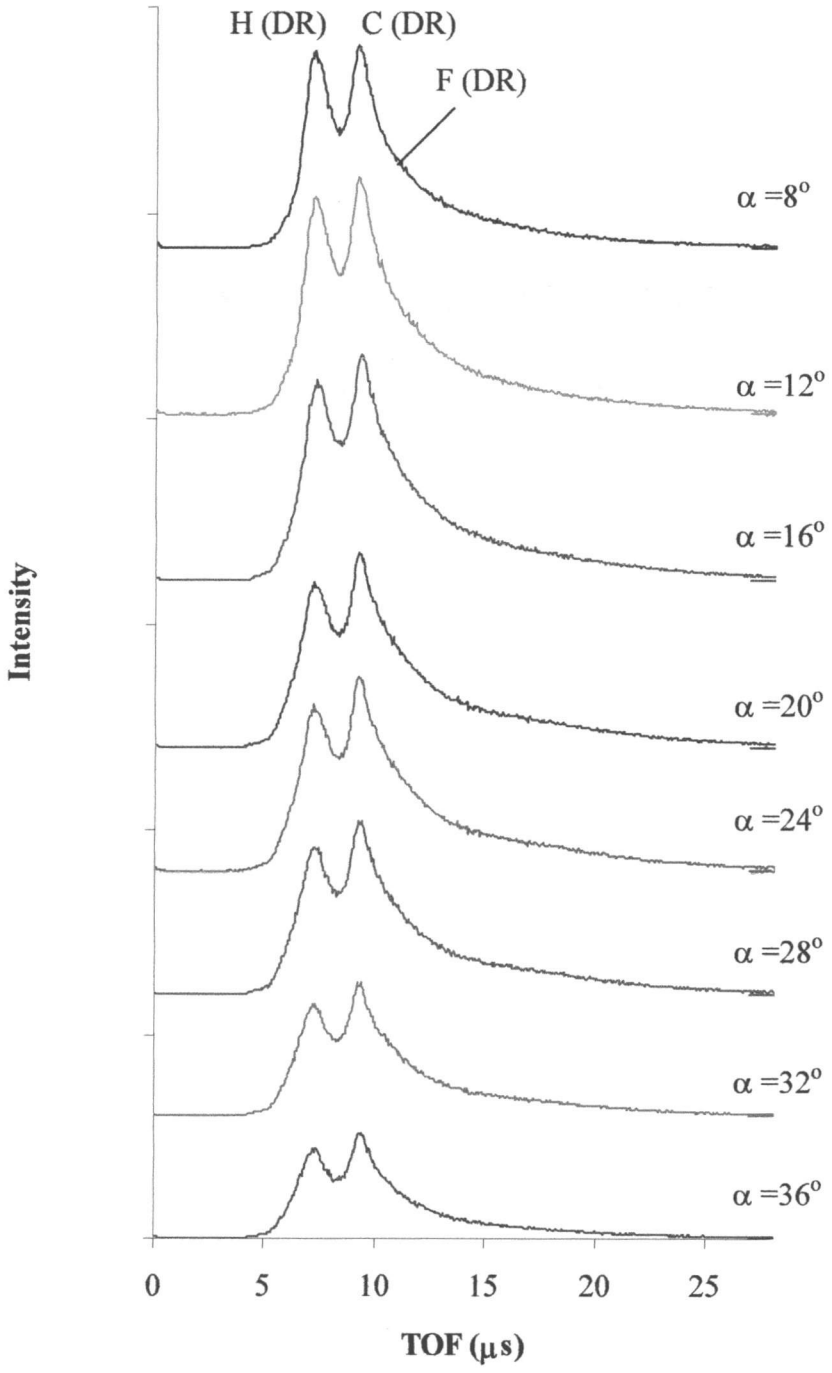

Figure B.2 DR Spectra of $[C_{12}mim][BF_4]$ obtained from 2.5-keV Ar^+

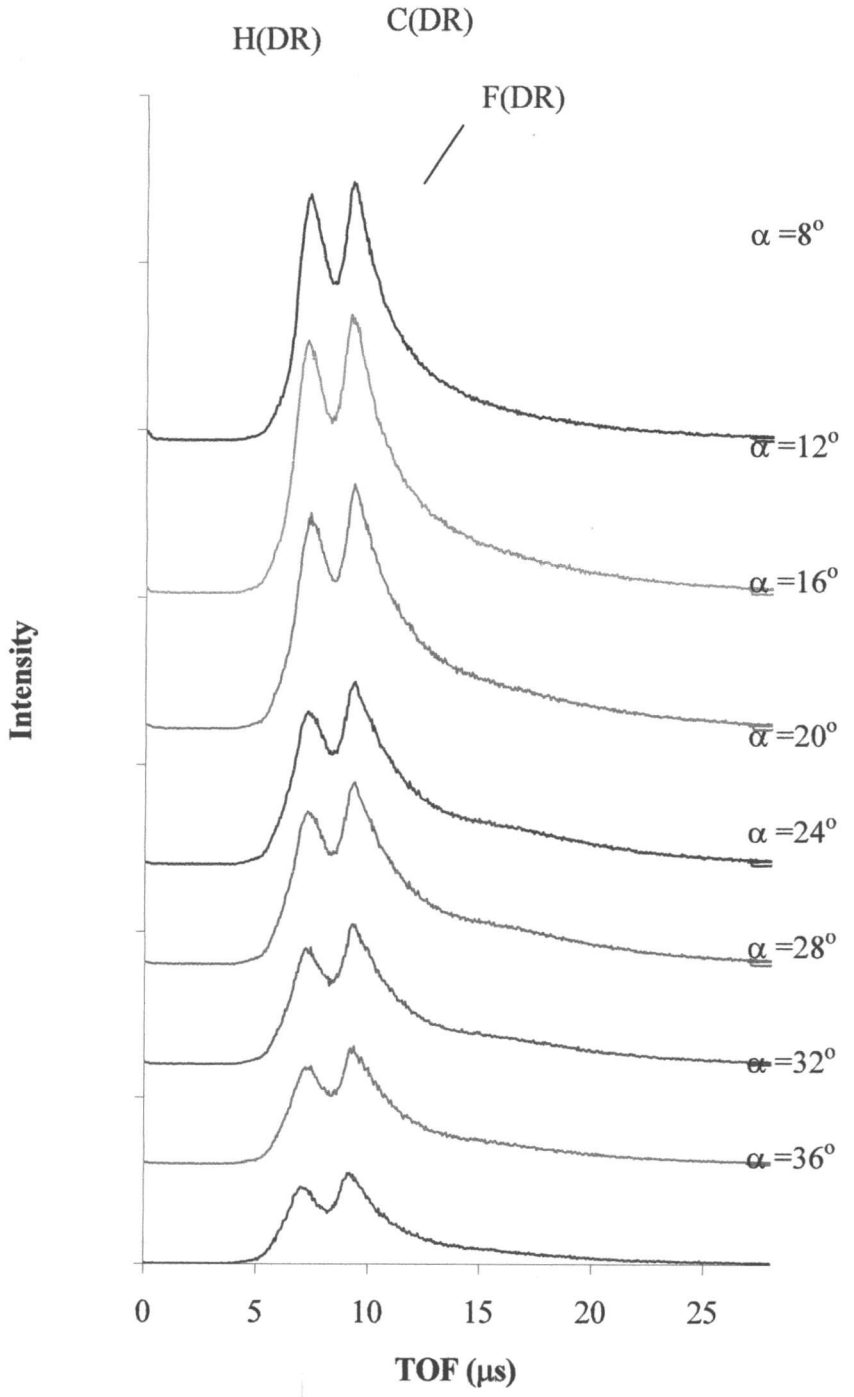

Figure B.3 DR Spectra of $[C_{12}mim][PF_6]$ obtained from 2.5-keV Ar^+

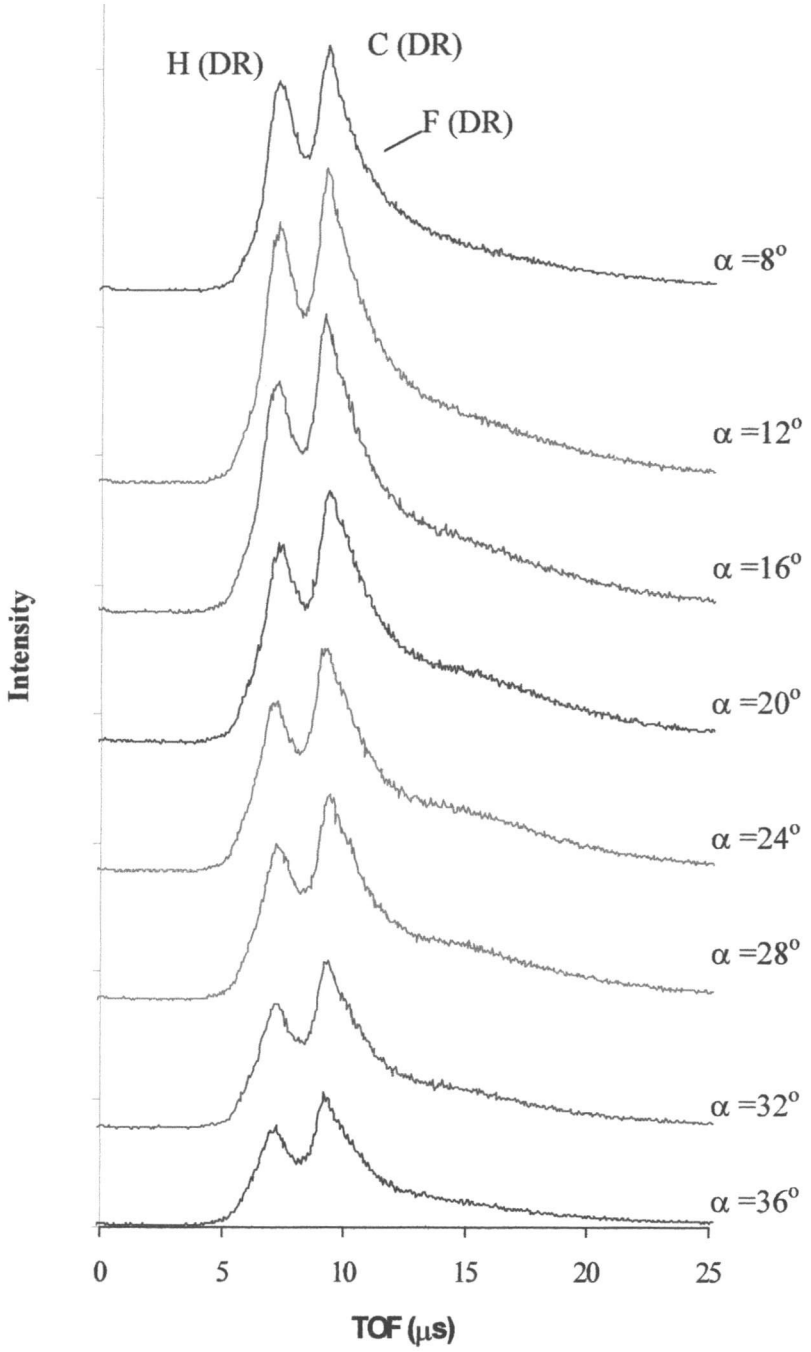

Figure B.4 DR Spectra of $[C_8mim][PF_6]$ obtained from 2.5-keV Ar^+

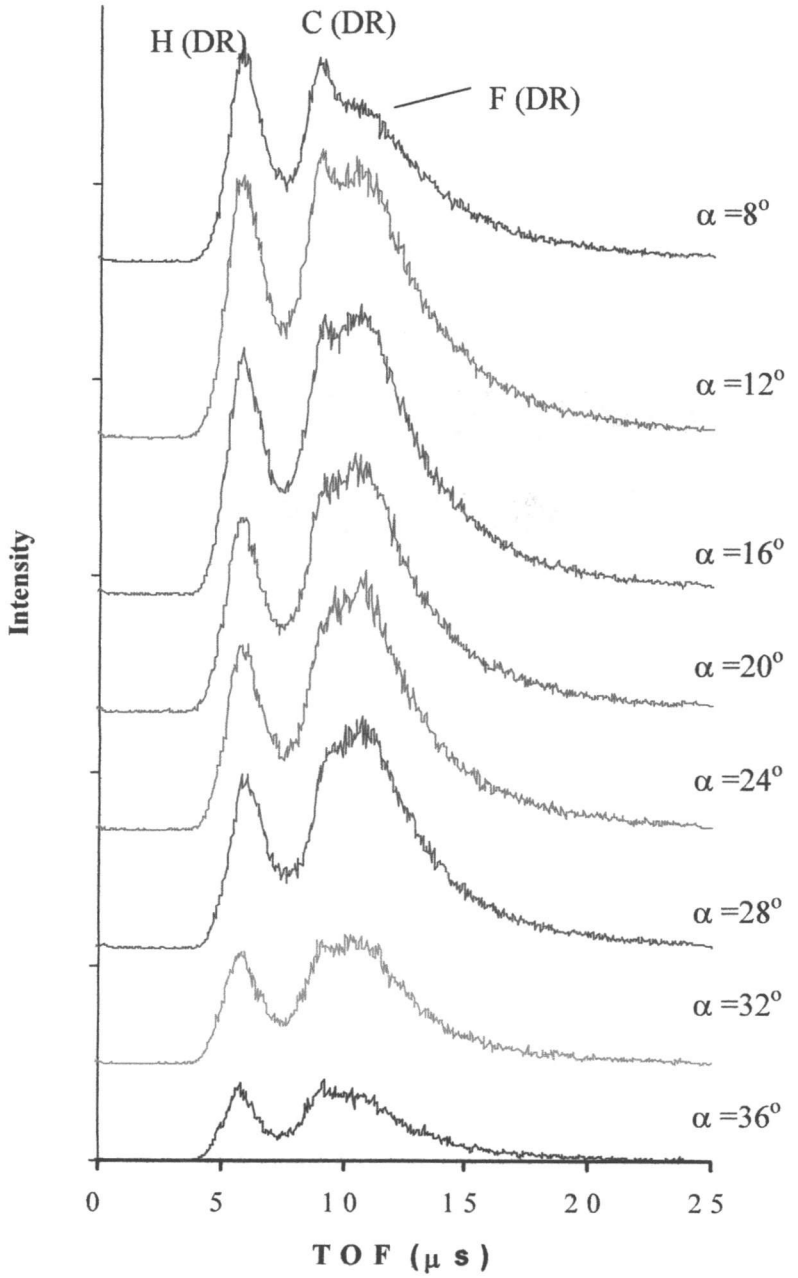

Figure B.5 DR Spectra of $[C_8mim][PF_6]$ obtained from 2.0-keV Ne^+

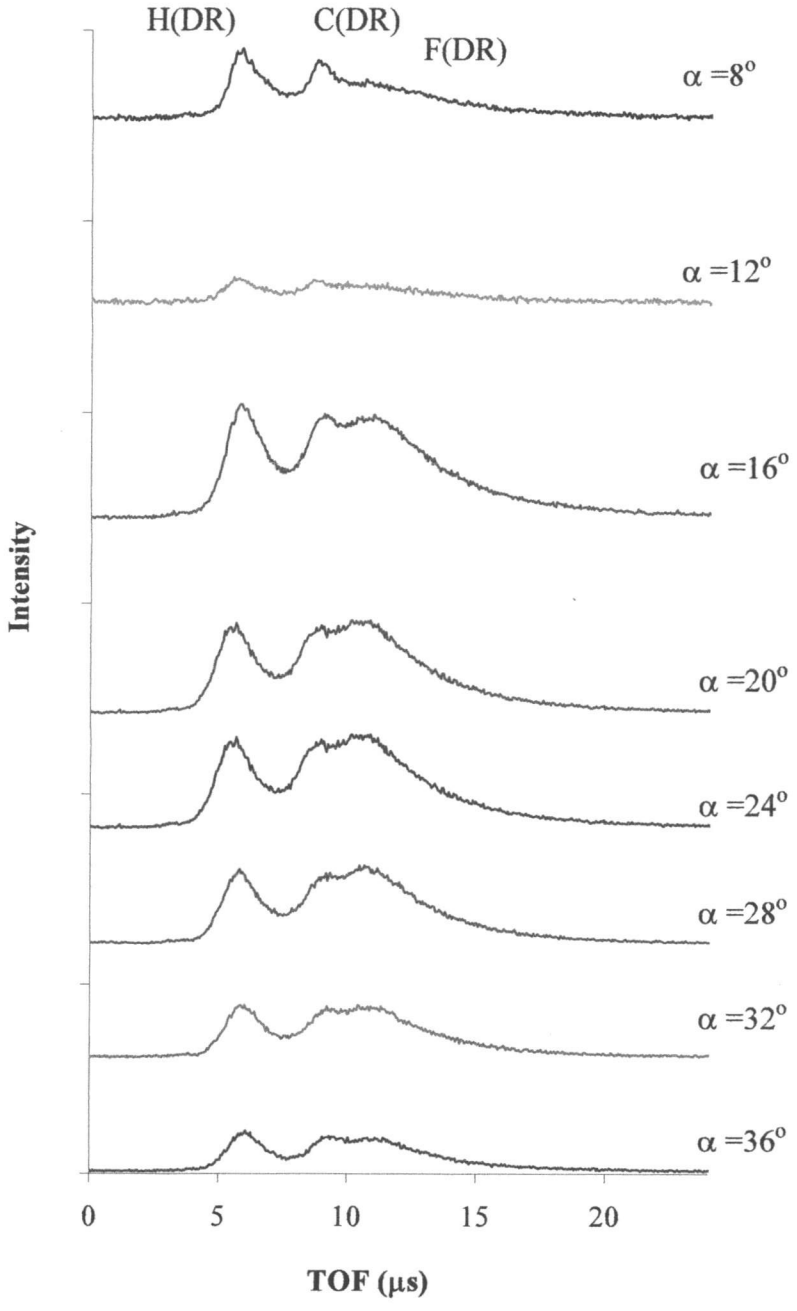

Figure B.6 DR Spectra of $[C_8mim][BF_4]$ obtained from 2.0-keV Ne^+

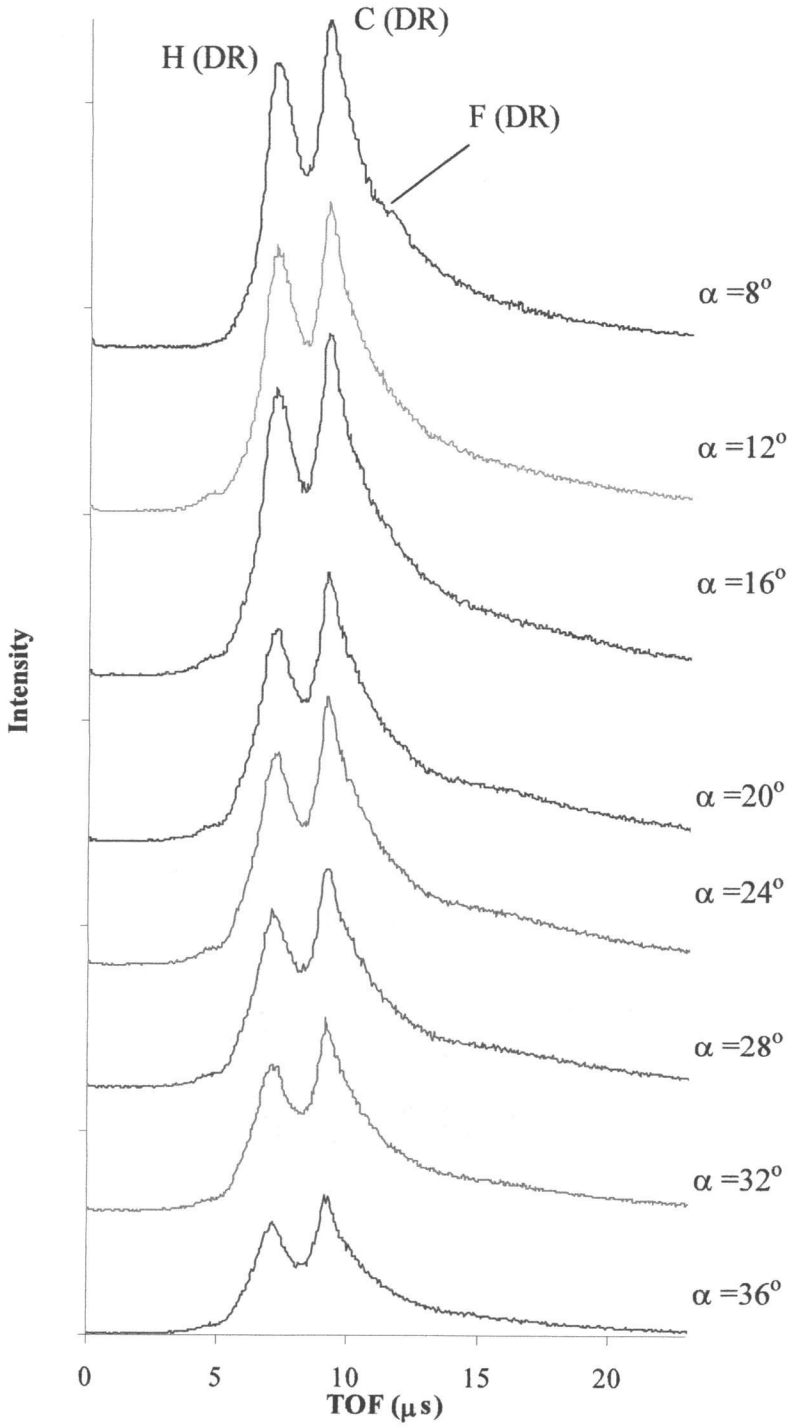

Figure B.7 DR Spectra of $[C_8mim][BF_4]$ obtained from 2.5-keV Ar^+

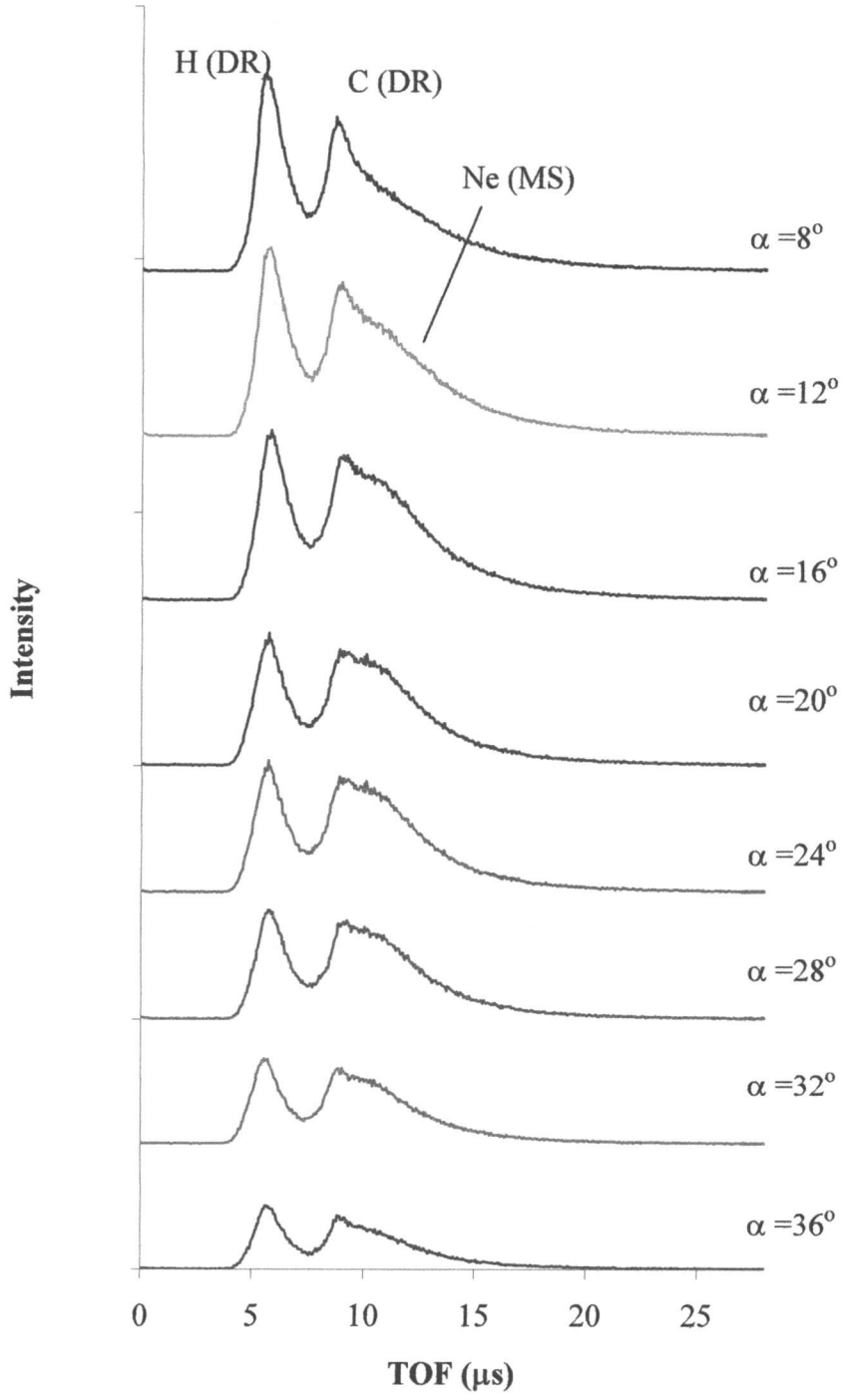

Figure B.8 DR Spectra of [C_8mim]Cl] obtained from 2.0-keV Ne^+

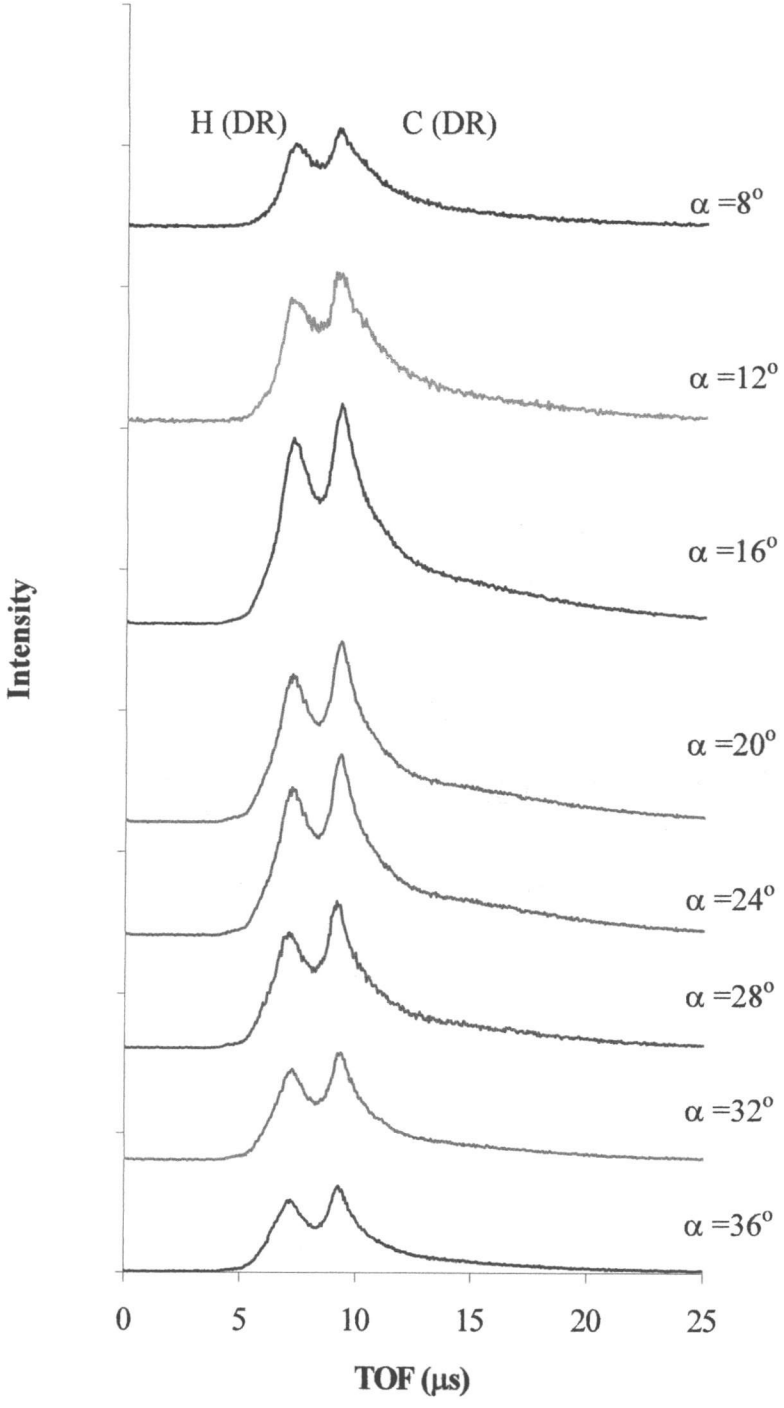

Figure B.9 DR Spectra of [C_8mim]Cl] obtained from 2.5-keV Ar^+

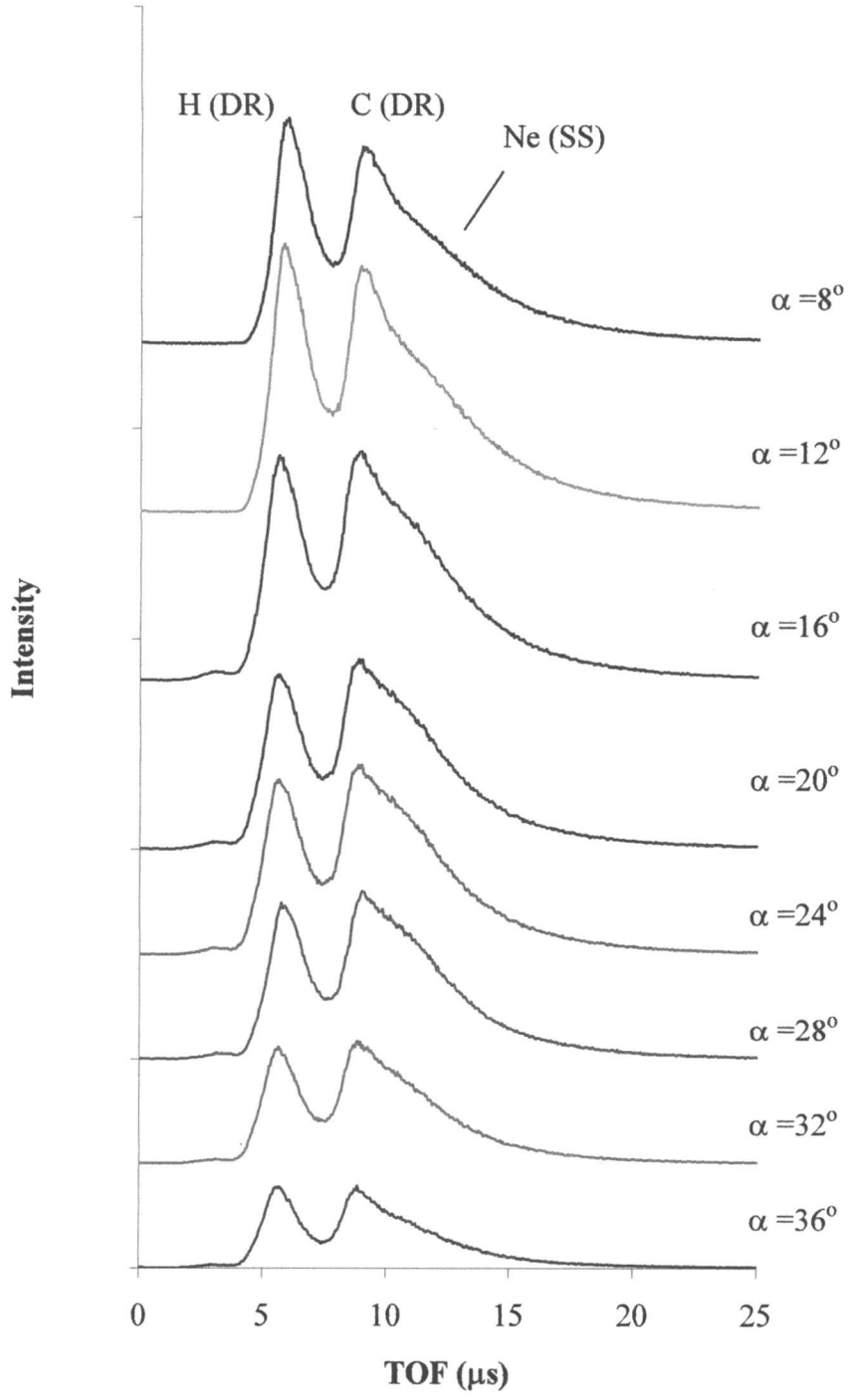

Figure B.10 DR Spectra of [C_8mim][Br] obtained from 2.0-keV Ne^+

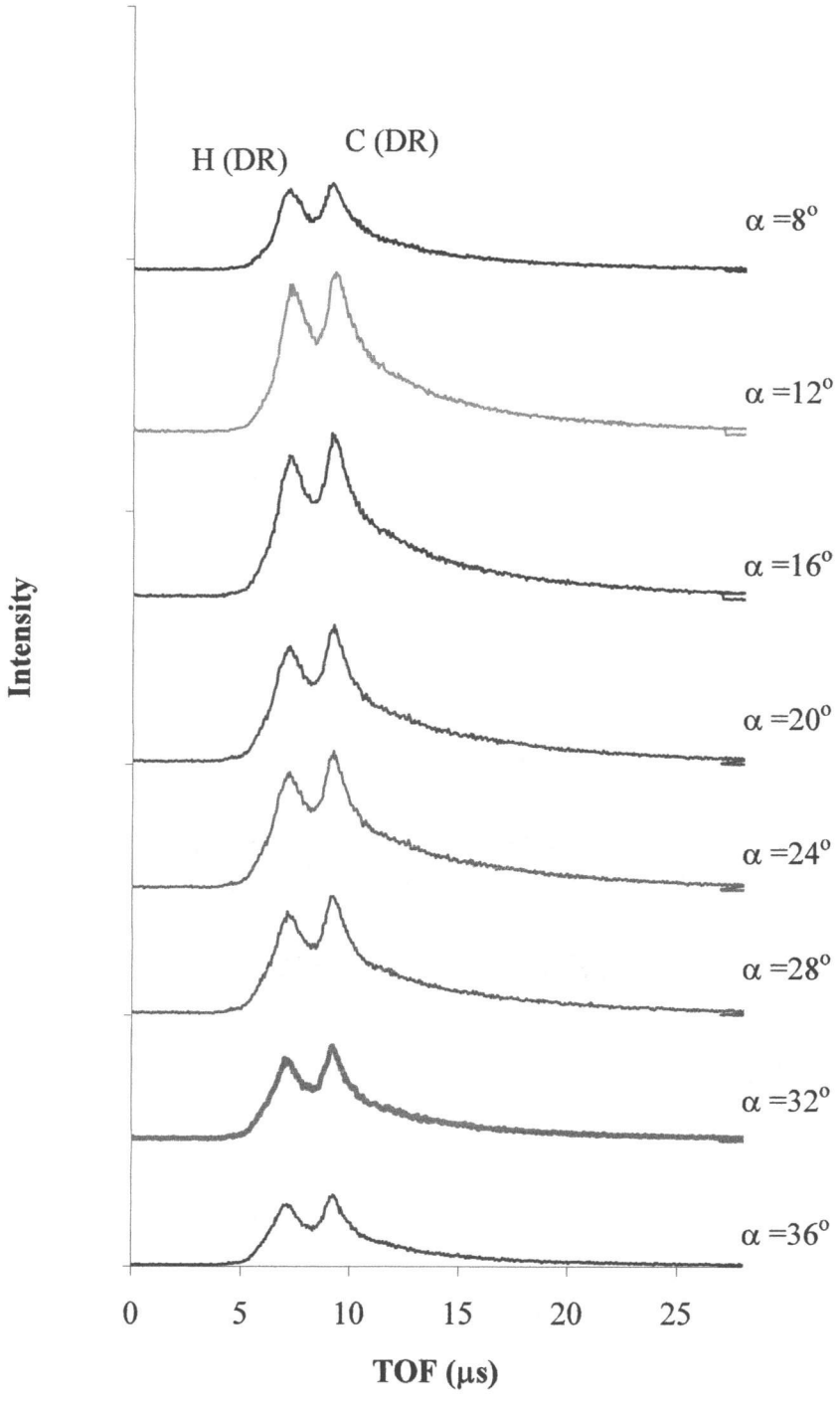

Figure B.11 DR Spectra of [C_8mim][Br] obtained from 2.5-keV Ar^+

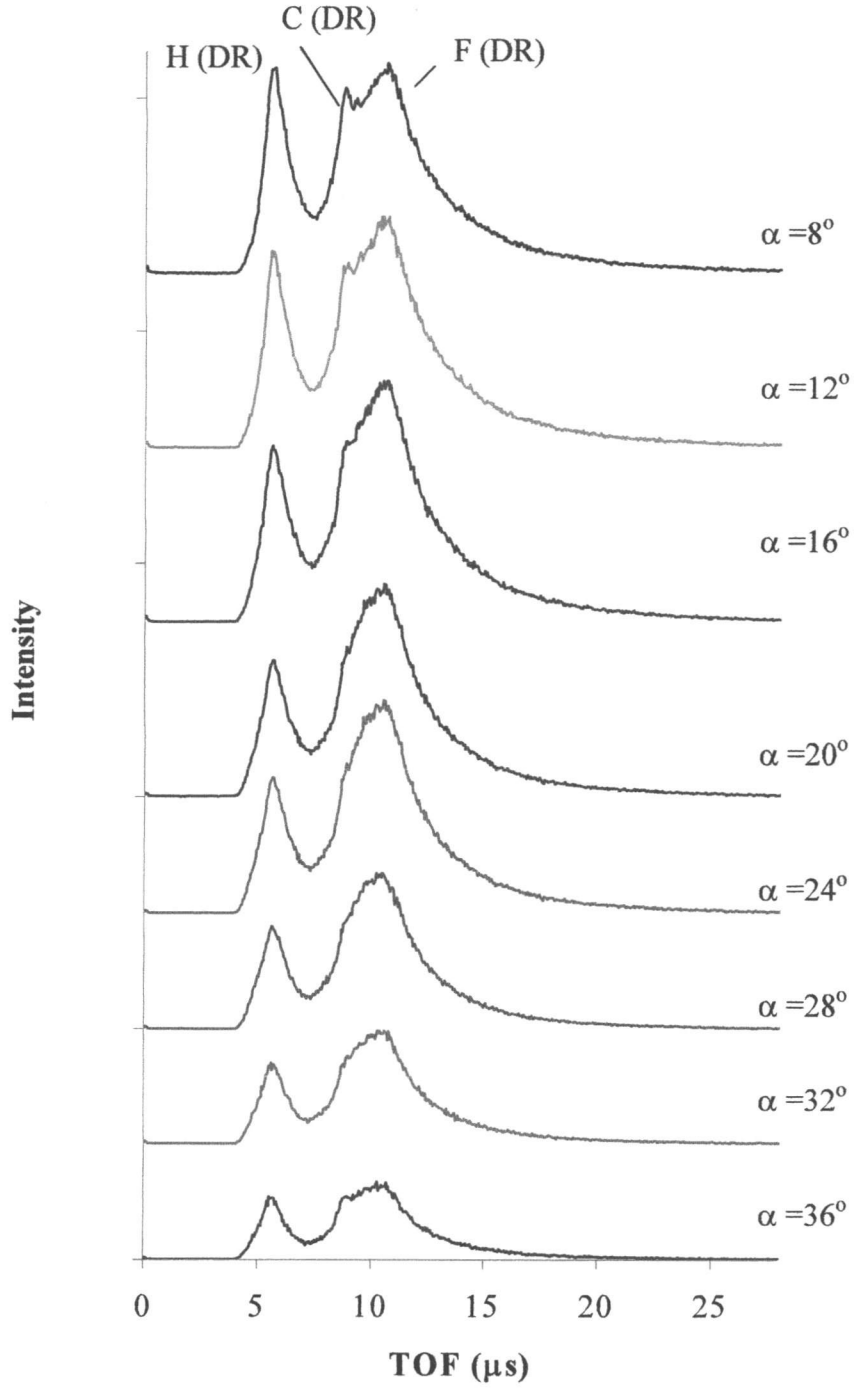

Figure B.12 DR Spectra of $[C_4mim][PF_6]$ obtained from 2.0-keV Ne^+

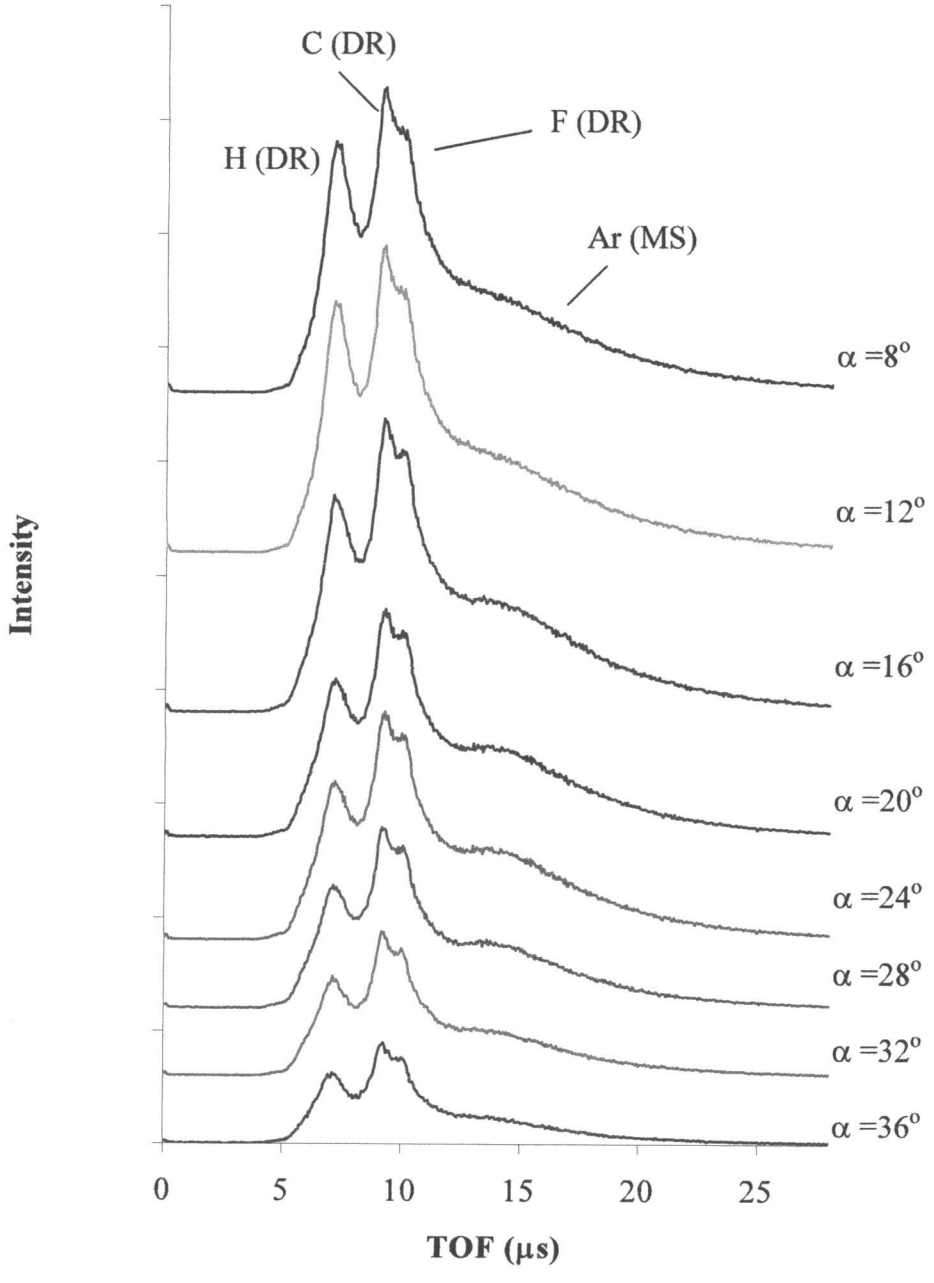

Figure B.13 DR Spectra of $[C_4mim][PF_6]$ obtained from 2.5-keV Ar^+

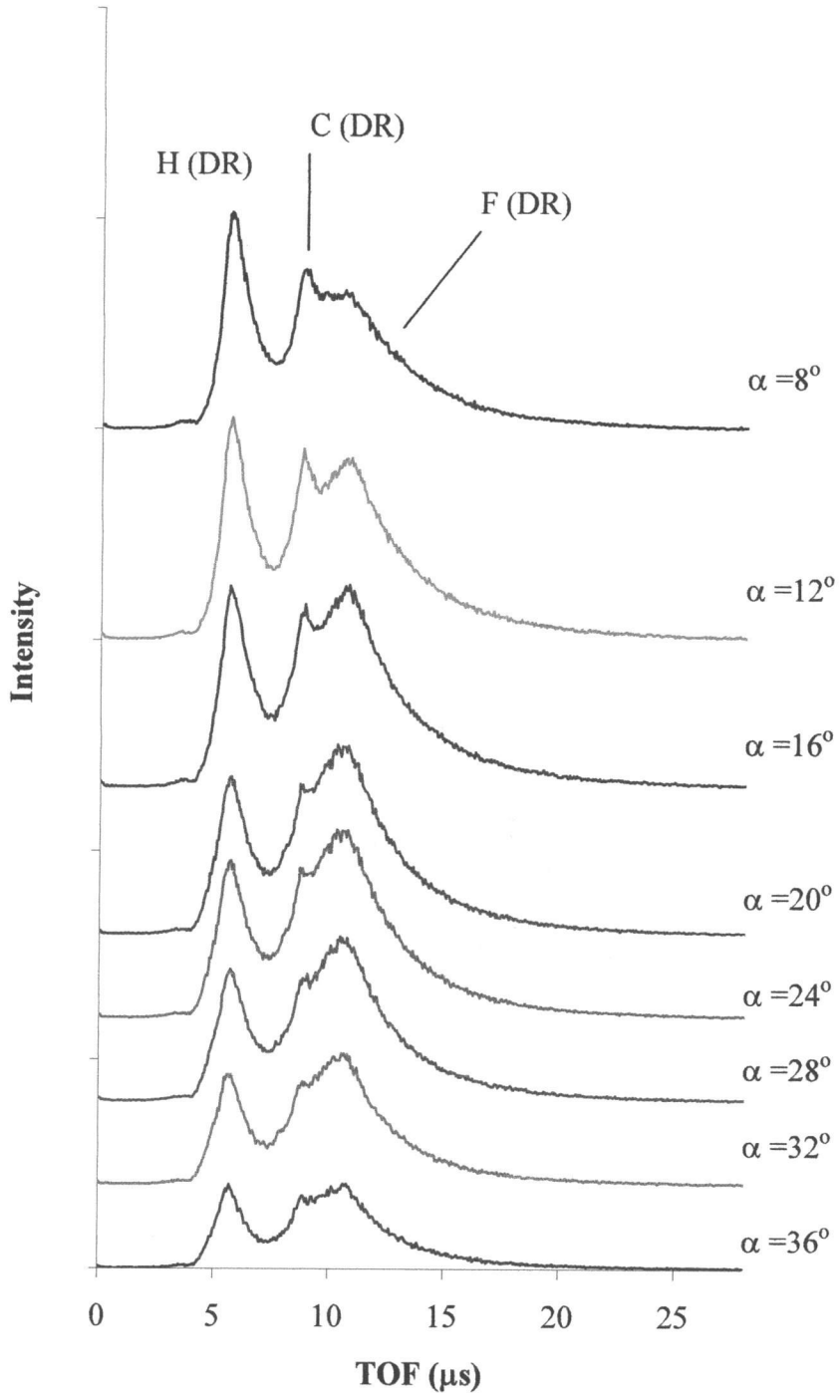

Figure B.14 DR Spectra of $[C_4mim][BF_4]$ obtained from 2.0- keV Ne^+

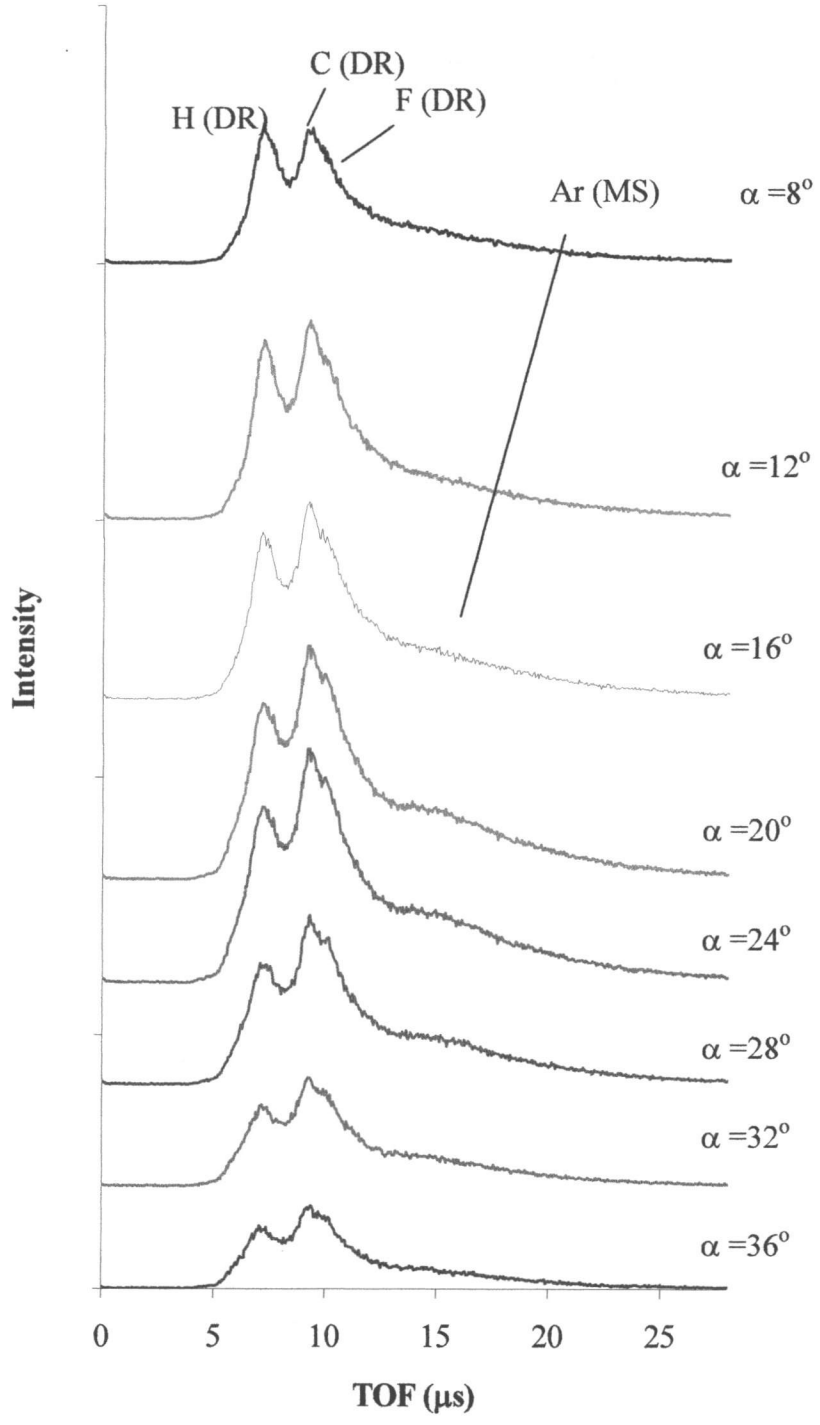

Figure B.15 DR Spectra of $[C_4mim][BF_4]$ obtained from 2.5-keV Ar^+

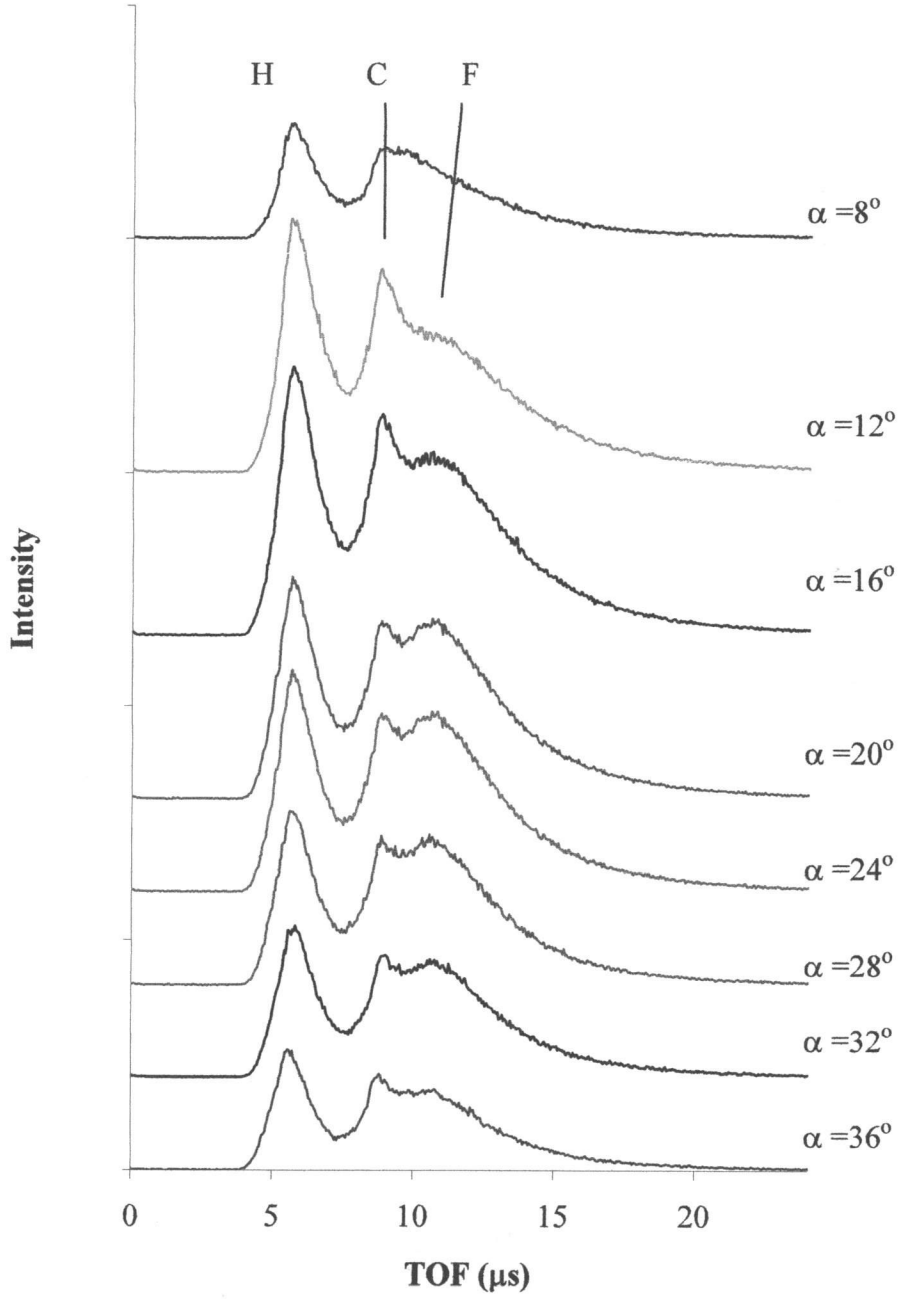

Figure B.16 DR Spectra of $[C_{12}mim][PF_6]$ (25.3 mole %) $[C_4mim][BF_4]$ obtained from 2.0-keV Ne^+

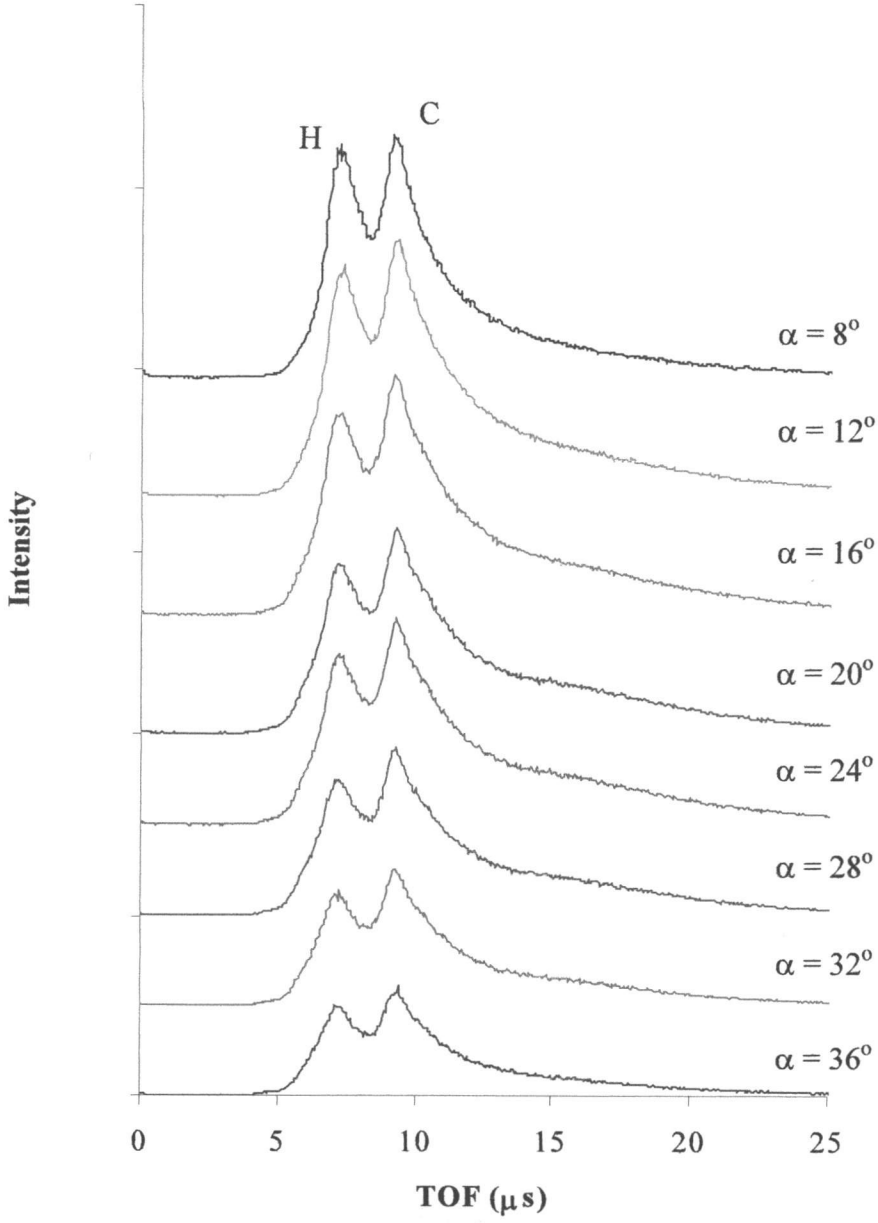

Figure B.17 DR Spectra of $[C_{12}mim][PF_6]$ (25.3 mole %) $[C_4mim][BF_4]$ obtained from 2.5-keV Ar^+